Université catholique de Louvain
Secteur des sciences et technologies
Institut de recherche en mathématique et physique
Centre for Cosmology, Particle Physics and Phenomenology



Dark matter searches in the context of simplified models

Doctoral dissertation presented by

Antony Martini

in fulfilment of the requirements for the degree of Doctor of Science

Jury de thèse

Prof. Fabio Maltoni (Advisor)	UCL, Belgium
Prof. Jean-Marc Gérard (Chairman)	UCL, Belgium
Dr. Chiara Arina	UCL, Belgium
Prof. Steven Lowette	VUB, Belgium
Prof. Alberto Mariotti	VUB, Belgium
Prof. Kentarou Mawatari	LPSC, France

September 15, 2017

Acknowledgements

This work is the result of close collaborations and discussions. First of all I would like to thank every people who contributed to the achievement of this thesis and to my understanding of particle physics. To all of you, regardless whether you are professor, PostDoc, PhD student or/and friends, I would like to express my sincere gratitude.

I start with the jury of my PhD defence. Thanks a lot to Jean-Marc, Fabio, Chiara, Steven, Alberto and Kentarou, we had a useful discussion on my work and your expertise also allowed me to improve my knowledge.

I warmly thank my supervisor Fabio Maltoni for the support and the help along these past four years. You always did your best to get funds for my PhD and I am very grateful for that. Then you have created an efficient team on dark matter searches at CP3 starting with me, I really appreciate your confidence in me. Even if it was always difficult to find a moment with you (I often joked about the fact that you was off-shell sometimes), you always guided me to find great collaborators, great conferences and great doctoral schools. On top of that you always had an informed advice on the direction to go in the underlying projects.

I would like to thank my closest collaborators. Kentarou, I am so pleased to have collaborated with you from the beginning. I have learnt so much about collider physics with you. I think we were an efficient duo for working on a daily basis. On top of that I appreciate your human qualities and for me we are more than colleagues. Mihailo, I really appreciated working with you. Thanks to you I also travelled much more than we could expect from my Belgian home lover character. Together we could discuss about any topics, professional or private and I hope we will keep in touch. Chiara, I enjoyed working with you at the end of my PhD and actually I would have appreciated to collaborate with you even sooner. You are a nice person. I would like to thank

Olivier for the precious help he gave me during my PhD and Bettina for the guidance and her cheery presence at the beginning of my thesis.

Before switching to French I would like to thank all the people of CP3 for the atmosphere over the past four years. In a non particular order, thanks a lot to Brieuc, Ioannis, Martin, Sébastien ($\times 2$), Nicolas, Eleni, Ambresh, Manoj, Gauthier, Adrien, Alexandre and Jérôme. Thanks a lot to my mathematician friends: Alban, Valentin, Natacha, Alexandra and Thierry. I would like to thank Gopi for the good time we had in Belgium and in USA. I also thank Sylvain, Olivier, Francisco, Jonathan and Arnaud. I apologize if some are missing.

Je voudrais particulièrement remercier Jean-Marc Gérard. Mon premier cours suivi à l'UCL fut le cours d'interactions fondamentales et tu m'as directement conforté dans mon choix de la physique des particules. J'ai énormément apprécié avoir réalisé mon mémoire avec toi, d'autant plus que celui-ci déboucha sur notre premier papier (et mon premier de surcroît). Je te remercie d'avoir toujours été ouvert à mes interrogations.

Je remercie Boon de tout coeur. Sans toi ce doctorat n'aurait pas eu la même saveur. Nous avons vécu tellement de péripéties durant ces quatre ans, à tel point que l'on pourrait en écrire un livre (mais pas le même que celui-ci). Tellement de fous rires aussi.

Maintenant j'aimerais remercier ceux sans qui je ne serais pas ce que je suis devenu aujourd'hui, à savoir ma famille. Maman et Papa, vous vous couperiez en quatre pour moi et je ne peux trouver de mots assez forts pour vous exprimer ma gratitude. Vous m'avez toujours soutenu dans mes choix. Estelle, nous avons toujours eu une relation fraternelle forte et je sais que nous pourrons tout le temps compter l'un sur l'autre dans la vie. Je vous remercie pour le soutien que vous m'avez accordé dans les moments les plus bas durant cette thèse. Je vous aime.

Un grand merci à Delphine qui a réussi à m'insuffler une touche d'optimisme au quotidien et qui a surtout réussi à me supporter ces derniers mois. Merci Chipmunk.

Je voudrais sincèrement remercier mes amis. Vous êtes une bouffée d'air frais pour moi. Thomas, cela fait tellement longtemps maintenant. Merci à Nico, Sarah, Chef, Julie, Will, Gilles, Lindsay, Galaad, Céline, Valentine et Pierre pour tous ces moments de détente. Merci à Loic de me permettre de me défouler au tennis. Merci à tous mes amis de l'UCL, Franky, Elo, Ricky, Maëlle, Jérôme, Kiff. Merci à tous les membres du BC MONS.

Finalement merci à tous ceux qui, de près ou de loin, ont contribué à mon épanouissement professionnel et/ou personnel.







This work has been supported by the IISN MadGraph convention 4.4511.10 and the IISN Fundamental interactions convention 4.4517.08, by the Belgian Federal Science Policy Office through the Interuniversity Attraction Pole P7/37 and by the ATTRACT - Brains back to Brussels grant from Innoviris.

Contents

Acknowledgements **3**

Foreword **11**

1 Introduction to dark matter **15**

1.1 Postulating the invisible 15

1.2 Early evidence of dark matter 17

1.3 The model of Big Bang 19

1.3.1 General relativity 20

1.3.2 From Big Bang to galaxy formation 23

1.3.3 Thermodynamics in the early Universe 25

1.3.4 Constraints on dark matter from the CMB 30

1.3.5 Structure formation 32

1.4 Gravitational lensing 33

1.5 The Standard Model of particle physics 34

1.6 Dark matter candidates 40

1.7 Dark matter detection 44

1.7.1 Indirect detection 44

1.7.2 Direct detection 46
1.7.3 Production at colliders 47

2 Dark matter simplified models at LHC 51
2.1 The s-channel mediator case 53
2.1.1 Spin-1 mediator model 54
2.1.2 Spin-0 mediator model 55
2.2 Dark matter production in association with jets 56
2.2.1 Total cross sections 59
2.2.2 Differential distributions 62
2.2.3 Comparison of signal distributions to the Standard Model . . 70
2.3 Dark matter production with a top-quark pair 71
2.3.1 Total cross sections 73
2.3.2 Differential distributions 76
2.4 Summary and comment on t-channel simplified models 76

3 MadDM: a numerical tool for dark matter physics 81
3.1 Review of direct detection and its implementation in MADDM 83
3.1.1 DM-nucleon elastic cross section 83
3.1.2 Projection operator method for extraction of low energy coefficients 85
3.1.3 Differential nucleus recoil rate 86
3.2 Validation 89
3.2.1 Validation of the DM-nucleon cross section calculation 89
3.2.2 Recoil rates 92
3.3 Summary and outlook 94

4 Exploration of simplified top-philic dark matter model 97

4.1 Simplified top-philic dark matter model and its numerical implementation 98

4.2 Cosmological and astrophysical constraints 104

4.2.1 Constraints from dark matter relic density 104

4.2.2 Constraints from direct detection 111

4.3 Collider constraints 114

4.3.1 Constraints from searches with missing transverse energy . . 116

4.3.2 Constraints from searches without missing transverse energy . 123

4.4 Combined constraints 127

Conclusion 131

Appendix A How to Use MadDM v.2.0 135

A.1 Structure of MADDM v.2.0 136

A.2 UFO Model Conventions 138

Appendix B Mediator width 141

Appendix C Recasting of LHC searches within the MADANALYSIS 5 framework 145

C.1 The CMS top-antitop plus missing energy search (CMS-B2G-14-004) 146

C.2 The CMS monojet search (CMS-EXO-12-048) 148

Appendix D Combined collider constraints 151

Bibliography 155

Foreword

The dark matter problem has the fascinating particularity to bring cosmology, astrophysics and particle physics closer. Astronomical and cosmological observations lead to the conclusion that a large amount of matter, that we call now dark matter, is invisible in the sense that only gravitational effects are detected. As the Standard Model of particle physics describes the Universe content in terms of particles and interactions among them, dark matter could also be described as (a) particle(s) interacting not only gravitationally.

The Standard Model has been strengthened over time, but its validity range is questionable above the electroweak scale. Therefore physics beyond the Standard Model is expected. Actually, a large variety of extensions of the Standard Model already exists. Among those extensions many dark matter candidates emerge and it would be really challenging to discriminate them in case of a discovery. Since such models of new physics grow complex and include many fields and many parameters, an alternative approach is preferred, called *simplified model approach*, where the model dependence is limited, yet the salient features that can provide a useful characterisation of possible signals are kept intact.

While the Standard Model structure has been extensively studied at colliders (*e.g.* at the Large Hadron Collider at CERN), such apparatus are not the only ones able to discover dark matter. Cosmological and astrophysical observations can also set constraints on model parameters from the measured dark matter abundance in the present Universe as well as from bounds on dark matter-nucleon cross section (direct detection experiments) and dark matter annihilation cross section into Standard Model particles (indirect detection experiments).

Making reliable predictions to be compared with data is a challenging task. The numerical tools used to compute collider quantities are already mature and linked to the

experimental analyses, while dark matter tools calculating cosmological and astrophysical quantities only started to be developed recently. In order to constrain dark matter models in an efficient way, considerable efforts have been made to provide an integrated framework.

In this thesis, we aim at combining cosmological, astrophysical and collider constraints on dark matter simplified models using all the technology available nowadays. In Chapter 1 we introduce cosmological and astrophysical evidence of dark matter. We also describe the model of the evolution of the Universe (Big Bang) introducing the thermodynamic processes that occur in the early Universe to produce both dark matter and baryonic elements today. We also explain the role of dark matter in the large structure formation in the Universe. In Chapter 2 we introduce the framework of dark matter simplified models and study the effects of quantum corrections for some physical processes at the Large Hadron Collider. In Chapter 3 we present MADDM, a numerical tool for dark matter phenomenology that computes both cosmological and astrophysical dark matter related quantities. Chapter 4 applies the simplified model approach of Chapter 2 for the particular case of a dark matter particle dominantly coupling via a scalar mediator to top quarks. We combine collider constraints with cosmological and astrophysical constraints coming from MADDM in order to have a full parameter space constrained by all possible dark matter searches.

The work presented in this thesis is based on the following publications:

- M. Backovic, M. Kramer, F. Maltoni, A. Martini, K. Mawatari and M. Pellen, *Higher-order QCD predictions for dark matter production at the LHC in simplified models with s-channel mediators*, Eur.Phys.J. **C75** (2015) no.10, 482, [arXiv:1508.05327]
- F. Maltoni, A. Martini, K. Mawatari and B. Oexl, *Signals of a superlight gravitino at the LHC*, JHEP **1504** (2015) 021, [arXiv:1502.01637]
- M. Backovic, A. Martini, O. Mattelaer, K. Kong and G. Mohlabeng, *Direct Detection of Dark Matter with MadDM v.2.0*, Phys. Dark Univ. **9-10** (2015) 37-50, [arXiv:1505.04190]
- C. Arina, M. Backovic, E. Conte, B. Fuks, J. Guo, J. Heisig, B. Hespel, M. Kramer, F. Maltoni, A. Martini, K. Mawatari, M. Pellen and E. Vryonidou, *A comprehensive approach to dark matter studies: exploration of simplified top-philic models*, JHEP **1611** (2016) 111, [arXiv:1605.09242]

Chapter 1 is a review of the dark matter concepts needed for the understanding of the following chapters and is then not based on a publication of the author. The major

contributions of the author to the aforementioned papers are the numerical building of the simplified models as well as the full numerical analysis in Ref. [1], the whole simulation part of Ref. [2], the implementation of the direct detection module of MADDM and its validation against a large bunch of toy models [3] and the analysis of various processes in the collider part of Ref. [4] (including the recasting of the CMS-B2G-14-004 analysis).

Chapter 1

Introduction to dark matter

"What we know is a drop, what we don't know is an ocean"

Sir Isaac Newton (1643 - 1727)

1.1 Postulating the invisible

Many times in the History, physicists have postulated the existence of invisible 'objects' to preserve established theories, sometimes with success, sometimes not. We present two successful and two unfortunate examples.

In the middle of the 19th century, the mechanical wave behaviour of light introduced by Huygens is commonly accepted thanks to the work of Thomas Young and Augustin Fresnel on diffraction of light. But a mechanical wave needs a medium to propagate in. Because light should propagate also in vacuum, Fresnel imagined a new invisible medium called *aether luminiferous* spread in the whole Universe [5]. The speed of light c is then a property of the aether. The aether has to be flexible in order to propagate transversal waves but also rigid to satisfy the huge speed propagation of light. At that time it is also natural to see the aether at rest in the absolute space of Newton (Let's not forget that at this epoch the time and distance intervals are invariant in classical mechanics). The principle of Galilean relativity stipulating that fundamental laws of physics have the same form in any inertial frame, has a weakness to define what is an inertial frame. Such a frame is then defined as fixed compared to a preferred frame, the absolute space of Newton. At the end of the century, Maxwell releases his

treatise on electromagnetism establishing that electric and magnetic fields can generate electromagnetic waves. In the Maxwell's equations, the propagation velocity c of the electromagnetic waves corresponds to the speed of light measured by Fizeau. This brings Maxwell to conclude that light is an electromagnetic wave and that the medium needed to propagate this wave is the aether luminoferous. Moreover, his equations would only be valid in the frame fixed to the aether *i.e.* the absolute space of Newton. However, finite velocities are not invariant in Galilean relativity and the speed of light should then be different in other inertial frames. The experiment led by Michelson and Morley using interferometer to detect the Earth's absolute motion is in contradiction with this conclusion, the speed of light is actually invariant. Einstein solves the problem arguing that Galilean transformations are not correct. Maxwell's equations are valid for any inertial frame implying that the speed of light is independent of the motion of the emitting body. They are also invariant under new transformations, the Lorentz transformations, leading to a new structure of space-time where the time and distance intervals are not absolute anymore. Special relativity was born and got rid of the aether as well as the vision of light as a mechanical wave.

A second and third example are the predictions from the French astronomer Nicolas Le Verrier about the existence of two new planets: Neptune and Vulcan [6]. In 1687, Newton publishes his *Principia Mathematica* containing his famous theory of gravitation. Le Verrier and the English astronomer John Couch Adams postulated the existence of Neptune based on anomalies in the Uranus motion. They computed with a substantial precision the location of this new planet and John Gall identified the planet at the Berlin observatory in the next few days. Later, Le Verrier tried to use the same argument to understand the anomalies in the precession of the perihelion of Mercury. He called the new potential planet *Vulcan* but this planet has never been observed. In 1915, the understanding of the Mercury anomaly arose from Einstein's theory of General Relativity.

Finally, the discovery of the neutrino is also a beautiful example of how physicists have postulated the invisible [7]. Radioactivity has been discovered in 1897 by Becquerel and its properties by Marie Curie and Ernest Rutherford. However, one property of radioactivity puzzled the physicists: the beta-decay. Indeed, they knew that radioactive sources can emit electrons, but they thought that each electron had a single energy like for alpha particle emission. Imagine how they were surprised when the experiment showed that the energy spectrum of beta electrons was continuous, in total contradiction with energy-momentum conservation for a 2-body decay process. The physicist Wolfgang Pauli postulated the existence of a third unseen particle coming along with the beta electron for a 3-body decay process to preserve the principle of energy-momentum conservation. A theory of the beta-decay emerged in 1932 from Enrico Fermi who called 'neutrino' the unseen particle of his theory. The discovery

of the neutrino was made in 1954 by Cowan and Reines using a hydrogenous material (water) detector next to a nuclear reactor to detect the reaction $\bar{\nu}_e + p \rightarrow n + e^+$.

The previous examples indicate that predicting the existence of a new object can be an attractive solution when the underlying theory seems well established. This was the case for the energy-momentum conservation with the missing neutrino and with the Newton's theory of gravitation for Neptune. However, we saw how it could be also dangerous in the case of the unseen Vulcan planet and the aether luminoferous. Postulating the invisible should always be taken with great care.

During the 20th century a new problem arose in our understanding of the Universe. The baryonic matter alone does not seem able to describe all the matter content of the Universe. A new kind of matter, unknown and invisible, called dark matter has been proposed to fill this hole. This thesis assumes that dark matter exists even if no non-gravitational evidence of its presence has been probed nowadays. Time and experiments will tell us if postulating this new invisible kind of matter was a mistake or a brilliant idea.

1.2 Early evidence of dark matter

At the end of the 19th century, astronomical photography was invented. Dark regions are observed in the sky but are they dark because they contain less stars or because of absorbing matter along the line-of-sight ? At that time most of the observations rely on the mass to star luminosity fraction M/L. The reference number is the Sun with $M_\odot/L_\odot = 1$. Then if we measure the light emission from a distant object (*e.g.* a star, a galaxy or a cluster of galaxies) we can estimate its mass [8]. However, another way to determine the mass of a body is to record the motion of the other objects around the body under study. Lord Kelvin appears as a pioneer of this method when he argued for a dynamical determination of the amount of matter in the Milky Way using the velocity dispersion of the stars [6]. Indeed, we can think the Milky Way as a gas of particles interacting gravitationally. Jan Oort (1932) applied this method to determine the local density of matter in the neighbourhood of the Sun. Using the dynamical data, he could derive a local matter density of $0.092\ M_\odot/\mathrm{pc}^3$. Be aware that this number corresponds to the sum of contributions coming from visible and invisible (or *dark*) matter. To estimate the local density of dark matter, Oort subtracted from this number the density of visible matter based on the contributions from the stars. He concluded that the total mass of dark matter is probably less than the total mass of visible stars [9]. However, later re-examination (also from Oort himself) of the local density of matter led to the conclusion that the amount of dark matter is around half of the amount of visible matter.

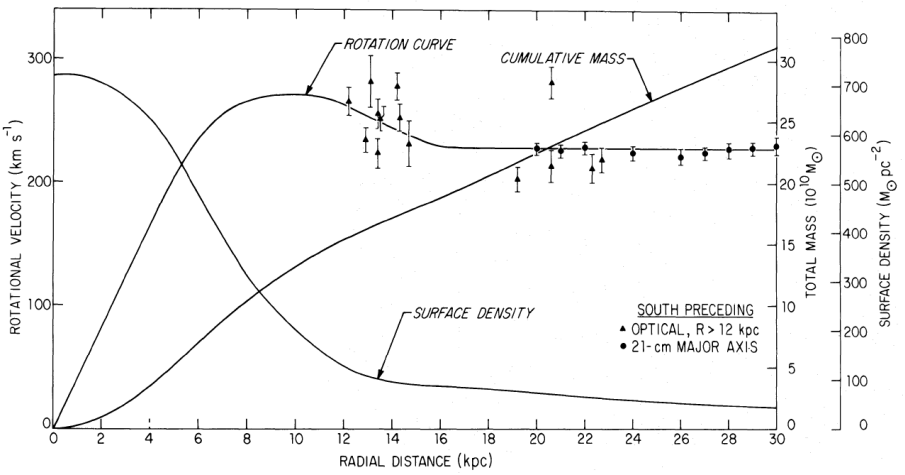


Figure 1.1: The rotation curve of Andromeda galaxy by Roberts and Whitehurst (1975) [10]. Triangles show the optical data from Rubin and Ford (1970). Circles show measurements made by radio telescope.

On a larger scale Zwicky studied the global density of matter in the Coma cluster of galaxies ($99\ \mathrm{Mpc}$ from Earth). He measured the redshifts of galaxies in the cluster and found that the velocity dispersion of these galaxies was much higher than expected. Zwicky applied the virial theorem for the first time for this kind of problem to compute the cluster mass. In this case the virial theorem says that we can relate the gravitational potential energy to the kinetic energy of the system

$$\langle T \rangle + \frac{1}{2} \langle U \rangle = 0, \tag{1.1}$$

where $\langle T \rangle$ is the mean kinetic energy and $\langle U \rangle$ is the mean potential energy. Zwicky extracted the mass of the cluster getting a value of $M_{cluster} = 4.5 \times 10^{13}\ M_{\odot}$. Surprisingly, the estimate from mass to luminosity fraction counts for only 2% of this number. Then most of the Coma cluster consists of invisible matter. This result of Zwicky is often considered as the first major evidence of dark matter in the Universe.

Another impressive evidence of dark matter comes from the 70s. Vera Rubin and Kent Ford improved a spectrograph coupled to a photomultiplier to record the velocity of stars in the Andromeda galaxy (M31). From Newtonian dynamics we know that the stars around the galactic centre should behave like the planets in the solar system *i.e.* their speed should decrease with the distance from the centre. This is known as

Keplerian behaviour. From Newton's law of motion we get

$$ma = m\frac{v^2}{r} = \frac{GmM(r)}{r^2}, \tag{1.2}$$

where m and v are the mass and the speed of the star, G is the gravitational constant of Newton and $M(r)$ the mass enclosed in the radius r from the centre of the galaxy to the star under study. Then we can extract the expression for the speed of the star

$$v = \sqrt{\frac{GM(r)}{r}}. \tag{1.3}$$

For the solar system, $M(r)$ is essentially the Sun mass, leading to $v \propto 1/\sqrt{r}$ *i.e.* , that the speed of planets decreases with r. For the Andromeda galaxy the general behaviour should be roughly the same because most of the luminous matter comes from the galactic centre. However, Fig. 1.1 shows the results of Roberts and Whitehurst containing Rubin and Ford data. They found that the galaxy rotation curve has a tail that remains flat, that could be explained if $M(r)$ is proportional to r then growing with the distance. In total contradiction with the density of visible stars in M31 they argued that invisible matter could explain this unexpected result. This flatness property has been observed on many spiral galaxies afterwards.

All these early observations seem to indicate the existence of dark matter in the Universe. However, the pioneers of dark matter that we mentioned in the previous paragraphs did not have in mind the same meaning of what we call dark matter nowadays. For them dark matter was only invisible baryonic matter *i.e.* dark bodies that they could not see with their technical setup for many different reasons. However, we do know today that dark matter is non-baryonic and has nothing to do with ordinary matter. The word *dark* is not just an adjective anymore but has a particular meaning in cosmology and particle physics. In the next sections we introduce the model of Big Bang to finally understand why dark matter (DM) should be non-baryonic.

1.3 The model of Big Bang

In order to understand the nature and the role of DM in the Universe we need to examine the thermal history of the early Universe. What are the big steps and mechanisms that will help us to constrain the abundances of baryonic matter and DM ? What is the role of DM in the structure formation in the Universe ? Here are the questions needing an answer. This section is based on Ref. [11].

1.3.1 General relativity

So far, all the evidence for DM is gravitational. Therefore, we need to introduce the Einstein's theory of gravitation. After the success of special relativity, Einstein addressed an issue to the Newton's theory of gravity. The later includes an instantaneous long range interaction in contradiction with the causal structure of special relativity. In addition, we saw that the anomaly in the motion of the perihelion of Mercury was still a mystery.

The first law of motion by Newton and Einstein stipulates that inertial frames are a specific class of frames where the laws of physics remain the same. Nevertheless, the existence of this kind of special frame is anything but obvious. Only experience can validate if a frame is inertial or not. The way to proceed is to verify that a test particle has a rectilinear movement if no external fields affect it. While we can ensure this condition for other fundamental forces like electromagnetism, it is impossible for gravity since the weak equivalence principle stipulates that the inertial mass is equivalent to the gravitational mass. Therefore, the resulting acceleration is independent from the mass and we can not distinguish a frame at rest in a gravitational field from an accelerated frame. The absolute concept of acceleration vanishes as well as the concept of free particle. Fortunately, we can always eliminate locally the effects of an external gravitational field by using the free fall inertial frame. This comes from the Einstein's idea that a person does not feel her weight in a free fall. In this particular frame, the laws of mechanics from Einstein and Newton remain valid. This constitutes the essence of the Einstein equivalence principle.

In the absence of gravity, we can consider the flat space-time of special relativity with the Minkowski metric $\eta_{\mu\nu} = \mathrm{diag}\,(1, -1, -1, -1)$, where we can pass from an inertial frame to another via the linear Lorentz transformations. In this framework all inertial observers are equivalent. However, in the presence of gravity we have a curved space-time with a metric $g_{\mu\nu}(x)$ depending on coordinates. The coordinate transformations to go from the experimental laboratory to a frame in free fall are not linear anymore. The Einstein equivalence principle implies that the Einstein's mechanics is still valid locally for each observer along a geodesic G which is the shortest path from one point to another in the curved space-time, the geodesic being the curve of free fall ($g_{\mu\nu}(G) = \eta_{\mu\nu}$). Gravity acts as a fictitious force in the Newton's theory as it is the case for any metric theory. The Einstein equivalence principle is then an extension of the relativity principle from inertial observer to any observer, inertial or not. Every physicist should be able to discover the laws of Nature in any frame.

The general relativity principle defines a dynamical space-time affecting and affected by its mass and energy content. In this framework, any free body *i.e.* influenced by gravitation only, follows a geodesic in a curved space-time. The equations of General

Relativity are

$$R_{\mu\nu} - \frac{1}{2}Rg_{\mu\nu} - \Lambda g_{\mu\nu} = \kappa T_{\mu\nu}, \tag{1.4}$$

where $R_{\mu\nu}$ is the Ricci tensor, R the curvature scalar, $T_{\mu\nu}$ the momentum tensor associated to the system under study, Λ the cosmological constant and $\kappa = 8\pi G/c^4$ with G the gravitational constant of Newton. Solving Eq. (1.4) leads to an expression for the metric $g_{\mu\nu}(x)$. For example Einstein's equations applied to a star allow to understand the space-time structure inside and outside the star itself. Also phenomena as deflection of light around a body and the anomaly of the perihelion of Mercury find an explanation.

Then we can apply the Einstein's equations to the Universe itself. What are the solutions of Eq. (1.4) describing our Universe ? To answer this question we need to make some assumptions about the structure of the Universe. Galaxies are considered as point-like objects constituting the Universe. Two assumptions are commonly used forming what we call the cosmological principle. Firstly, the Universe is isotropic meaning that the number of galaxies is in average the same in every direction. Secondly, the position of an observer has no effect on physical properties of the Universe (universality). Based on this assumption of universality, the Universe is homogeneous in the sense that for two same volumes the number of contained galaxies is the same. Moreover the universality requires a constant spatial curvature in the Universe. Based on these assumptions the solution of Eq. (1.4) will respect the cosmological principle. Therefore, we can parametrise the metric of the Universe as

$$ds^2 = c^2dt^2 - a^2(t)\left[\frac{d\sigma^2}{1-k\sigma^2} + \sigma^2 d\Omega^2\right] (\text{Robertson} - \text{Walker}), \tag{1.5}$$

where t is the proper time associated to each observer in the Universe, $a(t)$ is the scale factor related to the expansion rate of the Universe through the Hubble factor $H(t) = \dot{a}(t)/a(t)$, $\sigma = r/a$ is a dimensionless factor related to radial coordinate r, $d\Omega = d\theta^2 + \sin^2(\theta)d\varphi^2$ is the usual sphere element in spherical coordinates and $k = 0, \pm 1$ is related to the curvature of the Universe ; $k = 0$ corresponds to a flat space-time (hyperplan) while $k = \pm 1$ corresponds to an hypersphere or a pseudo-sphere when k is positive or negative, respectively. A galaxy is then dust in free fall in a perfect fluid and its spatial coordinates are the comoving coordinates $(\sigma, \theta, \varphi)$.

The energy-momentum tensor associated to the Universe according to the cosmological principle is the one associated to a perfect fluid

$$T_{\mu\nu} = \left(\rho + \frac{p}{c^2}\right) u_\mu u_\nu - p g_{\mu\nu}, \tag{1.6}$$

where ρ and p are the energy density and pressure measured by the comoving observer. u_μ is the four-velocity. If we insert the Robertson-Walker metric and the

energy-momentum tensor in the Einstein's equations we get the Friedmann-Lemaître equations

$$\left(\frac{\dot{a}}{a}\right)^2 + \frac{kc^2}{a^2} - \frac{\Lambda c^2}{3} = \frac{8\pi G}{3}\rho \tag{1.7}$$

$$\frac{\ddot{a}}{a} - \frac{\Lambda c^2}{3} = -\frac{4\pi G}{3}\left(\rho + \frac{3p}{c^2}\right), \tag{1.8}$$

which describe the evolution of the Universe in terms of 4 physical parameters: the geometric parameter k, the cosmological constant Λ related to dark energy, the energy density $\rho > 0$ and the pressure p. Depending on the choice for these parameters the Universe behaves differently. A third equation comes from the equation of conservation of matter

$$\dot{\rho} + 3H\left(\rho + P\right) = 0, \tag{1.9}$$

but is not independent from Eqs. (1.7) and (1.8). Therefore, we need a fourth equation to solve the system: the state equation. Indeed, energy density and pressure of a fluid are linked through an equation of state

$$p = \omega\rho. \tag{1.10}$$

Radiation is characterised by $\omega = 1/3$, matter without pressure by $\omega = 0$ and the fluid associated to the cosmological constant by $\omega = -1$. For a constant value of ω, Eq. (1.9) implies that

$$\rho \propto a^{-3(1+\omega)}. \tag{1.11}$$

We can re-write Eq. (1.7) in a reduced form

$$\Omega_M + \Omega_\Lambda = 1 + \frac{kc^2}{a^2H^2}, \tag{1.12}$$

where

$$\Omega_M = \frac{8\pi G\rho_M}{3H^2} = \frac{\rho_M}{\rho_c}, \qquad \Omega_\Lambda = \frac{\Lambda c^2}{3H^2} = \frac{\rho_\Lambda}{\rho_c} \tag{1.13}$$

are dimensionless cosmological variables describing the energy density of matter ρ_M and the energy density of the fluid associated to the cosmological constant ρ_Λ as fraction of the critical energy density ρ_c. The component of total matter Ω_M contains the matter Ω_m ($\omega = 0$) and the radiation Ω_r ($\omega = 1/3$) themselves divided in baryons Ω_b, DM Ω_{DM} and photons Ω_γ, neutrinos Ω_ν, respectively. Each cosmological variable evolves differently with time obeying their own equation of state. The critical energy density corresponds to the energy density for which the space-time is characterised by

$k = \Lambda = 0$ *i.e.* the boundary between a closed Universe ($k > 0$) and an open one ($k < 0$).

From the 2015 Planck satellite results on *cosmic microwave background* (CMB, see Section 1.3.4), the data favour a flat and dynamical space-time ($k = 0$ and $\Lambda > 0$). The energy content of the present Universe is then characterised by $\Omega_M^0 + \Omega_\Lambda^0 = 1$ with

$$\Omega_M^0 = 0.308 \pm 0.012, \qquad \Omega_\Lambda^0 = 0.692 \pm 0.012. \tag{1.14}$$

These measurements show that about 30% of the energy content of the present Universe is made of matter while the 70% remaining consists of dark energy. Moreover the Planck results show that matter contains about 15% of ordinary matter while the 85% remaining consists of DM. On top of that, the present value of the Hubble parameter, H_0, is $H_0 = 67.8 \pm 0.9\ \mathrm{km\,s^{-1}Mpc^{-1}}$ [12].

We will explain later what is the CMB and how we could extract the cosmological parameters from the experiment. For the moment the important result is that the General Relativity framework associated to the cosmological principle can model an expanding Universe and its energy content. Now, we introduce the Big Bang model in the framework of General Relativity to understand the evolution of the Universe from the Big Bang to the present time.

1.3.2 From Big Bang to galaxy formation

Beyond the Planck scale (10^{19} GeV) we do not have any clue of the physics of the Universe. During the next 10^{-43} s following the Big Bang, a quantum theory of gravity is necessary. A few modern theories like string theory or loop quantum theory attempt to set up a coherent framework but they suffer from the problem of falsification *i.e.* there is no way to test these theories against the experiment with the resources (*e.g.* particle accelerators) we have. From 10^{-43} s to 10^{-36} s after Big Bang, the era of grand unification occurs. Gravity decouples from the other three fundamental forces that are still unified at that time. Then the Universe starts a brief period of very strong homogeneous and isotropic expansion called *inflation*. At the end of this epoch, a very dense and hot plasma containing photons, quarks, electrons and neutrinos remains. Actual theories do not explain convincingly why there is such a discrepancy between the number of particles compared to the number of anti-particles. The process that would produce this asymmetry is called *baryogenesis*. When the Universe continues to cool down, the electroweak force, already decoupled from the strong force, spontaneously breaks down and the final result is the four fundamental forces we know today. Then the hadrons, bound states of quarks, annihilate with anti-hadrons like leptons and anti-leptons do, bringing us to $10\,\mathrm{s}$ after Big Bang when the Universe

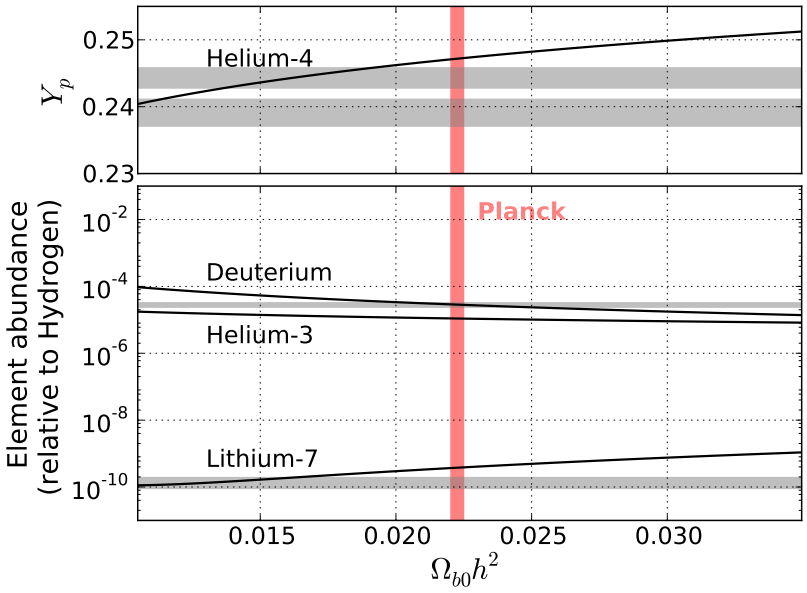


Figure 1.2: Abundances of Deuterium, Helium-3, Helium-4 and Lithium nuclei relative to hydrogen. $Y_p = \frac{2(n/p)}{1+n/p}$ corresponds to the primordial mass fraction of Helium-4 which depends on the neutron fraction n/p. The gray areas correspond to the spectroscopic observations from astrophysics for Helium-4, Deuterium and Lithium-7. In red, the Planck measurement on the baryonic content of the present Universe.

is dominated by radiation. At that time neutrinos have already decoupled from the thermal bath.

At this epoch, the radiation-dominated Universe is still so hot and dense that protons and neutrons can not bind into deuterium nuclei without being impacted by high-energy photons. When the Universe expands, the high energy photons become rare enough to allow the deuterium nuclei production to be efficient. Then other nucleons can stick into the deuterium to produce higher atomic number nuclei: tritium, helium-3, helium-4, lithium and beryllium. Producing heavier nuclei is complicated due to a stronger Coulomb barrier and the absence of stable nuclei with atomic number $A = 5$ and $A = 8$. This mechanism of production of nuclei is called *nucleosynthesis*. Nucleosynthesis occurs when the temperature of the Universe is in the range 0.7-0.05 MeV; this corresponds to a small window of about 15 minutes in time. Because of the drop of temperature when the Universe expands, the density of protons and neutrons falls down, but neutrons are unstable if not bound into nuclei. Around a temperature of 0.05 MeV the neutrons decay and the nucleosynthesis mechanism stops. All the nu-

clei content of the Universe is fixed at that time. Using thermodynamic principles that we will develop in the next section, it is possible to compute the abundance of all the produced nuclei during nucleosynthesis. After nucleosynthesis, the Universe contains three times more hydrogen nuclei than helium-4 nuclei, with only a little abundance for the others (Fig. 1.2). Data from astronomical spectroscopy can give an estimate on the density of baryons to the density of radiation fraction, $\eta \equiv n_b/n_\gamma$,

$$\eta = (5.15 \pm 1.75) \times 10^{-10}, \tag{1.15}$$

corresponding to a baryonic content in the present Universe $\Omega_{b0}h^2 = 0.018 \pm 0.006$, which is much smaller than the total amount of matter in the Universe (Eq. (1.14)). $h = H_0/(100 \text{ km s}^{-1} \text{ Mpc}^{-1})$ corresponds to the reduced Hubble constant. Finally, we would like to point out that while the prediction of the abundances of light elements during nucleosynthesis seems in agreement with observations coming from spectroscopy, a discrepancy appears for the Lithium-7 [13]. Such a tension with the model of Big Bang should always remember us that the predictions always assume the validity of General Relativity. We should keep this Lithium problem in mind even if some possible solutions have been exposed recently [14].

After a long period of expansion (around 70 000 years) the density of matter equals the density of photons. The first structures of the Universe start to form. However, the temperature is still too hot to allow hydrogen atoms to form, the photons being strongly coupled to the electrons. As the Universe keeps expanding, thermodynamics favours the formation of neutral atoms. The electrons stick to nuclei and the Universe becomes neutral. This process is called *recombination* and occurs around 3×10^5 years after Big Bang. At that time the Universe becomes transparent since photons can then decouple from the thermal bath and travel freely in the Universe. This decoupling event corresponds to the last scattering surface of photons and electrons. These photons which escaped from the cosmic bath are still visible today and constitute what we call the CMB. The CMB was predicted by Alpher and Herman in 1948 and discovered by Wilson and Penzias who recorded an isotropic microwave signal filling the whole sky at a temperature of 3.5 K. Analyses of the CMB by the Planck collaboration give a more precise value for the baryonic content in the Universe today $\Omega_{b0}h^2 = 0.02226 \pm 0.00023$ [12].

1.3.3 Thermodynamics in the early Universe

Now that we draw a global picture of the story of the Universe in the previous section, we need to introduce the thermodynamic processes that occur in the hot thermal bath of the Universe [11, 15–17]. These mechanisms are at the origin of nucleosynthesis as

well as photons, neutrinos and DM decoupling. It is necessary to cover the thermodynamics in the early Universe to understand the abundances of species when they are in thermal equilibrium and when they fall out of it.

Imagine that in the thermal bath of the Universe, a stable particle X of mass m interacts with a particle Y through some processes $X\bar{X} \leftrightarrow Y\bar{Y}$. We define Γ as the rate at which these processes occur. If Γ is much bigger than the Hubble expansion rate then a thermodynamic equilibrium can be maintained by the interacting particles at a temperature T. In that case we can consider these particles together as a Fermi-Dirac gas or a Bose-Einstein gas depending on the nature of the particles, fermionic or bosonic, respectively. The distribution function of such gas *i.e.* the statistical number of particles with an energy E at a temperature T, is

$$F_i\left(E,T\right) = \frac{g_i}{(2\pi)^3}\frac{1}{e^{[(E-\mu_i)/T_i(t)]}\pm 1} \equiv \frac{g_i}{(2\pi)^3} f_i\left(E,T\right), \tag{1.16}$$

where g_i is the degeneracy factor, μ_i the chemical potential and $T_i(t)$ is the temperate associated to the species under study. Particles interacting together will have the same temperature. Since the Universe contains radiation with a black body spectrum, every species interacting with photons will have a temperature T that we call *temperature of the Universe*.

From Eq. (1.16) we can define the particle density n, the energy density ρ and the pressure p of fluids as

$$n_i(t) = \int F_i(\mathbf{p},T)\, d^3\mathbf{p} = \frac{g_i}{2\pi^2}\int_m^\infty \frac{\sqrt{E^2-m^2}EdE}{e^{[(E-\mu_i)/T_i(t)]}\pm 1} \tag{1.17}$$

$$\rho_i(t) = \int F_i(\mathbf{p},T)E(\mathbf{p})\, d^3\mathbf{p} = \frac{g_i}{2\pi^2}\int_m^\infty \frac{\sqrt{E^2-m^2}E^2dE}{e^{[(E-\mu_i)/T_i(t)]}\pm 1} \tag{1.18}$$

$$p_i(t) = \int F_i(\mathbf{p},T)\frac{p^2}{3E}\, d^3\mathbf{p} = \frac{g_i}{6\pi^2}\int_m^\infty \frac{\left(E^2-m^2\right)^{3/2}dE}{e^{[(E-\mu_i)/T_i(t)]}\pm 1}. \tag{1.19}$$

Then we can particularise particle density for different limits for fermions and bosons. When $T \gg m$, we get

$$n = g\left(\zeta(3)/\pi^2\right)T^3 \qquad \text{(boson)} \tag{1.20}$$

$$n = g\left(3\zeta(3)/4\pi^2\right)T^3 \qquad \text{(fermion)}, \tag{1.21}$$

while when $T \ll m$, the expressions become

$$n = g\left(mT/2\pi\right)^{3/2} e^{(\mu-m)/T} \qquad \text{(boson and fermion)}, \tag{1.22}$$

where $\zeta(3) \simeq 1.202$ is the value of the Riemann zeta function in 3.

We can then define the entropy s of the early Universe as

$$s = \frac{2\pi^2}{45} q_* T^3, \tag{1.23}$$

where $q_*(T)$ is the number of relativistic degree of freedom at temperature T. Assuming that the Universe is in adiabatic expansion, we have $d(sa^3) = 0$ *i.e.* $sa^3 = \text{const}$, encoding the entropy conservation in an expanding Universe. In a similar way as for entropy, we can define the energy density by counting the number of relativistic degrees of freedom for a particular temperature

$$\rho = \frac{\pi^2}{30} g_* T^4. \tag{1.24}$$

If no annihilation or creation of matter occurs, the number of particles does not change in a given volume ($N \propto na^3$) and the conservation of entropy in an expanding Universe allows us to define a useful variable,

$$Y = \frac{n}{s}, \tag{1.25}$$

which represents the number of particles per comoving volume.

From Eq. (1.22) we realise that if particles had to stay in equilibrium when the Universe cools down, the particle density would decrease exponentially to reach an insignificant value today. To prevent this scenario there are a few number of mechanisms available. For example the asymmetry between the number of baryons and anti-baryons in the early Universe implies that even when all anti-baryons annihilate with baryons, a small residual of baryons still remains today. Thus an asymmetry could be at the origin of the existence of a particle residual. However, there is another simpler way to create a particle density residual: the *freeze-out* mechanism. When the Universe expands, the annihilation of a particle X with its anti-particle $\bar{X}$ could not be sufficient enough to maintain the thermal equilibrium meaning that $\Gamma < H$. At that point the thermodynamics at equilibrium is not valid anymore and the annihilation process is described by the Boltzmann equation

$$\frac{dn_X}{dt} + 3Hn_X = -\langle \sigma_{X\bar{X}} |v| \rangle \left(n_X^2 - n_{X,\text{eq}}^2 \right), \tag{1.26}$$

which competes the effects of Universe expansion and particle annihilation. $\langle \sigma_{X\bar{X}} |v| \rangle$ corresponds to the thermally averaged $X\bar{X}$ annihilation cross section and $n_{X,\text{eq}}$ to the density of particle X at equilibrium *i.e.* obeying to Eq. (1.22) for a non-relativistic particle. We re-write Eq. (1.26) by tracking the number of particles X per unit of entropy Y,

$$\frac{dY}{dt} = -\langle \sigma_{X\bar{X}} |v| \rangle \, s \left(Y^2 - Y_{\text{eq}}^2 \right), \tag{1.27}$$

since $s\,(dY/dt) = dn_X/dt + 3Hn_X$. Using $x = m/T$, the Boltzmann equation becomes

$$\frac{dY}{dx} = -\left\langle \sigma_{X\bar{X}}\,|v| \right\rangle \frac{s}{Hx}\left(Y^2 - Y_{\rm eq}^2\right). \tag{1.28}$$

This equation can be solved by numerical integration. At some temperature x_f, the annihilation can not be maintained because of the Universe expansion. At that time, particles X decouple from the thermal bath and we get a number of particles per unit of entropy Y_∞ constant until today. This residual density is called a *relic* and the precise moment when the decoupling occurs is called the *freeze-out*. Then using $n_{X0} = s_0 Y_\infty$ and $\rho_{X0} = m\, n_{X0}$, we can get the relic density $\Omega_X h^2 = \rho_X/\rho_c\, h^2$.

Two major kinds of relics emerge: *hot relic* and *cold relic*. Hot relic stands for particles that decouple from the thermal bath when they are still ultra-relativistic such that

$$Y_{\rm eq} = \frac{45\zeta(3)}{2\pi^4}\epsilon_{\rm FB}\frac{g_X}{q_*}, \tag{1.29}$$

with $\epsilon_{\rm FB} = 1$ (boson) or $3/4$ (fermion). The interaction stops to be efficient while $Y_{\rm eq}$ is constant. Thus the relic density is given by the value at equilibrium

$$Y_\infty = Y_{\rm eq}(x_f) = \frac{45\zeta(3)}{2\pi^4}\epsilon_{\rm FB}\frac{g_X}{q_*}. \tag{1.30}$$

This is for example the case when neutrinos decouple in the early Universe.

On the other hand, if the freeze-out occurs when particles are non-relativistic, the relics are called cold. For a non-relativistic particle we have

$$Y_{\rm eq} = \frac{45}{2\pi^4}\sqrt{\frac{\pi}{8}}\frac{g_X}{q_*}x^{3/2}e^{-x}. \tag{1.31}$$

With this expression we can solve the Boltzmann equation (1.28) analytically in the two limit regions $1 < x \ll x_f$ (before freeze-out) and $x \gg x_f$ (after freeze-out). Before freeze-out $Y \simeq Y_{\rm eq}$ and the density of particles X is roughly equal to its value at equilibrium. However, after freeze-out, $Y_{\rm eq}$ is exponentially suppressed and the first term on the right side of Eq. (1.27) is small compared to the expansion term of the left side for small values of particle density. When it happens, Y becomes fixed and the thermal freeze-out occurs. The relic density $\Omega_X h^2$ can be obtained by integrating the boltzmann equation from the freeze-out temperature x_f to infinity

$$\Omega_X h^2 \equiv \frac{\rho_X}{\rho_c}h^2 = \frac{mY_\infty s_0}{1.05\times10^{-5}\ {\rm GeV}^2{\rm cm}^{-3}}, \tag{1.32}$$

where $s_0 = 2889.2\,{\rm cm}^{-3}$ is the entropy density today. On Fig. 1.3 we see from numerical integration of the Boltzmann equation that a smaller value of the thermally averaged cross section leads to bigger value of relic density, and inversely.

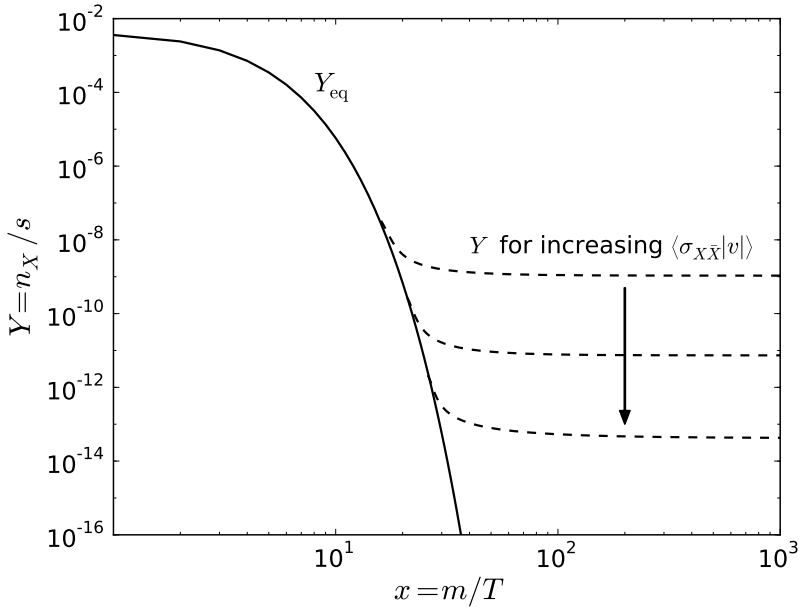


Figure 1.3: Decoupling of X from the thermal equilibrium (freeze-out mechanism). For increasing thermally averaged $X\bar{X}$ annihilation cross section, the value of Y_∞ decreases leading to smaller relic abundance of X.

On top of $X\bar{X}$ annihilation, a particle X can co-annihilate with a particle X'. Such a process $X\bar{X}' \to Y\bar{Y}$ can have a non negligible impact on the relic density of X if $m_{X'} > m_X$ within 10%, roughly. For example co-annihilation happens in super-symmetric models where the neutralino DM co-annihilates with stau or sleptons. The condition for co-annihilation to be an efficient process contributing to relic density is a non-negligible density of particles X' at the freeze-out time of X. The relative energy density at freeze-out time for two (non-relativistic) species can be estimated by

$$\frac{n_{X'}}{n_X} \sim \frac{e^{-m_{X'}/T_f}}{e^{-m_X/T_f}}. \tag{1.33}$$

If we consider a typical freeze-out temperature of $x_f = 20$, X' would be completely irrelevant if its mass is not within 10% of the mass of X. In order to quantify the impact of co-annihilation in the relic density calculation, we adapt Eq. (1.26) as

$$\frac{dn_X}{dt} + 3Hn_X = -\sum_{i,j=1}^{N} \langle\sigma_{ij}\,|v_{ij}|\rangle \left(n_i n_j - n_i^{\rm eq} n_j^{\rm eq}\right), \tag{1.34}$$

where $\sigma_{ij} = \sigma\left(X_i X_j \to Y\bar{Y}\right)$, assuming N particles X_i ($i = 1, \ldots, N$) decaying into the lightest one X_1 (denoted X) if they survive annihilation. Therefore $n_X =$

$\sum_{i=1}^{N} n_i$. Eq. (1.34) can also be written as Eq. (1.26) if we use the approximation $n_i/n_X = n_i^{\rm eq}/n_X^{\rm eq}$ [18]. We then obtain

$$\frac{dn_X}{dt} + 3Hn_X = -\left\langle \sigma_{\rm eff}\left|v\right|\right\rangle \left(n_X^2 - n_{X,\rm eq}^2\right), \tag{1.35}$$

with

$$\left\langle \sigma_{\rm eff}\left|v\right|\right\rangle = \sum_{i,j} \left\langle \sigma_{ij} v_{ij}\right\rangle \frac{n_i^{\rm eq}}{n_X^{\rm eq}} \frac{n_j^{\rm eq}}{n_X^{\rm eq}}. \tag{1.36}$$

Solving Eq. (1.35) leads to the relic abundance of the lightest stable particle X.

Applying the thermodynamics to the early Universe gives an explanation to the abundance of the nuclei after nucleosynthesis as well as for the freeze-out of the weak interaction and the relic density of DM (assuming that DM is in thermal equilibrium in the early Universe). In the next section we show how the CMB sets constraints on baryonic and DM abundances.

1.3.4 Constraints on dark matter from the CMB

The first space mission to probe the CMB was launched in 1989 by NASA with the COBE satellite (COsmic Background Explorer). COBE reported an isotropic microwave signal in the whole sky matching with a black body spectrum at a temperature of 2.73 K. Nevertheless, some small anisotropies have been highlighted by COBE, on the order of 1 part in 10^5 across the sky [19]. In 2001, the WMAP satellite (Wilkinson Microwave Anisotropy Probe) succeeded to study these anisotropies with a much higher temperature resolution for the sky map [20]. The latest results on CMB come from the Planck satellite launched in 2011. In 2015, the latest analysed results from Planck show an incredible micro-Kelvin precision for the whole sky map in several microwave frequencies, leading to the most precise measurement of CMB anisotropies ever [12]. That kind of experiment needs also a broad frequency coverage of the sky in order to separate the Galactic foreground from the CMB anisotropies. The result is a couple of maps for different frequencies.

As we observe the CMB as a sphere around us, we can expand the temperature anisotropies of the CMB into spherical harmonics $Y_{lm}(\theta,\varphi)$ and extract their coefficients a_{lm}

$$\frac{\delta T}{T}(\theta,\varphi) = \sum_{l,m} a_{lm} Y_{lm}(\theta,\varphi). \tag{1.37}$$

If we define the coefficients C_l as

$$C_l = \frac{1}{2l+1} \sum_{m=-l}^{l} |a_{lm}|^2, \tag{1.38}$$

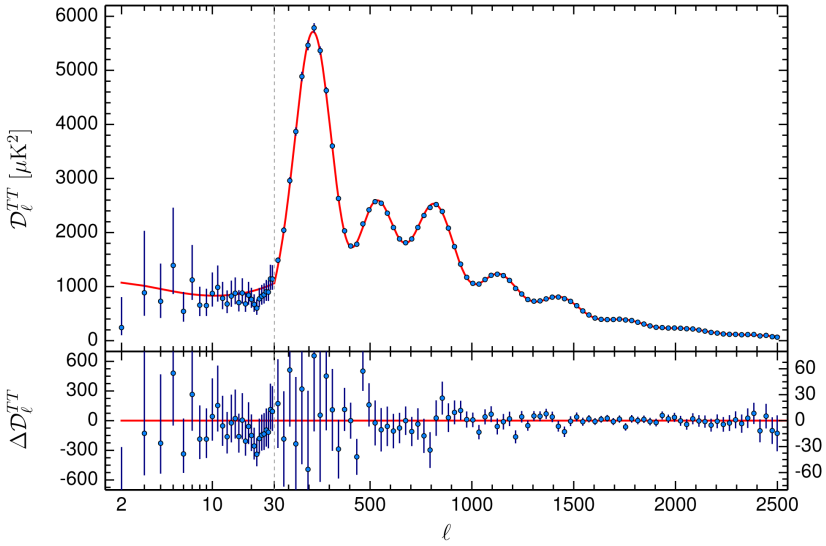


Figure 1.4: Planck 2015 temperature power spectrum [12].

the angular power spectrum associated to the CMB maps gives us essentially the behaviour of C_l as a function of l and the quantity $\mathcal{D}_l^{TT} = l(l+1)C_l/2\pi$ usually appears on plots. Note that the measurements will not exactly match the theoretical expectations since we measure the fluctuations averaged over the surface of last scattering. However, the possible statistical fluctuations are expected to cancel when averaging over m, especially for large values of l.

The shape of the angular power spectrum can be parametrised in terms of cosmological parameters $\Omega_b h^2$, $\Omega_m h^2$, the fraction between baryonic matter and DM, the Hubble constant, the cosmological constant and the curvature. The position of the peaks (Fig. 1.4) can be altered when the value of these parameters changes. For example the baryonic density fixes the relative amplitudes of the pair and impair peaks. Planck gives the following results for the relic density of baryons and DM in the Universe, respectively :

$$\Omega_b h^2 = 0.02226 \pm 0.00023 \qquad \Omega_{\rm DM} h^2 = 0.1186 \pm 0.0020. \tag{1.39}$$

Thus the CMB proves that around 85% of the matter content of the Universe is made of DM and the result is in agreement with the constraints from nucleosynthesis.

Another feature that we can learn from CMB anisotropies concerns the large scale structure of the Universe. Before the recombination the perpetual competition between gravity, that tends to clump particles together, and the radiation pressure , that

breaks this effort, prevents the large structures of the Universe to form. However, when the Universe becomes transparent, gravity has the opportunity to start the process. The small anisotropies of the CMB can be seen as the primordial inhomogeneities that will lead to the formation of galaxies and galaxy clusters.

1.3.5 Structure formation

From the observations of structures as galaxies, galaxy clusters and stars, it is clear that the Universe is not homogeneous and isotropic at that scale while this approximation is valid at larger scales as we have seen in the previous sections. In order to give a convincing explanation to the process of structure formation we have to come back to the inhomogeneities which can grow after recombination.

First, one can wonder if baryonic DM could explain the structure formation if we throw off the results on the baryonic density. Actually baryonic matter could not form the Universe structures we know today. From N-body simulations of gas particles we know that the anisotropies of the CMB we measured should have been much bigger to form the present Universe. Baryonic matter did not seem to have enough time to grow the primordial inhomogeneities in such distributions of galaxies. The cosmic bath of the early Universe does not allow baryonic matter to set up primordial inhomogeneities since the radiation is preventing it. When the Universe tends to be matter dominated it is too late for baryonic matter to form the Universe we know today.

However, non-baryonic DM can explain the structure formation in the Universe. Since DM does not interact with photons, primordial inhomogeneities can occur earlier than the matter dominated epoch. Then when the Universe becomes transparent, DM traps the baryonic matter in the created inhomogeneities leading to the present Universe. Nevertheless we know that DM can be hot or cold. These two types of DM lead to a different way of clumping matter into galaxies or clusters. For hot DM which is relativistic at decoupling, the large structures would have been formed first while the small ones would have been obtained by fragmentation of these large structures. From N-body simulations this method is not compatible with the actual structure of the Universe. However, cold DM gives a satisfactory explanation of the structure formation [21]. Since a cold relic is non-relativistic at decoupling, the first structures created are the small ones which then combine together to create bigger structures. The largest N-body simulation so far, *the Millenium simulation* developed by Springel et al., supports this cosmological model including cold DM [22].

If we gather together all the cosmological constraints we got so far, the most convincing cosmological model of Big bang is a model where the Universe is isotropic, homogeneous, with a null spatial curvature and which contains both dark energy and

cold DM. This model called ΛCDM accounts for all the constraints mentioned in the previous sections. It contains six free parameters including the baryonic density Ω_b, the DM density $\Omega_{\rm DM}$ and the dark energy density Ω_Λ. The decoupling of cold DM from the thermal bath is described by the freeze-out mechanism and the inhomogeneities that DM creates in the early Universe lead to a structure formation in agreement with the galaxy structures we observe today.

1.4 Gravitational lensing

Gravity couples to all forms of energy including photons. Therefore, light is also bent by astrophysical bodies such as stars, galaxies and clusters of galaxies. An invisible object can then focus the light emitted from a distant body, as we can focus light using a lens in optics. The image we get can then exhibit some distortions. There are three types of gravitational lensing: strong lensing, weak lensing and microlensing [9].

Strong lensing shows a visible distortion that could also appear as Einstein rings. *Weak lensing* exhibits smaller distortions of the background objects and needs the shape of a large number of objects to be able to guarantee the existence of an invisible object on the line-of-sight. Finally, *microlensing* is the most subtle lensing effect. Indeed, no distortions appear from a telescope picture but the amount of light received from the background objects varies with time.

In the context of DM, gravitational lensing has been extensively used to find Massive Compact Halo Objects (MACHOs) *i.e.* small objects such as white and brown dwarfs. Such bodies emit a small amount of light and are invisible with a telescope. Even if MACHOs have been detected, they contribute to a few percent of the matter content of the Universe.

On the other hand, gravitational lensing combined to the detection of the X-ray gas in galaxy clusters lead to a smoking gun of DM. It has been observed that the intra-cluster gas emitting X-rays is in hydrodynamical equilibrium. It this then possible to access the baryonic mass distribution of a cluster by studying the density and the temperature of the intra-cluster hot gas. Then if two galaxy clusters collide, the X-ray gases are slowed down due to friction. However, the mass distribution of the two clusters can be probed by weak gravitational lensing. One example of such system is the *bullet cluster*. This system corresponds to the collision of a small cluster (the bullet) with a bigger cluster named 1E 0657-558. The results of X-ray gas measurements and weak gravitational lensing show that the mass distribution of the merged clusters is well separated from the mass distribution of baryonic matter. Unlike ordinary matter, it appears that most of the mass of the clusters have passed through each other without

Name		Family		
		$N = 1$	$N = 2$	$N = 3$
Fermions	Quarks	$\begin{pmatrix} u \\ d \end{pmatrix}$	$\begin{pmatrix} c \\ s \end{pmatrix}$	$\begin{pmatrix} t \\ b \end{pmatrix}$
	Leptons	$\begin{pmatrix} \nu_e \\ e^- \end{pmatrix}$	$\begin{pmatrix} \nu_\mu \\ \mu^- \end{pmatrix}$	$\begin{pmatrix} \nu_\tau \\ \tau^- \end{pmatrix}$
Bosons		γ, g, $W^\pm$, Z, H		

Table 1.1: Particle content of the SM.

interacting. This collisionless part of the cluster can be explained with non-baryonic DM and is another major point for the existence of DM.

1.5 The Standard Model of particle physics

Particles and interactions among them are described by the Standard Model (SM) of particle physics [23,24]. In this theory, an interaction is obtained by localizing a global symmetry under which the theory is invariant. This requires the introduction of new vector fields (mediators) in such a way that the new extended Lagrangian is invariant under the new symmetry. We call *gauge theory* a theory which invokes this procedure to introduce interaction terms in a Lagrangian.

Table 1.1 displays the particle content of the SM. The fermions, which comprise the matter particles, are particles carrying half-integer spin while bosons, which are mediators of the interactions, carry integer spin (spin-0 or spin-1). The fermions can be sub-divided into two groups: quarks and leptons. Quarks are the only constituents sensitive to the strong interaction but can not live as free states. Quarks are bound into hadrons themselves sub-divided into baryons and mesons whether they are formed from a combination of three quarks or a quark and an anti-quark, respectively. On the other side, leptons are only sensitive to electroweak interactions. The first generation of leptons consists of electrons and electron neutrinos. Actually quarks and leptons can be divided into three generations, each generation being a more massive copy of the previous one. Therefore, the quantum numbers associated are common to the three generations of fermions. Note that the first generation being the lightest one in mass, their members are all stable while it is not necessarily the case for the other two generations. For example muons and taus are not stable. Concerning quarks, up-type quarks (u, c, t) carry an electric charge $+2/3$ while down-type quarks (d, s, b) carry an electric charge $-1/3$. Concerning leptons, neutrinos are neutral while the others carry a negative unit of charge. Finally, the gauge bosons are involved as mediator

of the interactions. The massless photon γ is the mediator of electromagnetism, the massless gluons g are the mediators of the strong interaction and the massive $W^{\pm}$ and Z gauge bosons are mediators of weak interaction. The H boson is a scalar particle which gives a mass to the weak bosons and fermions as we will see later.

Now that we have introduced the particle content of the SM, we can develop through a simple example how interaction terms can be generated in a gauge theory as the SM. We focus on the simple case of quantum electrodynamics (QED). Let's consider the free Lagrangian of a massless electron field ψ_e

$$\mathcal{L}_e = \bar{\psi}_e i \not{\partial} \psi_e, \tag{1.40}$$

where $\bar{\psi}_e = \psi_e^{\dagger}\gamma^0$ and $\not{\partial} = \partial_\mu \gamma^\mu$ with γ^μ the Dirac matrices. This Lagrangian is invariant under global phase transformation $\psi_e(x) \to e^{iq\alpha}\psi_e(x)$ where α is a constant generator of transformation and q is the electric charge of the electron. However, if we turn the transformation to be local $\alpha \to \alpha(x)$, the Lagrangian is not invariant anymore unless we replace the partial derivative by a covariant derivative D_μ such that

$$\partial_\mu \to D_\mu = \partial_\mu - iqA_\mu. \tag{1.41}$$

The invariance is then restored if the new field A_μ, which can be identified as the photon, transforms as $A_\mu(x) \to A_\mu(x) + \partial_\mu \alpha(x)$. Promoting the field A_μ to a dynamical field, the initial Lagrangian finally writes

$$\mathcal{L}_e = \bar{\psi}_e i \not{D} \psi_e - \frac{1}{4} F_{\mu\nu} F^{\mu\nu}, \tag{1.42}$$

where $F_{\mu\nu} = \partial_\mu A_\nu - \partial_\nu A_\mu$ is the electromagnetic tensor. Clearly, imposing a $U(1)_{\mathrm{em}}$ local symmetry implies the existence of an interaction between electrons and photons. This procedure can also be applied for non-abelian groups even if their structures are more complicated.

The strong sector of the SM is called Quantum Chromodynamics (QCD) and is based on $SU(3)$ invariance. Quarks are triplet representations of $SU(3)$ and represented in column vectors

$$\begin{pmatrix} u_r \\ u_g \\ u_b \end{pmatrix}, \quad \begin{pmatrix} d_r \\ d_g \\ d_b \end{pmatrix}, \quad \begin{pmatrix} s_r \\ s_g \\ s_b \end{pmatrix}, \quad \begin{pmatrix} c_r \\ c_g \\ c_b \end{pmatrix}, \quad \begin{pmatrix} b_r \\ b_g \\ b_b \end{pmatrix}, \quad \begin{pmatrix} t_r \\ t_g \\ t_b \end{pmatrix}, \tag{1.43}$$

where the indices stand for the *colour* (red, green and blue). This denomination comes from the analogy with colour merging. Since quarks bound into hadrons, a combination of two coloured quark and anti-quark (mesons) or the combination of three coloured quarks (baryons) leads to a colourless state (white). $SU(3)$ is then called the

field	$SU(3)_c$	$SU(2)_L$	Y	Q	T_3
$L_L^i = \begin{pmatrix} \nu_{eL} \\ e_L \end{pmatrix}$	$\mathbf{1}$	$\mathbf{2}$	$\begin{pmatrix} -1 \\ -1 \end{pmatrix}$	$\begin{pmatrix} 0 \\ -1 \end{pmatrix}$	$\begin{pmatrix} +\frac{1}{2} \\ -\frac{1}{2} \end{pmatrix}$
l_R^i	$\mathbf{1}$	$\mathbf{1}$	-2	-1	0
$Q_L^i = \begin{pmatrix} u_L \\ d_L \end{pmatrix}$	$\mathbf{3}$	$\mathbf{2}$	$\begin{pmatrix} \frac{1}{3} \\ \frac{1}{3} \end{pmatrix}$	$\begin{pmatrix} \frac{2}{3} \\ -\frac{1}{3} \end{pmatrix}$	$\begin{pmatrix} +\frac{1}{2} \\ -\frac{1}{2} \end{pmatrix}$
u_R^i	$\mathbf{3}$	$\mathbf{1}$	$\frac{4}{3}$	$\frac{2}{3}$	0
d_R^i	$\mathbf{3}$	$\mathbf{1}$	$-\frac{2}{3}$	$-\frac{1}{3}$	0

Table 1.2: SM fields with their quantum numbers under $SU(3)_c \times SU(2)_L \times U(1)_Y$.

colour group and noted $SU(3)_c$. The eight generators of $SU(3)_c$ are the gluons G_μ^a with $a = 1, \cdots 8$ and the covariant derivative of each quark field Q is given by

$$D_\mu Q = (\partial_\mu - i g_s G_{\mu a} \lambda^a)\, Q, \tag{1.44}$$

where the λ^a matrices are the Gell-Mann matrices forming the algebra of $SU(3)_c$ and g_s is the strong interaction coupling which has a stronger value than the other interactions, justifying the *strong* adjective. The Lagrangian of QCD finally writes

$$\mathcal{L}_{QCD} = -\sum_{\text{quarks}} \bar{Q} \gamma_\mu D^\mu Q - \frac{1}{4} G_{\mu\nu a} G^{\mu\nu a}, \tag{1.45}$$

where $G_{\mu\nu a} \equiv \partial_\mu G_{\nu a} - \partial_\nu G_{\mu a} + i f^{bc}{}_a G_{\mu b} G_{\nu c}$ with $f^{bc}{}_a$ the structure constants of $SU(3)_c$.

The electroweak sector of the SM is invariant under $SU(2)_L \times U(1)_Y$. Actually the SM is a chiral theory meaning that it acts differently on left-handed and right-handed fermions. If we suppose a fermion field ψ, its left-handed and right-handed components are

$$\psi_L \equiv \left(\frac{1 - \gamma^5}{2} \right) \psi, \quad \psi_R \equiv \left(\frac{1 + \gamma^5}{2} \right) \psi, \tag{1.46}$$

where γ_5 is defined as

$$\gamma^5 = i \gamma^0 \gamma^1 \gamma^2 \gamma^3 = \begin{pmatrix} -1 & 0 \\ 0 & 1 \end{pmatrix}. \tag{1.47}$$

Additionally we can get the following relations

$$\bar{\psi}\psi = \bar{\psi}_L \psi_R + \bar{\psi}_R \psi_L, \quad \bar{\psi_L} \psi_L = \bar{\psi}_R \psi_R = 0, \tag{1.48}$$

which tell us that a particle with only one chiral component such as neutrinos can not have a mass term in the Lagrangian. Experimentally it was found that only left-handed

fermions couple to $W^{\pm}$ gauge bosons. Left-handed fermions are then represented as $SU(2)_L$ doublets

$$\begin{pmatrix}\nu_{eL}\\ e_L\end{pmatrix}, \quad \begin{pmatrix}\nu_{\mu L}\\ \mu_L\end{pmatrix}, \quad \begin{pmatrix}\nu_{\tau L}\\ \tau_L\end{pmatrix}, \quad \begin{pmatrix}u_L\\ d_L\end{pmatrix}, \quad \begin{pmatrix}c_L\\ s_L\end{pmatrix}, \quad \begin{pmatrix}t_L\\ b_L\end{pmatrix}, \tag{1.49}$$

while right-handed fermions are $SU(2)_L$ singlets

$$e_R, \quad \mu_R, \quad \tau_R, \quad u_R, \quad d_R, \quad c_R, \quad s_R, \quad t_R, \quad b_R. \tag{1.50}$$

We define the covariant derivative as

$$D_\mu \begin{pmatrix}\nu_{eL}\\ e_L\end{pmatrix} \equiv \left(\partial_\mu - i\frac{g}{2}\sigma^i W_{i\mu}\right)\begin{pmatrix}\nu_{eL}\\ e_L\end{pmatrix}, \tag{1.51}$$

where σ^i ($i = 1, 2, 3$) are the Pauli matrices , generators of $SU(2)_L$, since they satisfy the algebra

$$\left[\sigma^i, \sigma^j\right] = 2i\epsilon^{ij}{}_k\sigma^k. \tag{1.52}$$

The gauge bosons $W_{i\mu}$ are in the adjoint representation of $SU(2)_L$. The charged current is mediated by the W^+ and W^- gauge bosons which are rotated states from $W_{1\mu}$ and $W_{2\mu}$ fields,

$$W^{\pm}_\mu = \frac{1}{\sqrt{2}}\left(W_{1\mu} \mp W_{2\mu}\right). \tag{1.53}$$

However, the $W_{3\mu}$ gauge field can not be interpreted as the photon. Actually neutral current is allowed by weak interactions. Then in order to accommodate both weak and electromagnetic neutral currents we extend the $SU(2)_L$ structure to $SU(2)_L \times U(1)_Y$. This requires the electroweak Lagrangian to be locally invariant under $U(1)_Y$ gauge transformations and the covariant derivative acting on each field writes

$$D_\mu = \partial_\mu - ig'\frac{Y}{2}B_\mu, \tag{1.54}$$

where g' is the coupling constant associated to $U(1)_Y$ and Y is a quantum number called the weak hypercharge. The weak hypercharge is linked to the electric charge Q and the third component of the weak isospin $\mathbf{T}$ via the Gell-Mann-Nishijima relation

$$Q = T^3 + \frac{Y}{2}. \tag{1.55}$$

The summarised values of the quantum numbers as well as the representation of particle multiplets are displayed in Table 1.2. Finally the Lagrangian of the SM based on $SU(3)_c \times SU(2)_L \times U(1)_Y$ writes

$$\begin{aligned}\mathcal{L}_{SM} = &-\frac{1}{4}B^{\mu\nu}B_{\mu\nu} - \frac{1}{4}W_i^{\mu\nu}W^i_{\mu\nu} - \frac{1}{4}G^{\mu\nu}_a G^a_{\mu\nu}\\ &+ i\bar{Q}^j_L \not{D} Q^j_L + i\bar{u}^j_R \not{D} u^j_R + i\bar{d}^j_R \not{D} d^j_R\\ &+ i\bar{L}^j_L \not{D} L^j_L + i\bar{l}^j_R \not{D} l^j_R,\end{aligned} \tag{1.56}$$

where

$$D_\mu = \partial_\mu - ig_s G_{\mu a}\lambda^a - i\frac{g}{2}\sigma^i W_{i\mu} - ig'\frac{Y}{2}B_\mu \tag{1.57}$$

$$W^i_{\mu\nu} = \partial_\mu W^i_\nu - \partial_\nu W^i_\mu - g\epsilon^i_{jk}W^j_\mu W^k_\nu \tag{1.58}$$

$$B_{\mu\nu} = \partial_\mu B_\nu - \partial_\nu B_\mu. \tag{1.59}$$

While coherent, this theory misses a crucial point. Experimentally, the weak gauge bosons are actually massive but a gauge theory do not allow mass terms in the Lagrangian. Those ones are not gauge invariant. On top of that, fermions, which should be massive, are also massless in the theory of SM we just built. To allow both gauge bosons and fermions to acquire a mass we need to introduce a new scalar field called the Higgs field which will spontaneously break the symmetry $SU(2)_L \times U(1)_Y$. Only the unbroken electromagnetic gauge group $U(1)_{\rm em}$ with a massless photon will remain. This mechanism of spontaneously symmetry breaking is called the Brout-Englert-Higgs mechanism [25, 26] and led to a Nobel prize for the last two aforementioned physicists after the discovery of the H boson in July 2012 at the Large Hadron Collider at CERN [27, 28].

There are two ways to introduce mass terms for gauge bosons. The first one is to explicitly break the $SU(2)_L \times U(1)_Y$ symmetry by introducing mass terms for gauge bosons by hand in the SM Lagrangian. However, this approach would not preserve gauge invariance leading to a non-renormalizable theory and breaking unitarity. The second way to introduce mass terms for gauge bosons is spontaneous symmetry breaking. This kind of symmetry breaking preserves the gauge invariance of the original symmetry which is a crucial point for preserving also the renormalizability of the theory. Spontaneous symmetry breaking is based on the introduction of a complex scalar field ϕ, complex doublet of $SU(2)_L$, since it corresponds to the symmetry we want to break. We use the parametrisation

$$\phi = \begin{pmatrix}\phi^+ \\ \phi^0\end{pmatrix} = \frac{1}{2}\begin{pmatrix}\phi_1 + i\phi_2 \\ \phi_3 + i\phi_4\end{pmatrix}, \tag{1.60}$$

and we introduce a new term $\mathcal{L}_H$ in the SM Lagrangian

$$\mathcal{L}_H = \left(D_\mu\phi\right)^\dagger \left(D^\mu\phi\right) - V\left(\phi\right), \tag{1.61}$$

where

$$V\left(\phi\right) = \mu^2\phi^\dagger\phi + \lambda\left(\phi^\dagger\phi\right)^2 \tag{1.62}$$

is the scalar potential which is constrained by gauge invariance and renormalizability. If $\mu^2 > 0$, $V\left(\phi\right)$ has a minimum when $\phi = 0$. On the other hand, $\mu^2 < 0$ implies that $V\left(\phi\right)$ has an infinite number of degenerate minima given by

$$|\phi|^2 = -\frac{\mu^2}{2\lambda} \equiv \frac{1}{2}v^2. \tag{1.63}$$

All these minimum energy state configurations fulfilling this equation are connected by gauge transformations. The system spontaneously breaks $SU(2)_L \times U(1)_Y$ when it chooses one of these minima. We call v the vacuum expectation value (VEV). If we develop the electroweak Lagrangian around this new minimum energy state, it can be shown that new massless fields called Goldstone bosons appear, but they can be removed with a particular gauge choice called unitary gauge. However, the degrees of freedom associated to Goldstone bosons do not disappear, they have been absorbed by the gauge bosons, which acquire a physical longitudinal polarization making them massive. We say that Goldstone bosons have been eaten by gauge bosons. We can apply this mechanism directly to our field (1.60). If we choose the VEV in the direction of ϕ_3, $\phi_3 = v$ and $\phi_1 = \phi_2 = \phi_4 = 0$. Then we can re-parametrise the field ϕ perturbatively around the VEV,

$$\phi = \frac{1}{\sqrt{2}} \begin{pmatrix} 0 \\ v + H(x) \end{pmatrix}, \tag{1.64}$$

where $H(x)$ is a real scalar field. In this unitary gauge, the degrees of freedom associated to the Goldstone bosons $\phi_{1,2,4}$ have been absorbed by the gauge fields. To convince us , we insert the definition (1.64) of the field ϕ into the first term of Eq. (1.61) getting

$$\begin{aligned} \left(D_\mu \phi\right)^\dagger \left(D^\mu \phi\right) =& \frac{1}{2} \partial^\mu H \partial_\mu H \\ &+ \left[\frac{1}{4} g^2 W^{\mu +} W^-_\mu + \frac{1}{8} \left(g^2 + g'^2\right) Z^\mu Z_\mu \right] \left(H + v\right)^2, \end{aligned} \tag{1.65}$$

where we made the Z weak boson and A photon fields appear from a rotation of neutral W_3 and B neutral fields

$$\begin{pmatrix} Z_\mu \\ A_\mu \end{pmatrix} = \begin{pmatrix} \cos\left(\theta_w\right) & -\sin\left(\theta_w\right) \\ \sin\left(\theta_w\right) & \cos\left(\theta_w\right) \end{pmatrix} \begin{pmatrix} W_{3\mu} \\ B_\mu \end{pmatrix}. \tag{1.66}$$

The rotation angle is called the Weinberg angle and corresponds to

$$\cos\left(\theta_w\right) = \frac{g}{\sqrt{g^2 + g'^2}}. \tag{1.67}$$

Eq. (1.65) shows that the weak gauge bosons $W^\pm$ and Z have acquired a mass while there is no mass term for the photon confirming that $U(1)_{\mathrm{em}}$ is the unbroken symmetry. The $W^\pm$ and Z masses are given by

$$m_W = \frac{1}{2} g v \tag{1.68}$$

$$m_Z = \frac{1}{2} \sqrt{g^2 + g'^2} v. \tag{1.69}$$

With the new definiton of ϕ, the scalar potential (Eq. (1.62)) becomes

$$V(\phi) = \frac{1}{2}\left(2\lambda v^2\right) H^2 + \lambda v H^3 + \frac{1}{4}\lambda H^4. \tag{1.70}$$

We see that a scalar particle called the H boson appears and has a mass $m_H = \sqrt{2\lambda v^2}$.

We saw how spontaneous symmetry breaking of $SU(2)_L \times U(1)_Y$ to $U(1)_{\mathrm{em}}$ involving scalar field allows the weak gauge bosons to have a mass without spoiling the gauge invariance of the SM Lagrangian. Now we still need to introduce mass terms for fermions. The way to proceed is to introduce Yukawa interactions between fermions and the H boson since introducing mass terms for fermions by hand in the Lagrangian would not preserve the invariance in a chiral theory. The Yukawa interactions between fermions and the complex scalar field are given by

$$\mathcal{L}_Y = -Y^u_{ij}\bar{Q}^i_L \tilde{\phi}\, u^j_R - Y^d_{ij}\bar{Q}^i_L \phi\, d^j_R - Y^l_{ij}\bar{L}^i_L \phi\, l^j_R + h.c., \tag{1.71}$$

where $\tilde{\phi} = i\sigma^2\phi^*$. If we substitute ϕ with its expression (1.64), we get mass terms for fermions as well as interactions between fermions and the H boson. Additionally, the mass matrices for fermions are

$$m^l_{ij} = \frac{v}{\sqrt{2}}Y^l_{ij}, \quad m^u_{ij} = \frac{v}{\sqrt{2}}Y^u_{ij}, \quad m^d_{ij} = \frac{v}{\sqrt{2}}Y^d_{ij}. \tag{1.72}$$

To sum up, the SM is a chiral theory describing strong, weak and electromagnetic interactions. Based on the group structure $SU(3)_c \times SU(2)_L \times U(1)_Y$, the introduction of mass terms for weak gauge bosons involves a mechanism of spontaneous symmetry breaking (the Brout-Englert-Higgs mechanism); the $SU(2)_L \times U(1)_{\mathrm{em}}$ symmetry is spontaneously broken into $U(1)_{\mathrm{em}}$ thanks to the introduction of a $SU(2)$ doublet complex scalar field. Then fermion masses emerge via the interaction with the H boson. The SM is the most up-to-date model representing modern particle physics.

Even if SM has been extensively tested and validated, it contains some shortcomings. First, neutrinos are actually massive particles while they are massless for the SM. Then the validity of the SM above the TeV scale is compromised due to hierarchy and naturalness problems [29]. The SM is probably a low energy realisation of a more general model. More general models have been built by physicists and are often called *beyond Standard Model* theories (BSM).

1.6 Dark matter candidates

In the previous section we developed the most advanced validated model of modern particle physics. Now we want to know what could be a valid DM candidate. First

of all, does the SM contain valid DM candidates ? If not, which candidates in more advanced theories would fit ?

To present possible candidates for DM particle we need to address what would be the ideal candidate. Such candidate should be neutral otherwise electromagnetic interaction of DM would have been already discovered in the outer space. The candidate should also be stable (at least compared to the age of the Universe). Finally, if DM was produced thermally in the early Universe, its relic abundance should be smaller than (or equal to) the value recorded by Planck satellite.

Neutrinos Neutrinos are SM candidates that fulfil the mentioned criteria. Experiments studying oscillation of neutrino flavours set a lower bound on the neutrino mass for the heaviest neutrino $m_\nu > 0.05$ eV as well as an upper bound on the mass of each neutrino $m_\nu < 2.8$ eV. The computation of relic abundance can be evaluated to

$$\Omega_{\nu 0} h^2 = \sum_i g_i \left(\frac{m_{\nu i}}{90 \text{ eV}} \right), \tag{1.73}$$

where $g_i = 1$ or 2 if neutrinos are Majorana or Dirac particles, respectively. From the above constraints on neutrino masses and the constraints coming from CMB, primordial nucleosynthesis and structure formation, we get

$$0.0006 < \Omega_{\nu 0} h^2 < 0.0076, \tag{1.74}$$

which is well below the value of $\Omega_{\text{DM}} h^2$. According to this result, neutrinos alone can not constitute the whole density of DM in the Universe. On top of that, neutrinos are so light that they are falling into the hot DM relic category and we saw that hot DM is not a good candidate to explain the structure formation in the Universe.

However, some extensions of the SM predict the existence of *sterile neutrinos* that would be right-handed neutrinos coupling to the left-handed neutrinos of the SM. These sterile neutrinos would only interact gravitationally and then would be singlet under SM symmetries. Using a special mechanism called *see-saw* [30], the SM neutrinos acquire a very small mass while sterile neutrinos are much heavier and could satisfy the relic abundance constraint on DM.

Axions The combined action of charge conjugation C, parity P and time reversal T let the SM Lagrangian invariant (CPT theorem). However, CP symmetry is not an exact symmetry. CP is slightly violated by electroweak interaction as it was shown for the neutral kaon system. Then if we consider non-perturbative QCD, a large CP-violation was expected due to the following term in the effective QCD Lagrangian

$$\mathcal{L}_\theta \propto \theta g_s^2 G^a_{\mu\nu} \epsilon^{\mu\nu\rho\sigma} G_{a\rho\sigma}. \tag{1.75}$$

Such a term implies an electric dipole moment for the neutron which has never been observed experimentally ($\theta < 10^{-10}$). To solve this problem, Peccei and Quinn introduced a new $U(1)_{PQ}$ global symmetry which is spontaneously broken [31]. The pseudo-Goldstone boson resulting from this symmetry breaking is the axion. The θ parameter in Eq. (1.75) is then promoted to a field and the axion field a corresponds to $a = f_a\theta$ where f_a is the spontaneous symmetry breaking scale. The axion mass m_a only depends on f_a [32] and is given by

$$m_a = 0.57 \left(\frac{10^7 \text{ GeV}}{f_a}\right) \text{ eV}. \tag{1.76}$$

In the original model of Peccei and Quinn, the scale f_a was associated to the Higgs VEV, $f_a \simeq v$, but such a scale has been ruled out a long time ago. Today, laboratory and astrophysics (supernova 1987A) constraints have set an upper bound on axion mass, $m_a < 10^{-2}$ eV, suggesting $f_a \gg v$ [33]. Such an axion, called *invisible* axion, is then so light and so weakly interacting with ordinary matter that it can not be in thermal equilibrium in the early Universe. Then the axion does not follow the usual freeze-out mechanism and can be considered as a cold DM candidate despite its small mass. Note that models containing such an axion assume that the Peccei and Quinn symmetry is broken around the period of inflation, which is still an hypothetical era. Then the DM relic density constraint sets a lower bound on m_a, around 10^{-6} eV [32, 34]. This implies that the lower bound on m_a assumes the validity of General Relativity. Finally, the axion can couple to two photons and a couple of experiments have tried to use this interaction to get a hint of axion particle [35–37]. The current allowed mass range for axions is around $10^{-6} - 10^{-4}$ eV.

Weakly interacting massive particles A prime class of non-baryonic DM candidates corresponds to weakly interacting massive particles (WIMPs). We consider a Z_2 symmetry which will stabilize a DM candidate χ and allow annihilation and production of DM particles in pairs through the interaction $\bar{\chi}\chi \to \bar{f}f$, where f is an ordinary fermion. Using the freeze-out mechanism for non-relativistic species leads to a relic abundance $\Omega_\chi h^2$. If a DM particle would interact with the same strength as SM fermions interacting with regular electroweak gauge bosons, the freeze-out temperature x_F would be roughly $x_f = m_\chi/T_f \sim 20$. Being non-relativistic at decoupling, the relic density only depends on the velocity averaged cross section $\langle\sigma v\rangle$ as

$$\Omega_\chi h^2 \simeq 0.11 \times \frac{2.8 \times 10^{-26}\text{cm}^3\text{s}^{-1}}{\langle\sigma v\rangle}. \tag{1.77}$$

If we use a typical velocity averaged cross section of 1 pb corresponding for example to the cross section of a neutrino of several GeV interacting with a Z boson, we get

the right measured relic abundance of DM in the Universe. Aware of this appealing "coincidence", any DM candidate with a mass in the $\mathrm{GeV} - \mathrm{TeV}$ range interacting with weak gauge bosons or another interaction with similar strength can lead to the right relic abundance if we take also into account coannihilation processes that can affect the number of DM particles in the early Universe. This is the essence of what we call the WIMP miracle and every DM candidate fitting this requirement is called a WIMP. Such candidates arise in various BSM theories: the lightest supersymmetric particle (LSP) in supersymmetry (SUSY) (*e.g.* neutralino), the lightest Kaluza-Klein particle (LKP) in extra-dimension theories (*e.g.* KK-photon) and the lightest T-odd particle (LTP) in the little Higgs model. The appealing side of WIMPs comes also from the fact that the mass range concerned is reachable at colliders and other various astrophysical or ground-based experiments. In this thesis, we will mainly focus on WIMP searches.

Other candidates Another DM candidate is the gravitino which is the supersymmetric partner of the graviton in supergravity, *i.e.* the theory that combines SUSY and General Relativity. In phenomenologically viable SUSY models, SUSY breaking is often assumed to take place in a so-called hidden sector, and then transmitted to the visible sector (*i.e.* SM particles and their superpartners) through some mediation mechanism, *e.g.* gauge mediation and gravity mediation [38, 39]. The gravitino acquires a mass when SUSY breaks, by absorbing massless spin-$1/2$ goldstinos via a super-Higgs mechanism. The corresponding gravitino mass can be related to the SUSY breaking scale and the Planck scale. When the gravitino is the LSP, it can be considered as a possible DM candidate. Then the computation of the relic density for gravitinos leads to different conclusions in function of the gravitino mass [40]. Below a few eVs, the gravitino is not a viable candidate because the SUSY breaking scale is then too small to allow other supersymmetric particles above the TeV scale. Moreover, very light gravitinos would affect the expansion rate of the Universe and the light nuclear abundances. The gravitino can be heavier if we assume that it can decay during the cosmic evolution (with a very long lifetime), but this behaviour would affect the density of light nuclei after nucleosynthesis. Also for some other scenarios the relic density of gravitinos appears to be too high while it is still possible to find some windows than could be viable. Other DM candidates in SUSY such as sneutrinos and axinos have been explored. Other alternatives come from primordial black holes at the Planck scale. The list of DM candidates we invoked in this section is non-exhaustive but is a glimpse on the mass range that DM could cover, from axions to primordial black holes.

1.7 Dark matter detection

Nowadays the particle physics community puts a lot of energy and enthusiasm at detecting DM particle. Different paths are followed to search for DM in Earth-bound or satellite experiments and all of them rely on non-gravitational interaction with SM particles [41]. This strong assumption is motivated by the WIMP miracle.

1.7.1 Indirect detection

Indirect search of DM is based on the idea that DM density today is enhanced in galactic regions where there is a clump of gravitational matter such as the galactic centre or in the Sun. Then DM would annihilate into SM particles via

$$\chi\bar{\chi} \to \gamma\gamma, l^- l^+, q\bar{q}, \nu_l\bar{\nu}_l, W^+W^-, ZZ. \tag{1.78}$$

Indirect detection experiments record the deposit of energy of the products of DM annihilation using telescopes (both on the ground or in orbit around the Earth). The energy spectrum of the products could exhibit a hint of a possible DM particle. We can distinguish two types of products: charged particles and neutral ones. Charged particles require a special treatment because from the moment they were produced and the moment we detect them, they are deflected by magnetic fields present in the galactic halo and they also loose energy, inter alia, from synchrotron radiation and inverse Compton scattering. Some software modules like GALPROP [42] and DRAGON [43] allow to simulate the propagation of charged particles in the Galaxy. Another key point comes from particle anti-particle division. Indeed, the anti-particle content of the Universe is insignificant compared to the particle one. Therefore, the detection of anti-particles such as positrons and anti-protons with telescopes is a clearer way to detect DM particles. However, some bodies such as pulsars also emit e^+e^- and constitute an annoying background for indirect detection experiments.

We can take the production of two monochromatic photons from a direct annihilation process as an example. Such a signal appears as a mono-energetic line in the spectrum

$$\chi\bar{\chi} \to \gamma\gamma \qquad \text{with } E_\gamma \simeq m_\chi, \tag{1.79}$$

since we can consider DM particles at rest when annihilating. The gamma ray flux inside a solid angle $\Delta\Omega$ is given by

$$\frac{d\Phi_\gamma}{dE_\gamma} = \frac{\langle\sigma v\rangle}{8\pi m_\chi^2}\frac{dN_\gamma}{dE_\gamma}\int_{\Delta\Omega} d\Omega \int_{\text{line of sight}} dr\, \rho_\chi^2(l) \tag{1.80}$$

$$\equiv \frac{\langle\sigma v\rangle}{8\pi m_\chi^2}\frac{dN_\gamma}{dE_\gamma}\, J, \tag{1.81}$$

where dN_γ/dE_γ is the energy distribution of photons per reaction and $\rho_\chi(l)$ the DM density with l the distance between the observer and the annihilation event. To be able to compute this gamma ray flux we need a model of DM halo profile.

Nowadays three standard DM density profiles are usually used and differ from their behaviour in the DM core or at large distances [44]. The Navarro-Frenk-White (NFW) profile is given by

$$\rho_{\rm NFW}(r) = \frac{\rho_\odot}{\left(\frac{r}{R}\right)^\gamma \left(1+\frac{r}{R}\right)^{3-\gamma}}, \tag{1.82}$$

where r is the distance from centre of the Galaxy, $\rho_\odot$ is the DM density at the solar position and R is the characteristic radius of the halo. This profile containing a singularity in $r = 0$, it can not be applied to the centre of the Galaxy. Another profile is the Einasto profile given by

$$\rho_{\rm Einasto}(r) = \rho_\odot e^{\left[-\frac{2}{\alpha}\left(\left(\frac{r}{R}\right)^\alpha - 1\right)\right]}, \tag{1.83}$$

where the α parameter controls the curvature of the profile. The Einasto profile fits microlensing and star velocities better. However, observational data, showing a constant DM density from the centre of the Galaxy, are in contradiction with high-resolution numerical simulations which predict a much higher value at the centre. To prevent this behaviour, a third halo profile called the Burkert profile exhibits a constant density inside a radius R,

$$\rho_{\rm Burkert}(r) = \frac{\rho_\odot}{\left(1+\frac{r}{R}\right)\left(1+\frac{r^2}{R^2}\right)}. \tag{1.84}$$

Figure 1.5 shows the differences between these three density profiles for the Milky Way. The parameter values are taken from Ref. [45]. NFW and Einasto profiles are close from each other while the Burkert profile displays a smaller density of DM in the centre of the Galaxy. Now that we discussed the DM density in galactic halos, the gamma ray flux or any other fluxes can be computed with Eq. (1.81). On the experimental side, the Fermi-LAT collaboration recorded a gamma ray excess for $m_\chi \sim 130$ GeV that turned out to be a fake positive [46].

A couple of hints of DM popped out from indirect detection in other channels than $\gamma\gamma$, even if most of them have been ruled out or are waiting for a better understanding. The PAMELA satellite [47] and the Alpha Magnetic Spectrometer (AMS-02) [48] have both recorded a positron excess that has still to be confront to other sources of background. Then an excess of photons in the Galactic centre has been highlighted by analysing the Fermi-LAT data in this region [49, 50]. The excess covers an energy range $E_\gamma = 0.3 - 5$ GeV and does not consist of a gamma ray line. These photons could then come from radiation of DM annihilation products. Finally, the possible

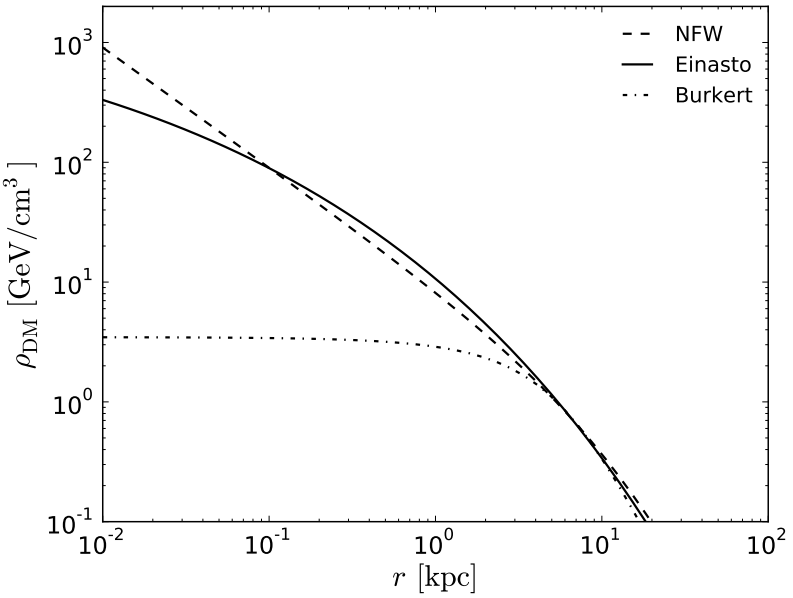


Figure 1.5: NFW, Einasto and Burkert Milky Way DM halo density profiles. See Ref. [45] for the mean values of the profile parameters.

neutrinos coming from annihilation of DM into the Sun could be detected by experiment such as IceCube [51] and Antares [52] which have no evidence of DM for the moment.

1.7.2 Direct detection

Direct detection experiments aim at detecting WIMPs by their scattering off nuclei. Using a nuclear target buried deep underground to protect against cosmic rays, they record the recoil of nuclei from the impact of an incoming WIMP passing through the Earth. The underlying techniques for this purpose are based on cryogenic and noble liquid detector technologies. Noble liquid detectors use the scintillation phenomenon produced in noble liquids such as Xenon and Argon to detect the recoil of nuclei while cryogenic detectors work at very-low temperature (mK scale) to detect the heat produced after a particle hits a nucleus. LUX [53], XENON100 [54], XENON1T [55] and LZ [56] are experiments based on Xenon detector while CDMS [57,58], CRESST [59], EDELWEISS [60] and EURECA [61] experiments use scintillators such as Germanium. These experiments involve low energy recoils since the typical recoil energy of nuclei is a few keVs. Then the lowest observable recoil that an experiment can reach

can be translated into a lower limit on the WIMP masses that they can probe. So far only limits have been set on the WIMP-nucleon cross section since no convincing evidence of DM emerged, the strongest one coming from LUX with an upper bound on spin independent WIMP-nucleon cross section of $1.1 \times 10^{-46}\ \mathrm{cm}^2$ for a WIMP mass of $50\ \mathrm{GeV}$. On the other hand, the controversial results of the DAMA experiment that recorded an annual modulation of DM signal compatible with theoretical predictions still need further investigations [62]. The detailed theory of direct detection will be covered in Chapter 3.

1.7.3 Production at colliders

Producing WIMPs in accelerator is also a way to discover or set constraints on DM. We will focus on the production of DM at the Large Hadron Collider (LHC) located at CERN which is a hadron collider using proton beams [63]. Since protons are heavier than leptons, it is easier to accelerate them to high energies due to less synchrotron radiation, but in the same time the resulting physics is more complicated. Additionally, hadron colliders are less annoyed by synchrotron radiation than lepton colliders. The background processes involving all the particles of the SM are described by QCD and the signal processes are typically rare compared to the background. In order to face the huge amount of events passing through the detectors, a trigger is necessary to only save and study interesting events *i.e.* events that would fit the signal. At the TeV scale, the constituents of the proton, quarks and gluons, are resolved and the proton kinematics is described by a parton density function (pdf) $f_i(x)$ which corresponds to a one-dimensional probability function depending on the fraction of the proton momentum x carried by a parton i. Using the parton densities, we can compute the cross section $\sigma_{pp\to X}$ of a hard proton-proton collision

$$\sigma_{pp\to X} = \sum_{i,j} \int dx_1 dx_2 f_{1,i}(x_1, \mu_F) f_{2,j}(x_2, \mu_F) \sigma_{i,j\to X}(x_1, x_2, \mu_F), \quad (1.85)$$

where the indices i and j run over all the initial partons that could produce the final state X and μ_F corresponds to the factorisation scale which is the typical energy scale of the process and also sets the separation between perturbative and non-perturbative dynamics.

The LHC is characterised by the centre-of-mass energy $\sqrt{s}$ of the collision and the luminosity L defined as

$$s = (p_1 + p_2)^2\,, \qquad L = f\frac{n_1 n_2}{4\pi\sigma_x\sigma_y}, \quad (1.86)$$

where $p_{1,2}$ denotes the 4-momentum of the protons, $n_{1,2}$ is the number of particles per bunch, f is the collision frequency and $\sigma_{x,y}$ corresponds to the beam size in the

two directions perpendicular to the beam pipe that we define as the z axis. Given a particular luminosity and a process characterised by a cross section $\sigma(s)$, the expected number of events N is given by

$$N = \mathcal{L} \times \sigma(s), \tag{1.87}$$

where $\mathcal{L} = \int dtL$ is the integrated luminosity. LHC Run I started in 2010 with a centre-of-mass energy $\sqrt(s) = 7\,\mathrm{TeV}$ and a maximal luminosity of $L = 3.7 \times 10^{33}\ \mathrm{cm}^{-2}\mathrm{s}^{-1}$ and continued in 2012 with a centre-of-mass energy $\sqrt{s} = 8\,\mathrm{TeV}$ and a maximal luminosity of $L = 7.7 \times 10^{33}\ \mathrm{cm}^{-2}\mathrm{s}^{-1}$. The LHC Run II at $\sqrt{s} = 13\,\mathrm{TeV}$ started in 2015. ATLAS [64], CMS [65], LHCb and ALICE are the four main experiments at the LHC. The first two are general purpose experiments while the last two are specialised experiments studying b physics and quark-gluon plasma, respectively. In 2012, ATLAS and CMS discovered the H boson, only missing piece of the SM.

Even if DM would let no trace in the ATLAS and CMS detectors, the principle of energy-momentum conservation may betray its presence. Since proton-proton collisions occur in the longitudinal direction, the total transverse momentum should be close to zero. Therefore, missing energy channels constitute a possible DM signal. The missing transverse energy $\not{E}_T$ (also noted as MET) is defined as

$$\not{E}_T = \left|\sum \vec{p}_{T,miss}\right| = \left|\sum \vec{p}_{T,vis}\right|, \tag{1.88}$$

where $\sum \vec{p}_{T,miss}$ corresponds to the sum of transverse momenta of invisible particles, which is the opposite vector of $\sum \vec{p}_{T,vis}$, the sum of transverse momenta of visible particles. Channels involving missing energy and constituting possible DM signals are

- jets plus missing energy or mono-jet(s) signatures where the jet comes from initial state radiation of light quarks,
- $t\bar{t}$ plus missing energy,
- mono-photon,
- mono-Z, mono-W or mono-H,
- mono-leptons,

if we assume that DM is produced in pairs due to the conservation of a new quantum number. The main background comes from neutrinos which produce the same signal as DM.

Because no DM signal has been recorded at LHC yet, the constraints set on different parameters coming from various BSM models have to be confronted to constraints coming from cosmology (relic density) and astrophysics (indirect and direct detection). The combination of all possible constraints would considerably reduce the phase space parameter. Since we have no clue on what DM is, a general approach consists in building models which make the less assumptions as possible on DM interactions. Simplified models enter into this class of models.

Chapter 2

Dark matter simplified models at LHC

"Seek simplicity, and distrust it."
Alfred N. Whitehead (1861 - 1947)

While the complementarity of different DM searches is a powerful tool, it is intrinsically limited in that the comparison of collider and other results introduces some degree of model dependence. As the nature of DM is still unknown, there exist a myriad of DM models and mechanisms to be explored, spanning a wide range of complexity and ambition. In this context, it is of utmost importance to follow an approach where the model dependence is limited, while the salient features that can provide a useful characterisation of possible signals are kept intact. The "simplified models" approach aims exactly at achieving this [66].

Many simplified models for DM have been proposed in the past (see Refs. [67–69] and references therein). In their simplest form, these models assume DM to be a single massive particle which interacts weakly with the SM particles *i.e.* a WIMP. The interaction of DM with the SM can be mediated by a new field, the mediator. When the mediator is heavier than the energy scales the experiment can probe, the interaction becomes point-like and the Lagrangian can be organised in terms of a tower of higher-dimensional operators in the framework of an effective field theory (EFT). However, when the experimentally accessible energy becomes comparable or higher than the mediator mass, on-shell effects become important and a properly defined quantum field theory featuring the mediator state in the spectrum is needed [70–75]. The LHC can explore a large range of DM and mediator masses, as well as coupling strengths

and possible combinations of DM and mediator spins. Collider results within the framework of simplified models can then be combined with direct searches for the mediators, $e.g.$ in Drell-Yan processes, as well as with cosmological and astrophysical constraints on DM (see Chapter 4).

Before proceeding to an overview of the goals of this chapter, we should step back and comment on the validity of the interpretation of DM LHC searches in terms of simplified models. Simplified model philosophy consists in describing UV-complete models without having to characterise the whole UV-completion. While this approach is not questionable for direct detection of DM since low characteristic transfer momenta already allow a description of the phenomenon in the EFT framework, it is of utmost importance to ensure that simplified models are also reliable at LHC where the energy scales involved are much bigger. Actually, it has been shown that even if unitarity can be broken using simplified models, the relevant couplings for such breaking appear to be greater than the valid range of perturbativity [76].

LHC searches for DM rely on precision calculations to impose the most stringent bounds on DM models, and hopefully characterise possible signals. Higher-order corrections in QCD to DM production processes at the LHC are hence vital for extracting precise information about DM from the LHC results.

The first goal of this chapter is to illustrate the feasibility of having a fully general implementation of DM simplified models in the FEYNRULES [77]/MADGRAPH5_AMC@NLO [78] (MG5_AMC) framework, accurate up to next-to-leading order (NLO) in QCD. To this aim we start with the simplest (yet non-trivial) case of s-channel mediators (colour singlet, spin 0 and 1 bosons) coupling to DM and quarks and we briefly comment on t-channel mediators. We assume that DM is a Dirac fermion for concreteness, yet our implementation is not limited by the choice of DM spin or nature (Dirac or Majorana). We show how predictions and event generation for this class of models can be achieved at NLO QCD accuracy, *in a fully automatic way*, for a wide set of observable/final states, while also employing the most recent matching/merging multi-jet techniques [79].

The second goal of this chapter is of phenomenological nature, $i.e.$ to investigate the impact of the NLO corrections on the current and future searches for DM at the LHC in the simplified model framework. Previous analyses [80–84] studied NLO QCD corrections for DM production in $\not{E}_T + j/\gamma/W$ in the case of EFT, $i.e.$, in the limit of heavy mediators. We consider two examples, among several promising final state signatures:

$$pp \to X\bar{X} + \text{jets} \tag{2.1}$$

for a spin-1 mediator model, and

$$pp \to X\bar{X} + t\bar{t} \tag{2.2}$$

for a spin-0 mediator model, where X is a DM particle. We do not only calculate NLO QCD corrections to the overall production rates, but also study in detail the effects of higher-order corrections on the differential distributions of relevant observables.

Our simulation set-up is based on the FEYNRULES/MG5_AMC framework. The FEYNRULES package provides the relevant Feynman rules starting from any local Lagrangian [77, 85, 86], as well as the UV/R_2 counterterms [87] necessary for the NLO computations via NLOCT [88]/FEYNARTS [89]. Our simplified DM model files are publicly available at the FEYNRULES repository [90]. With these ingredients, which are only based on the model and are not process dependent, MG5_AMC computes tree-level amplitudes, loop-amplitudes [91–93] and subtraction terms for a desired process, as well as their integration over phase space [94]. Event generation is obtained by matching short-distance events to the parton shower employing the MC@NLO method [95], which is implemented for PYTHIA6 [96], PYTHIA8 [97], HERWIG6 [98] and HERWIG++ [99].

This chapter is organised as follows. In Section 2.1 we introduce s-channel simplified models for DM and specify the relevant interactions and model parameters of the implementation. We discuss the impact of the NLO QCD corrections on DM pair production with jets through spin-1 mediators in Section 2.2, which includes a discussion of inclusive cross sections and differential distributions. NLO QCD predictions for DM production in association with a top-quark pair through spin-0 mediators are discussed in Section 2.3. We provide our conclusions and t-channel simplified models prospects in Section 2.4.

2.1 The s-channel mediator case

We start by defining the particle content and the interactions of the simplified model, which we dub DMSIMP. We assume that DM is described by a single, massive and weakly interacting particle, that communicates to the SM through the exchange of a mediator. For simplicity, we assume that the mediator is not part of the SM.[1] In addition, we consider pair production of DM, imposing the DM candidate to be charged under a Z_2 symmetry. The mediator is not charged under this new symmetry. The first very general classification stems from the class of vertices that characterise the

[1] So-called portal models where DM interacts with the Higgs or the Z/γ bosons can be included in our framework as well.

model: Lagrangians featuring DM-DM-mediator and SM-SM-mediator type interactions identify models with an s-channel mediator, while Lagrangians characterised by DM-SM-mediator interactions define a t-channel mediator. From the point of view of QCD corrections the two classes are very different, as an s-channel mediator is necessarily a colour singlet, while a t-channel mediator can be either neutral or coloured. To start with, we focus on the case of Dirac DM with spin-1 or spin-0 mediators coupling to the matter fields of the SM. Changing the spin or the nature of the fermion (Dirac or Majorana) of the DM particle or including a coupling of the mediator to the SM bosons is straightforward [100].

2.1.1 Spin-1 mediator model

In the framework of our simplified model, the interaction Lagrangian of a spin-1 mediator (Y_1) with a Dirac fermion DM (X_D) is given by

$$\mathcal{L}_{X_D}^{Y_1} = \bar{X}_D \gamma_\mu (g_{X_D}^V + g_{X_D}^A \gamma_5) X_D \, Y_1^\mu \,, \tag{2.3}$$

and with quarks by

$$\begin{aligned} \mathcal{L}_{\rm SM}^{Y_1} = \sum_{i,j} \Big[& \bar{d}_i \gamma_\mu (g_{d_{ij}}^V + g_{d_{ij}}^A \gamma_5) d_j \\ & + \bar{u}_i \gamma_\mu (g_{u_{ij}}^V + g_{u_{ij}}^A \gamma_5) u_j \Big] Y_1^\mu \,, \end{aligned} \tag{2.4}$$

where d and u denote down- and up-type quarks, respectively, (i, j=1,2,3) are flavour indices, and $g^{V/A}$ are the vector/axial-vector couplings of DM and quarks. Note that we adopt this notation according to the actual implementation in FEYNRULES. The model file also includes an alternative choice for the spin of DM particle (complex scalar X_C).

The pure vector and pure axial-vector mediator scenarios are given by setting the parameters in the Lagrangians (2.3) and (2.4) to

$$g_{X_D}^V \equiv g_X \quad \text{and} \quad g_{X_D}^A = 0 \tag{2.5}$$

$$g_{u_{ii}}^V = g_{d_{ii}}^V \equiv g_{\rm SM} \quad \text{and} \quad g_{u_{ii}}^A = g_{d_{ii}}^A = 0 \tag{2.6}$$

and

$$g_{X_D}^V = 0 \quad \text{and} \quad g_{X_D}^A \equiv g_X \tag{2.7}$$

$$g_{u_{ii}}^V = g_{d_{ii}}^V = 0 \quad \text{and} \quad g_{u_{ii}}^A = g_{d_{ii}}^A \equiv g_{\rm SM} \,, \tag{2.8}$$

respectively, where we assume quark couplings to the mediator to be flavour universal and set all flavour off-diagonal couplings to zero. With this simplification of a single

universal coupling for the SM-Y_1 interactions, the model has only four independent parameters, $i.e.$ two couplings and two masses:

$$\{g_{\rm SM},\, g_X,\, m_X,\, m_Y\}\,. \tag{2.9}$$

We note that the mediator width is calculated from the above parameters.

Finding a signal of DM in this parameter space (or to constrain these parameters) is the primary goal of the DM searches at the LHC Run II [69], and the most important signature in this model is mono-jet plus $\not{E}_T$. The di-jet final state via the Y_1 Drell-Yan process can be an important complementary channel.

2.1.2 Spin-0 mediator model

Similarly, in the case of a spin-0 mediator (Y_0) interacting with the Dirac fermion DM and the SM particles, we define the interaction part of the Lagrangians as

$$\mathcal{L}^{Y_0}_{X_D} = \bar{X}_D(g^S_{X_D} + ig^P_{X_D}\gamma_5)X_D\, Y_0\,, \tag{2.10}$$

and

$$\begin{aligned}\mathcal{L}^{Y_0}_{\rm SM} = \sum_{i,j}\Big[&\bar{d}_i\frac{y^d_{ij}}{\sqrt{2}}(g^S_{d_{ij}} + ig^P_{d_{ij}}\gamma_5)d_j \\ &+ \bar{u}_i\frac{y^u_{ij}}{\sqrt{2}}(g^S_{u_{ij}} + ig^P_{u_{ij}}\gamma_5)u_j\Big]Y_0\,,\end{aligned} \tag{2.11}$$

where $g^{S/P}$ are the scalar/pseudo-scalar couplings of DM and quarks. Assuming a UV complete description of the scalar theory with the couplings of the mediator to the SM particles proportional to the particle masses, we normalise these couplings to the SM Yukawa couplings, $y^f_{ii} = \sqrt{2}m_f/v$, and set all flavour off-diagonal couplings to zero. This implies that, in a five-flavour scheme with massless bottom quarks, only top quarks are relevant for DM production in this model. Extension to a four-flavour scheme with massive bottom quarks is possible. The model file for the spin-0 mediator case includes other choices for the spin of the DM particle (real scalar X_R and complex scalar X_C).

The pure scalar and pure pseudo-scalar mediator scenarios are given by setting the parameters in the Lagrangians (2.10) and (2.11) to

$$g^S_{X_D} \equiv g_X \quad \text{and} \quad g^P_{X_D} = 0 \tag{2.12}$$

$$g^S_{u_{33}} \equiv g_{\rm SM} \quad \text{and} \quad g^P_{u_{33}} = 0 \tag{2.13}$$

and

$$g^S_{X_D} = 0 \quad \text{and} \quad g^P_{X_D} \equiv g_X \tag{2.14}$$
$$g^S_{u_{33}} = 0 \quad \text{and} \quad g^P_{u_{33}} \equiv g_{\rm SM}\,, \tag{2.15}$$

respectively. All the other $g^{S/P}_{u_{ij}}$ and $g^{S/P}_{d_{ij}}$ parameters are irrelevant. Similar to the spin-1 case, the model has only four independent parameters as in (2.9).

In the spin-0 mediator model with Yukawa-type couplings, the most relevant tree-level process at the LHC is DM pair production associated with a top-quark pair. On the other hand similarly to Higgs production, at one loop, gluon fusion can give rise to $\not{E}_T$ + jets signatures which are in general phenomenologically relevant. For the heavy mediator case, the four-top final state can be also relevant.

At this stage, we do not see compelling reasons to introduce couplings of the mediator to leptons, even though it is straightforward to do. We do not include effective gluon-gluon-Y_0 interactions either, for several reasons. The first is that this operator is higher dimensional (dim=5) and therefore might lead to unitarity-violating effects that need to be studied on a model and benchmark basis. The second is that a simplified model assumes no other new physics particle beyond the DM particle X and mediator Y at the weak scale. If such new particle effects decouple with their mass, the main contribution to the gluon-gluon-Y_0 coupling would then be due to loop of SM quarks. Depending on the masses involved (that of the DM, the mediator and the quarks contributing in the loop) and the momentum transfer of the process, such interactions might be considered point-like. This is, however, very much model and process dependent. To be accurate one should first calculate the loop-induced processes exactly and study the range of applicability of such an effective interaction by explicit comparison. This is possible in MG5_aMC [101] and has been considered with the same DM implementation as presented here in Ref. [102]. Other studies of the loop-induced process for mono-jet + $\not{E}_T$ can be found in Refs. [103–106]. We also note that couplings of the mediator to the SM gauge bosons can be introduced easily [100].

2.2 Dark matter production in association with jets

In this section, we consider a spin-1 mediator scenario and discuss the impact of the NLO QCD corrections on DM pair production with jets, $i.e.$,

$$pp \to X\bar{X} + j(j)\,. \tag{2.16}$$

In MG5_AMC the code and events for the above process can be automatically generated by issuing the following commands:

```
> import model DMsimp_s_spin1
> generate p p > xd xd~ j [QCD]
> add process p p > xd xd~ j j [QCD]
> output
> launch
```

We have checked that our model can reproduce the SM predictions for $pp \to Zj(j) \to \tau^+\tau^- j(j)$ by adjusting the corresponding coupling and mass parameters.

In order to illustrate the effect of the higher-order corrections, we consider pure vector, Eqs. (2.5) and (2.6), or pure axial-vector, Eqs. (2.7) and (2.8), couplings with a simplified flavour structure. We take

$$g_X = 1 \quad \text{and} \quad g_{\rm SM} = 0.25 \tag{2.17}$$

as our benchmark for the spin-1 mediator scenario.

We assume that the mediator can only decay into the DM particle and the SM quarks (if kinematically allowed) through the interactions specified in Eqs. (2.3) and (2.4), so that the mediator width, Γ_Y, is determined by the particle masses and the couplings g_X and $g_{\rm SM}$. In our framework, the width is automatically computed by using the MADWIDTH module [107] for each parameter point. The above benchmark coupling strength in (2.17) leads to $\Gamma_Y/m_Y \sim 0.05$ for $m_Y > 2m_X$ and $\Gamma_Y/m_Y \sim 0.025$ for $m_Y < 2m_X$, both for the vector and axial-vector cases. Note that, if we take $g_{\rm SM} = 1\,(0.5)$ with $g_X = 1$, the Y_1 width becomes very large as $\Gamma_Y/m_Y \sim 0.5\,(0.15)$ for $m_Y > 2m_X$.

We provide LO and NLO QCD predictions for $pp \to X\bar{X} + j(j)$ at the centre-of-mass energy $\sqrt{s} = 13$ TeV. The central value μ_0 for the renormalisation (μ_R) and factorisation (μ_F) scales is set to $H_T/2$, where H_T is the sum of the transverse momenta of all jets in the event and the missing transverse energy. The scale uncertainty is estimated by varying the scales μ_R and μ_F, independently, by a factor two around μ_0. We adopt the five-flavour scheme and the LO NNPDF2.1 and NLO NNPDF2.3 sets [108] through the LHAPDF interface [109], with the corresponding values of $\alpha_s^{\rm LO}(M_Z) = 0.130$ and $\alpha_s^{\rm NLO}(M_Z) = 0.118$, for the LO and NLO predictions, respectively. The PDF uncertainties are computed automatically [110], following the prescription summarised in [111].

Where relevant, we apply a parton shower to the events using PYTHIA8 [97]. We then define jets using the anti-k_T algorithm [112] as implemented in FASTJET [113] with

(m_Y, m_X) [GeV]			vector		
			$\not{E}_T > 150$ GeV	$\not{E}_T > 300$ GeV	$\not{E}_T > 500$ GeV
10	undecayed	$\sigma_{\rm LO}$ [pb]	$2.923 \times 10^{2}\,^{+10.7}_{-8.9}\,\pm 1.6\,\%$	$1.734 \times 10^{1}\,^{+14.2}_{-11.9}\,\pm 1.1\,\%$	$1.695 \times 10^{0}\,^{+17.4}_{-14.0}\,\pm 1.8\,\%$
		$\sigma_{\rm NLO}$ [pb]	$5.093 \times 10^{2}\,^{+10.3}_{-8.2}\,\pm 0.5\,\%$	$2.689 \times 10^{1}\,^{+10.4}_{-9.1}\,\pm 0.6\,\%$	$2.433 \times 10^{0}\,^{+11.1}_{-10.0}\,\pm 1.1\,\%$
		K factor	1.74	1.55	1.44
$(10, 1)$	$m_Y > 2m_X$	$\sigma_{\rm LO}$ [pb]	$1.605 \times 10^{2}\,^{+10.7}_{-8.9}\,\pm 1.6\,\%$	$0.978 \times 10^{1}\,^{+14.3}_{-12.0}\,\pm 1.1\,\%$	$0.970 \times 10^{0}\,^{+17.4}_{-14.1}\,\pm 2.0\,\%$
		$\sigma_{\rm NLO}$ [pb]	$2.818 \times 10^{2}\,^{+10.1}_{-8.1}\,\pm 0.5\,\%$	$1.517 \times 10^{1}\,^{+10.0}_{-8.9}\,\pm 0.6\,\%$	$1.345 \times 10^{0}\,^{+10.5}_{-9.6}\,\pm 1.1\,\%$
		K factor	1.76	1.55	1.39
$(10, 50)$	$m_Y < 2m_X$	$\sigma_{\rm LO}$ [pb]	$2.434 \times 10^{0}\,^{+11.8}_{-10.1}\,\pm 1.5\,\%$	$2.843 \times 10^{-1}\,^{+15.0}_{-12.5}\,\pm 1.2\,\%$	$3.786 \times 10^{-2}\,^{+18.0}_{-14.5}\,\pm 2.4\,\%$
		$\sigma_{\rm NLO}$ [pb]	$3.198 \times 10^{0}\,^{+5.6}_{-5.4}\,\pm 0.5\,\%$	$3.485 \times 10^{-1}\,^{+5.9}_{-6.3}\,\pm 0.7\,\%$	$4.325 \times 10^{-2}\,^{+7.3}_{-7.8}\,\pm 1.3\,\%$
		K factor	1.31	1.23	1.14
$(10, 500)$	$m_Y < 2m_X$	$\sigma_{\rm LO}$ [pb]	$6.968 \times 10^{-3}\,^{+17.4}_{-14.0}\,\pm 4.3\,\%$	$2.314 \times 10^{-3}\,^{+18.9}_{-15.0}\,\pm 4.6\,\%$	$7.317 \times 10^{-4}\,^{+20.6}_{-16.1}\,\pm 5.6\,\%$
		$\sigma_{\rm NLO}$ [pb]	$7.698 \times 10^{-3}\,^{+5.4}_{-6.4}\,\pm 2.2\,\%$	$2.385 \times 10^{-3}\,^{+5.7}_{-6.9}\,\pm 2.3\,\%$	$6.800 \times 10^{-4}\,^{+5.5}_{-7.1}\,\pm 2.6\,\%$
		K factor	1.10	1.03	0.93
100	undecayed	$\sigma_{\rm LO}$ [pb]	$2.148 \times 10^{2}\,^{+10.6}_{-9.3}\,\pm 1.5\,\%$	$1.616 \times 10^{1}\,^{+14.4}_{-12.0}\,\pm 1.0\,\%$	$1.644 \times 10^{0}\,^{+17.4}_{-14.1}\,\pm 1.9\,\%$
		$\sigma_{\rm NLO}$ [pb]	$3.011 \times 10^{2}\,^{+6.6}_{-5.9}\,\pm 0.5\,\%$	$2.121 \times 10^{1}\,^{+7.3}_{-7.1}\,\pm 0.6\,\%$	$1.955 \times 10^{0}\,^{+8.1}_{-8.2}\,\pm 1.2\,\%$
		K factor	1.40	1.31	1.19
$(100, 1)$	$m_Y > 2m_X$	$\sigma_{\rm LO}$ [pb]	$1.100 \times 10^{2}\,^{+10.6}_{-9.3}\,\pm 1.5\,\%$	$0.822 \times 10^{1}\,^{+14.4}_{-12.0}\,\pm 1.1\,\%$	$0.862 \times 10^{0}\,^{+17.4}_{-14.1}\,\pm 1.9\,\%$
		$\sigma_{\rm NLO}$ [pb]	$1.530 \times 10^{2}\,^{+6.5}_{-5.7}\,\pm 0.5\,\%$	$1.100 \times 10^{1}\,^{+7.4}_{-7.2}\,\pm 0.6\,\%$	$1.059 \times 10^{0}\,^{+8.0}_{-8.1}\,\pm 1.2\,\%$
		K factor	1.39	1.34	1.23
$(95, 50)$	$m_Y \lesssim 2m_X$	$\sigma_{\rm LO}$ [pb]	$1.117 \times 10^{1}\,^{+11.0}_{-9.6}\,\pm 1.5\,\%$	$0.988 \times 10^{0}\,^{+14.7}_{-12.2}\,\pm 1.1\,\%$	$1.140 \times 10^{-1}\,^{+17.6}_{-14.2}\,\pm 2.0\,\%$
		$\sigma_{\rm NLO}$ [pb]	$1.512 \times 10^{1}\,^{+6.0}_{-5.5}\,\pm 0.5\,\%$	$1.281 \times 10^{0}\,^{+6.8}_{-6.8}\,\pm 0.6\,\%$	$1.325 \times 10^{-1}\,^{+7.2}_{-7.6}\,\pm 1.2\,\%$
		K factor	1.35	1.30	1.16
$(100, 500)$	$m_Y < 2m_X$	$\sigma_{\rm LO}$ [pb]	$7.043 \times 10^{-3}\,^{+17.4}_{-14.0}\,\pm 4.3\,\%$	$2.329 \times 10^{-3}\,^{+18.9}_{-15.0}\,\pm 4.6\,\%$	$7.395 \times 10^{-4}\,^{+20.6}_{-16.1}\,\pm 5.6\,\%$
		$\sigma_{\rm NLO}$ [pb]	$7.804 \times 10^{-3}\,^{+5.3}_{-6.4}\,\pm 2.2\,\%$	$2.411 \times 10^{-3}\,^{+5.5}_{-6.8}\,\pm 2.3\,\%$	$6.908 \times 10^{-4}\,^{+5.5}_{-7.1}\,\pm 2.6\,\%$
		K factor	1.11	1.04	0.93
1000	undecayed	$\sigma_{\rm LO}$ [pb]	$2.248 \times 10^{0}\,^{+16.1}_{-13.2}\,\pm 3.2\,\%$	$6.865 \times 10^{-1}\,^{+17.7}_{-14.3}\,\pm 3.3\,\%$	$1.979 \times 10^{-1}\,^{+19.6}_{-15.5}\,\pm 4.1\,\%$
		$\sigma_{\rm NLO}$ [pb]	$2.601 \times 10^{0}\,^{+5.1}_{-6.0}\,\pm 1.7\,\%$	$7.393 \times 10^{-1}\,^{+5.2}_{-6.4}\,\pm 1.8\,\%$	$1.909 \times 10^{-1}\,^{+5.3}_{-6.8}\,\pm 2.1\,\%$
		K factor	1.16	1.08	0.96
$(1000, 1)$	$m_Y > 2m_X$	$\sigma_{\rm LO}$ [pb]	$1.093 \times 10^{0}\,^{+16.4}_{-13.3}\,\pm 3.1\,\%$	$3.278 \times 10^{-1}\,^{+18.0}_{-14.4}\,\pm 3.3\,\%$	$9.182 \times 10^{-2}\,^{+19.7}_{-15.6}\,\pm 4.1\,\%$
		$\sigma_{\rm NLO}$ [pb]	$1.215 \times 10^{0}\,^{+4.2}_{-5.5}\,\pm 1.7\,\%$	$3.399 \times 10^{-1}\,^{+4.5}_{-6.0}\,\pm 1.7\,\%$	$8.743 \times 10^{-2}\,^{+4.8}_{-6.5}\,\pm 2.0\,\%$
		K factor	1.11	1.04	0.95
$(1000, 50)$	$m_Y > 2m_X$	$\sigma_{\rm LO}$ [pb]	$1.094 \times 10^{0}\,^{+16.4}_{-13.3}\,\pm 3.1\,\%$	$3.268 \times 10^{-1}\,^{+18.0}_{-14.4}\,\pm 3.3\,\%$	$9.137 \times 10^{-2}\,^{+19.7}_{-15.6}\,\pm 4.1\,\%$
		$\sigma_{\rm NLO}$ [pb]	$1.221 \times 10^{0}\,^{+4.3}_{-5.6}\,\pm 1.7\,\%$	$3.416 \times 10^{-1}\,^{+4.6}_{-6.0}\,\pm 1.7\,\%$	$8.807 \times 10^{-2}\,^{+4.9}_{-6.6}\,\pm 2.0\,\%$
		K factor	1.12	1.05	0.96
$(995, 500)$	$m_Y \lesssim 2m_X$	$\sigma_{\rm LO}$ [pb]	$2.169 \times 10^{-1}\,^{+16.4}_{-13.3}\,\pm 3.4\,\%$	$6.777 \times 10^{-2}\,^{+18.0}_{-14.4}\,\pm 3.6\,\%$	$1.981 \times 10^{-2}\,^{+19.7}_{-15.6}\,\pm 4.4\,\%$
		$\sigma_{\rm NLO}$ [pb]	$2.497 \times 10^{-1}\,^{+5.3}_{-6.2}\,\pm 1.8\,\%$	$7.223 \times 10^{-2}\,^{+5.5}_{-6.6}\,\pm 1.9\,\%$	$1.914 \times 10^{-2}\,^{+5.3}_{-6.8}\,\pm 2.1\,\%$
		K factor	1.15	1.07	0.97
$(10000, 1)$	$m_Y \gg \sqrt{\hat{s}}$	$\sigma_{\rm LO}$ [pb]	$8.487 \times 10^{-6}\,^{+18.0}_{-14.3}\,\pm 4.3\,\%$	$2.666 \times 10^{-6}\,^{+20.0}_{-15.7}\,\pm 5.5\,\%$	$8.238 \times 10^{-7}\,^{+22.0}_{-17.0}\,\pm 7.3\,\%$
		$\sigma_{\rm NLO}$ [pb]	$8.835 \times 10^{-6}\,^{+3.1}_{-5.1}\,\pm 2.5\,\%$	$2.579 \times 10^{-6}\,^{+3.1}_{-5.5}\,\pm 3\,\%$	$7.148 \times 10^{-7}\,^{+5.0}_{-7.0}\,\pm 4.4\,\%$
		K factor	1.04	0.97	0.87

Table 2.1: LO and NLO cross sections and corresponding K factors for DM pair production in association with a jet for the vector mediator scenario at the 13-TeV LHC, where different $\not{E}_T$ cuts are imposed. The uncertainties represent the scale and PDF uncertainties in percent, respectively. We show several benchmark model points for the mediator and DM masses with the coupling parameters $g_X = 1$ and $g_{\rm SM} = 0.25$.

the jet cone radius $R = 0.4$, where we require $p_T(j) > 30$ GeV and $|\eta(j)| < 4.5$ for all jets in the event.

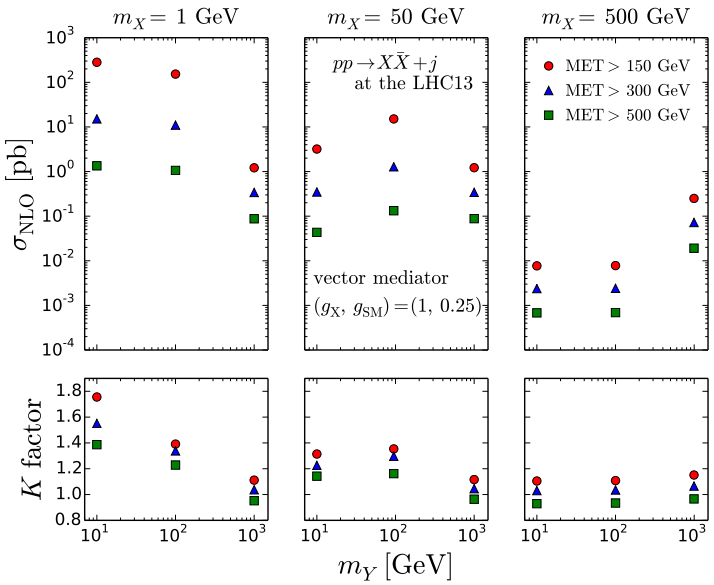


Figure 2.1: Summary plot of NLO cross sections and corresponding K factors in Table 2.1.

2.2.1 Total cross sections

In Table 2.1 we present LO and NLO cross sections (in pb) for DM pair production in association with a jet at fixed order (FO) in perturbation theory. We show results for a pure vector mediator by fixing the parameters as in Eqs. (2.5), (2.6) and (2.17). We cover various benchmark points suggested by the ATLAS/CMS DM forum [69] in the $m_Y - m_X$ plane, representing four different cases: on-shell ($m_Y > 2m_X$) and off-shell ($m_Y < 2m_X$) production of the mediator, in the threshold regime ($m_Y \lesssim 2m_X$) and in the EFT limit ($m_Y \gg \sqrt{\hat{s}}$). We also present scale and PDF uncertainties in % as well as K factors which we define as the ratio of the central values of the NLO and LO cross sections. We compute the table entries with different $\not{E}_T$ cuts: 150, 300, and 500 GeV. For convenience, we also show a graphical summary of our results in Fig. 2.1. As a reference, the cross sections for $pp \to Y_1 + j$ are also shown, where the vector mediator Y_1 is produced on-shell and does not decay. For $m_Y > 2m_X$, the mono-jet rate is given by $\sigma(pp \to X\bar{X} + j) \sim \sigma(pp \to Y_1 + j) \times B(Y_1 \to X\bar{X})$ in the narrow width approximation.

The production rate strongly depends on both masses as well as on the kinematic cuts, and varies by orders of magnitude in the parameter scan. On the other hand, the K

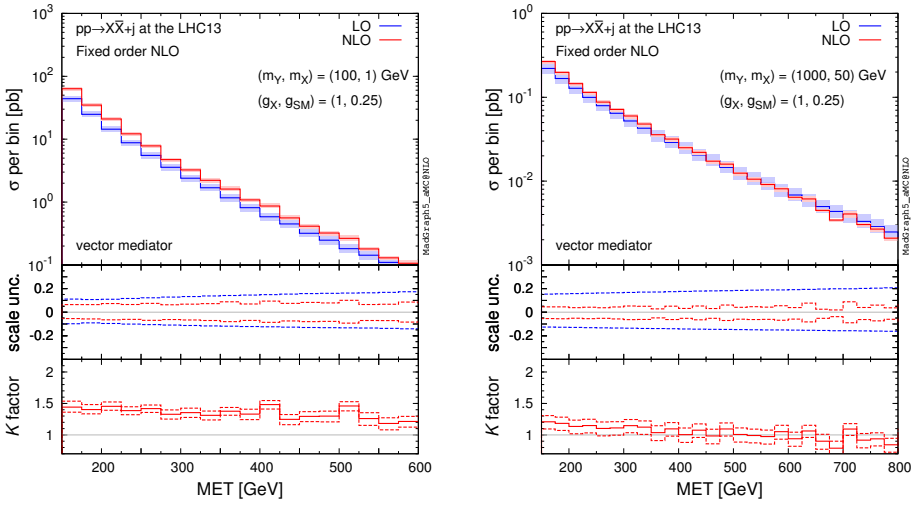


Figure 2.2: $\not{E}_T$ distributions at FO (N)LO accuracy for $pp \to X\bar{X} + j$ at the 13-TeV LHC for $(m_Y, m_X) = (100, 1)$ and $(1000, 50)$ GeV, where we assume a pure vector mediator and Dirac DM. The middle and bottom panels show the differential scale uncertainties and K factors, respectively.

factors, *i.e.* higher-order effects, are not so sensitive to the mass spectra; $K \sim 1.1$ for the heavy-mediator and/or heavy-DM cases, while $K \sim 1.3 - 1.4$ for the ~ 100 GeV mediator with light DM, assuming the $\not{E}_T > 150$ GeV cut. We find that in the case of a relatively light mediator with a very light DM, $(m_Y, m_X) = (10, 1)$ GeV, the K factor can reach a value as large as 1.8.

Different benchmark points probe different Bjorken-x regions of the parton distribution functions. As heavy mediators/DM are produced from very high-x partons, the dominant contribution comes from the $q\bar{q}$ initial state, as the gluon PDF is subdominant in the high-x region. For light mediators with light DM, on the other hand, a large contribution arises from the qg initial state. For instance, we find that the ratio of production cross sections via $u\bar{u}$ and ug initial states, $\sigma(u\bar{u})/\sigma(ug)$, is 1.4 in the case of $(m_Y, m_X) = (1000, 50)$ GeV while 0.2 for $(m_Y, m_X) = (100, 1)$ GeV, at LO.

As expected, most of the results at NLO accuracy display significantly smaller scale uncertainties compared to the LO calculations. An exception is provided by the $(m_Y, m_X) = (10, 1)$ GeV case, which we discuss in detail at the end of this subsection. The PDF uncertainties are sub-leading in both the LO and NLO results and reduced by going from LO to NLO. Furthermore, the scale and PDF uncertainties in-

(m_Y, m_X) [GeV]			axial-vector		
			$\not{E}_T > 150$ GeV	$\not{E}_T > 300$ GeV	$\not{E}_T > 500$ GeV
100	undecayed	$\sigma_{\rm LO}$ [pb]	$2.130 \times 10^{2}\,^{+10.6}_{-9.3}\,\pm 1.6\,\%$	$1.573 \times 10^{1}\,^{+14.4}_{-12.0}\,\pm 1.1\,\%$	$1.633 \times 10^{0}\,^{+17.3}_{-14.0}\,\pm 1.9\,\%$
		$\sigma_{\rm NLO}$ [pb]	$3.063 \times 10^{2}\,^{+6.9}_{-6.1}\,\pm 0.5\,\%$	$2.153 \times 10^{1}\,^{+7.7}_{-7.4}\,\pm 0.6\,\%$	$2.055 \times 10^{0}\,^{+8.4}_{-8.3}\,\pm 1.6\,\%$
		K factor	1.44	1.37	1.26
$(100, 1)$	$m_Y > 2m_X$	$\sigma_{\rm LO}$ [pb]	$1.101 \times 10^{2}\,^{+10.6}_{-9.3}\,\pm 1.6\,\%$	$0.825 \times 10^{1}\,^{+14.4}_{-12.1}\,\pm 1.1\,\%$	$0.854 \times 10^{0}\,^{+17.4}_{-14.1}\,\pm 2\,\%$
		$\sigma_{\rm NLO}$ [pb]	$1.549 \times 10^{2}\,^{+6.8}_{-6.0}\,\pm 0.5\,\%$	$1.127 \times 10^{1}\,^{+7.4}_{-7.2}\,\pm 0.6\,\%$	$1.063 \times 10^{0}\,^{+8.2}_{-8.2}\,\pm 1.2\,\%$
		K factor	1.41	1.37	1.24
$(95, 50)$	$m_Y \lesssim 2m_X$	$\sigma_{\rm LO}$ [pb]	$3.070 \times 10^{0}\,^{+11.6}_{-10.0}\,\pm 1.5\,\%$	$3.359 \times 10^{-1}\,^{+14.9}_{-12.4}\,\pm 1.2\,\%$	$4.457 \times 10^{-2}\,^{+17.7}_{-14.3}\,\pm 1.8\,\%$
		$\sigma_{\rm NLO}$ [pb]	$4.093 \times 10^{0}\,^{+6.0}_{-5.7}\,\pm 0.5\,\%$	$4.302 \times 10^{-1}\,^{+6.7}_{-6.9}\,\pm 0.7\,\%$	$5.079 \times 10^{-2}\,^{+6.9}_{-7.4}\,\pm 1.3\,\%$
		K factor	1.33	1.28	1.14
$(100, 500)$	$m_Y < 2m_X$	$\sigma_{\rm LO}$ [pb]	$2.298 \times 10^{-3}\,^{+18.1}_{-14.5}\,\pm 5\,\%$	$7.839 \times 10^{-4}\,^{+19.5}_{-15.4}\,\pm 5.3\,\%$	$2.558 \times 10^{-4}\,^{+21.2}_{-16.5}\,\pm 6.3\,\%$
		$\sigma_{\rm NLO}$ [pb]	$2.502 \times 10^{-3}\,^{+5.9}_{-6.8}\,\pm 2.5\,\%$	$7.972 \times 10^{-4}\,^{+6.2}_{-7.3}\,\pm 2.6\,\%$	$2.383 \times 10^{-4}\,^{+6.1}_{-7.5}\,\pm 3.0\,\%$
		K factor	1.09	1.02	0.93

Table 2.2: Same as Table 2.1, but for the axial-vector mediator scenario.

crease when the mass scale of the mediator and/or DM increases. The higher $\not{E}_T$ cut leads to smaller K factors and to larger scale and PDF uncertainties, which one can clearly see in the $\not{E}_T$ distributions in Fig. 2.2.

In Table 2.2, we present the pure axial-vector mediator case by fixing the parameters as in Eqs. (2.7), (2.8) and (2.17). The resulting cross sections are very similar compared to the pure vector case for $m_Y > 2m_X$, while in the off-shell regime, we find that the cross sections are suppressed compared to the production via pure vector mediators. In the off-shell situation the DM pair is produced at threshold. A pair of (Dirac) DM originating from a decay of a spin-1 mediator will be in a $^{2S+1}L_J$ state with $J = 1$. If the coupling is vector-like the DM pair can be in a $^3S_1$ state, while if it is axial-like it will be in a $^3P_1$ state, *i.e.* suppressed at threshold. The similar argument holds in case of $gg \to Y_0 + \bar{t}t$ case, as we show in Section 2.3.

The NLO effects are very similar to the vector mediator scenario for all the mass combinations as well as the $\not{E}_T$ cuts. Although we do not show the mixed scenario of vector and axial-vector, one can easily compute such scenarios by changing the coupling parameters in our simplified model.

The parameter point $(m_Y, m_X) = (10, 1)$ GeV warrants special attention, as it illustrates a case of large NLO corrections (so-called "giant K factors" [114]), which might arise in the limit where $p_T^j \gg m_Y, m_X$. The giant K factors in the $pp \to Y_1 + j$ process occur due to the opening of the $pp \to Y_1 + jj$ channel at NLO. This process can lead to a di-jet event topology with a soft, collinear emission of Y_1. In the regime of $p_T^j \gg m_Y$, the Y_1 emission behaves similar to an emission of a massless gauge boson, where the diagrams with dijet topologies contribute factors of $\alpha_s^2 g_X^2 \log^2(p_T^j/m_Y)$, and hence NLO K factors which scale as $\sim \alpha_s \log^2(p_T^j/m_Y)$. Similar features commonly appear in calculations of SM W/Z+jets processes at high jet p_T [114].

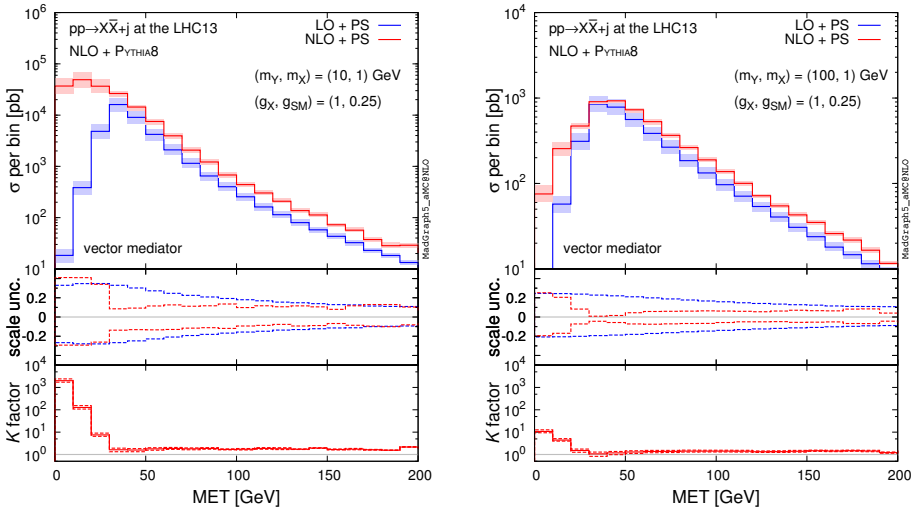


Figure 2.3: $\not{E}_T$ distribution at (N)LO+PS accuracy for $pp \to X\bar{X} + j$ at the 13-TeV LHC for $(m_Y, m_X) = (10, 1)$ GeV (left) and $(m_Y, m_X) = (100, 1)$ GeV (right). The lower panels provide information on the differential scale uncertainty and K factor.

Topologies leading to giant K factors are naturally suppressed in the case of DM production by the cut on $\not{E}_T$. This restricts the calculation to regions of phase space which are insensitive to the soft and collinear double-logs of di-jet event topologies with a soft Y_1 emission. Figure 2.3 (left) illustrates the effect in case of $m_Y = 10$ GeV and $m_X = 1$ GeV. The region of low missing energy displays a two to three orders of magnitude difference in rate between the LO and NLO calculations, whereas we see that above $\not{E}_T > 50$ GeV, the K factor is drastically reduced. On the other hand, we see that already for $(m_Y, m_X) = (100, 1)$ GeV in Fig. 2.3 (right), such logarithmic enhancements are very weak.

2.2.2 Differential distributions

We proceed with the discussion of the features of the differential distributions relevant for DM studies. We begin with Fig. 2.4 which shows the $\not{E}_T$ distributions at LO and NLO for four benchmark points of the simplified model, assuming a pure vector

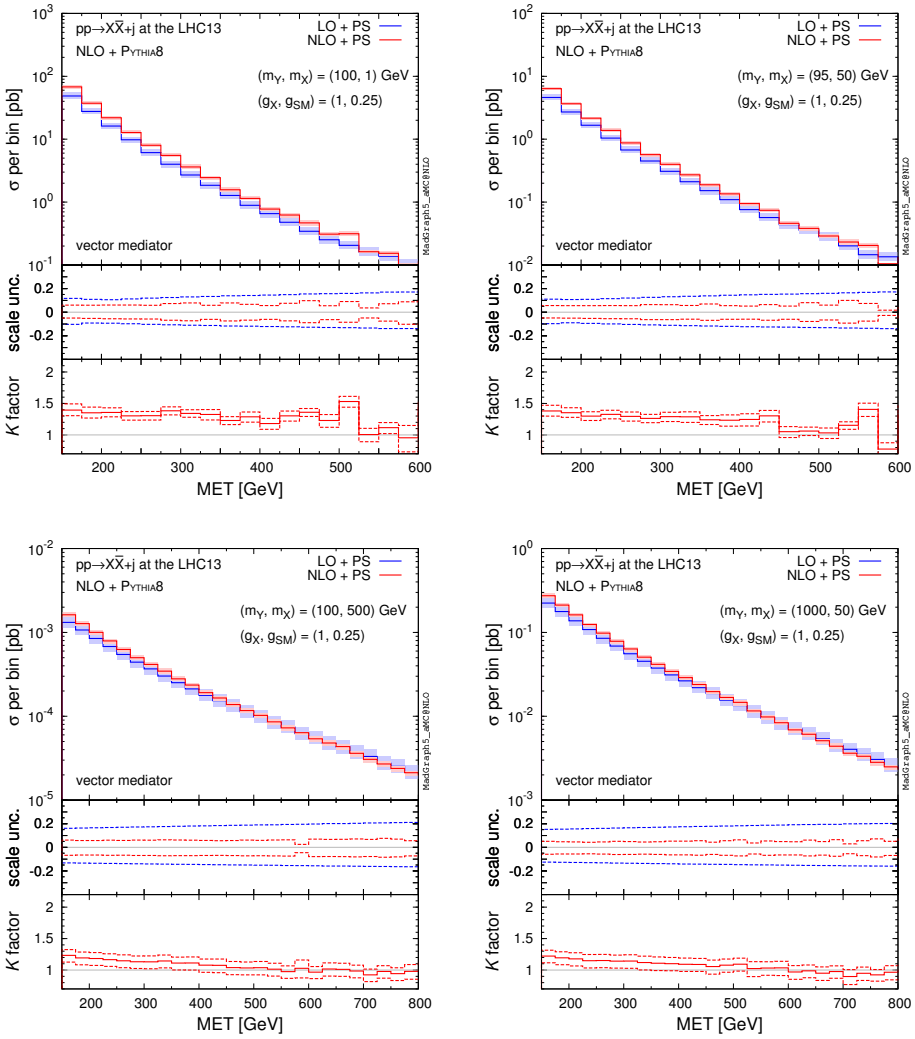


Figure 2.4: $\not{E}_T$ distributions for $pp \to X\bar{X} + j$ at the 13-TeV LHC for four benchmark points specified by (m_Y, m_X), where we assume a pure vector mediator and Dirac DM. The middle and bottom panels show the differential scale uncertainties and K factors, respectively.

mediator and Dirac fermion DM. As seen in the total rates, the NLO effects in the distributions do not depend on the mass relation between the mediator and the DM, $i.e.$ on-shell or off-shell, but do depend on the energy scale of the final state. In the top panels, the energy scale is $\mathcal{O}(100)$ GeV for m_Y or $2m_X$. We find that the two benchmark points display striking similarities in the shape of the $\not{E}_T$ distributions,

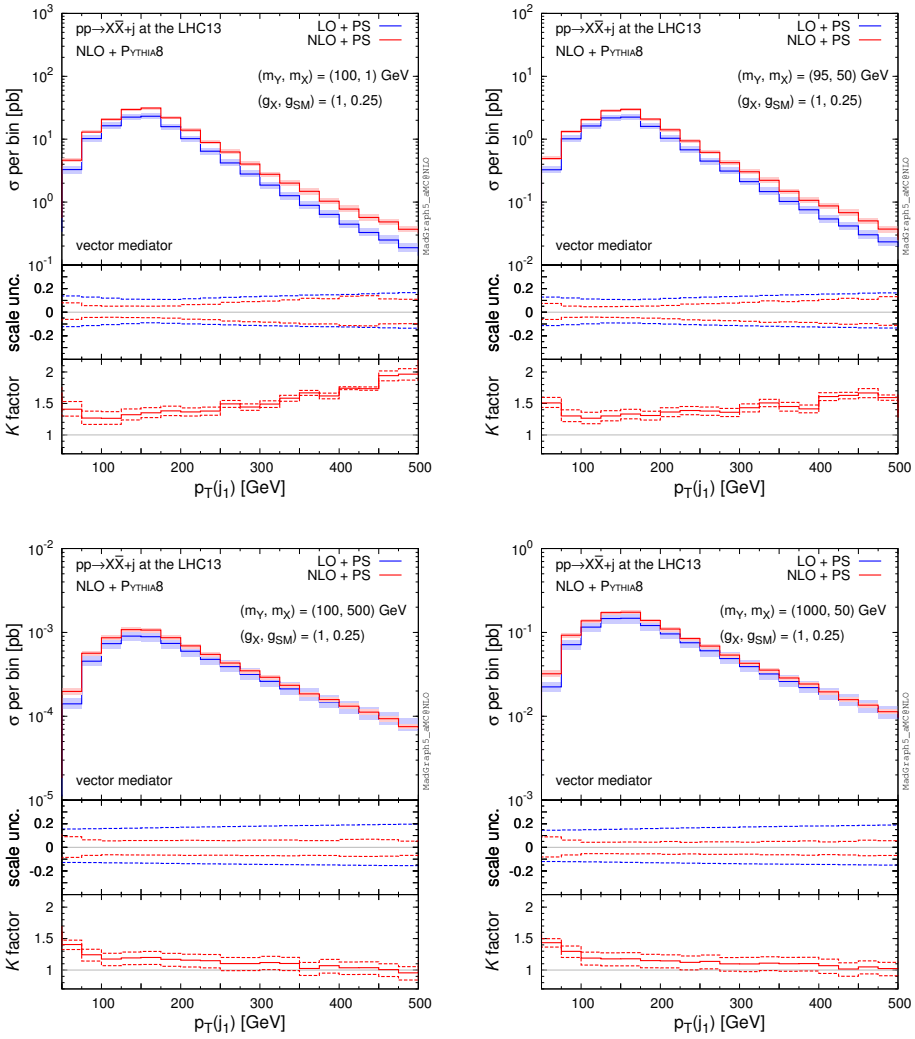


Figure 2.5: p_T distributions of the hardest jet for $pp \to X\bar{X} + j$ at the 13-TeV LHC for four benchmark points specified by (m_Y, m_X), where we assume a pure vector mediator and Dirac DM and the $\not{E}_T > 150\,\text{GeV}$ cut is imposed. The middle and bottom panels show the differential scale uncertainties and K factors, respectively.

while the rate of the latter is suppressed due to off-shell Y_1 production. The largest effects of NLO corrections are in the low $\not{E}_T$ regions, where NLO corrections reach K factors of about 1.4 for $\not{E}_T \sim 150\,\text{GeV}$, with a steady decrease with increasing $\not{E}_T$. We observe similar features also in the high-scale benchmark points of $\mathcal{O}(1)$ TeV for m_Y or $2m_X$ (bottom panels of Fig. 2.4), where the largest K factors are about 1.2

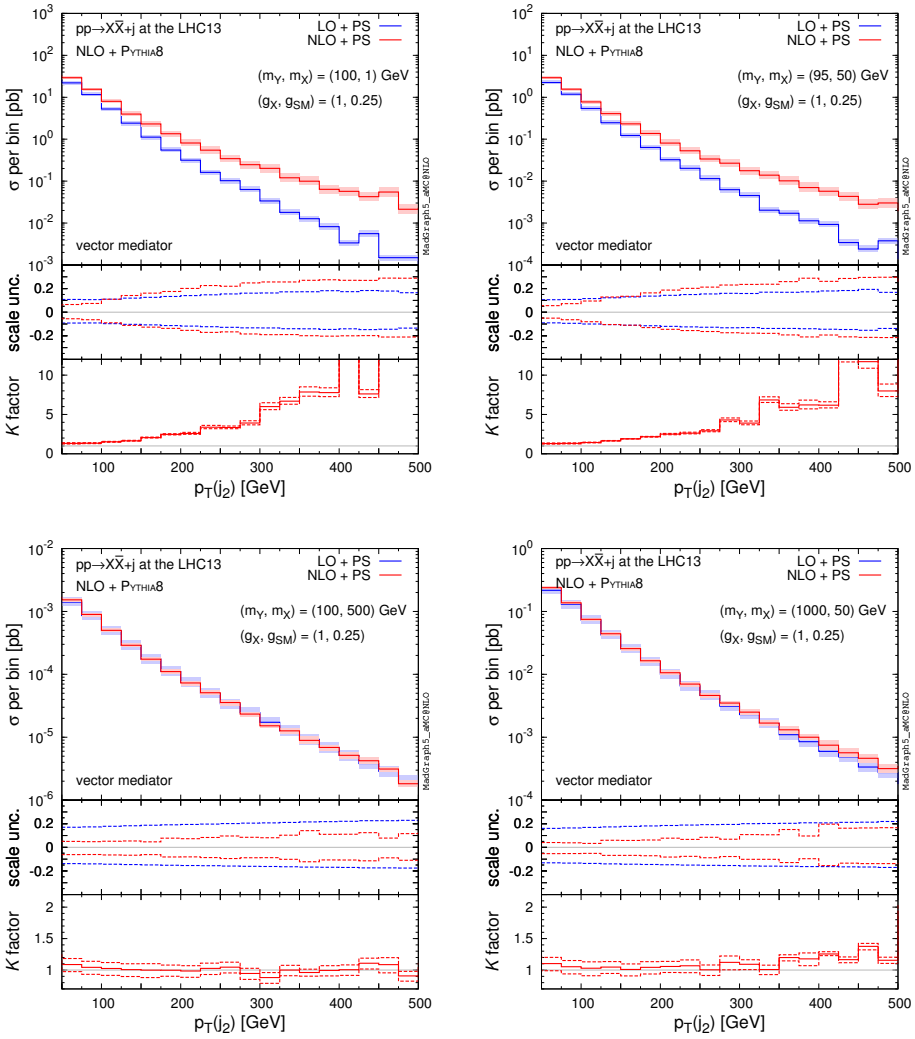


Figure 2.6: Same as Fig. 2.5, but for the second hardest jet.

for $\not{E}_T \sim 150$ GeV. Comparing with the FO distributions in Fig. 2.2, we observe that the parton shower does not affect the $\not{E}_T$ distribution. Note that the NLO corrections are different for different $\not{E}_T$ regions, with the largest NLO corrections occurring in the lower $\not{E}_T$ regions where the rate is the highest. Hence the careful estimation of NLO effects is very important for accurate LHC studies of DM in each signal region.

Next, we study the features of jet kinematic distributions produced in association with DM. Figures 2.5, 2.6, 2.7 and 2.8 show example p_T and η distributions of the hardest

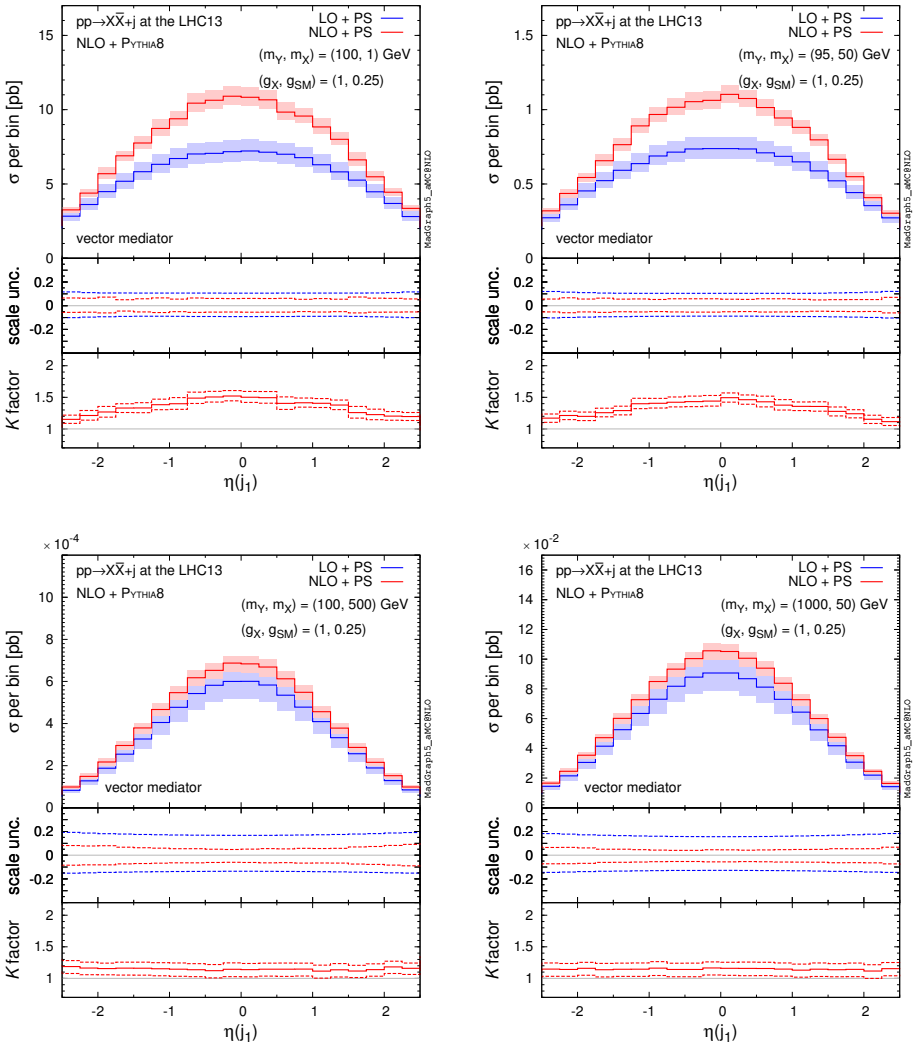


Figure 2.7: η distributions of the hardest jet for $pp \to X\bar{X} + j$ at the 13-TeV LHC for four benchmark points specified by (m_Y, m_X), where we assume a pure vector mediator and Dirac DM and the $\not{E}_T > 150$ GeV cut is imposed. The middle and bottom panels show the differential scale uncertainties and K factors, respectively.

and second hardest jets for the four benchmark points as in Fig. 2.4, assuming

$$\not{E}_T > 150 \text{ GeV} . \tag{2.18}$$

Distributions of the hardest jet transverse momentum show very interesting features. In Fig. 2.5 we find that, in all benchmark points, the LO distributions match the NLO

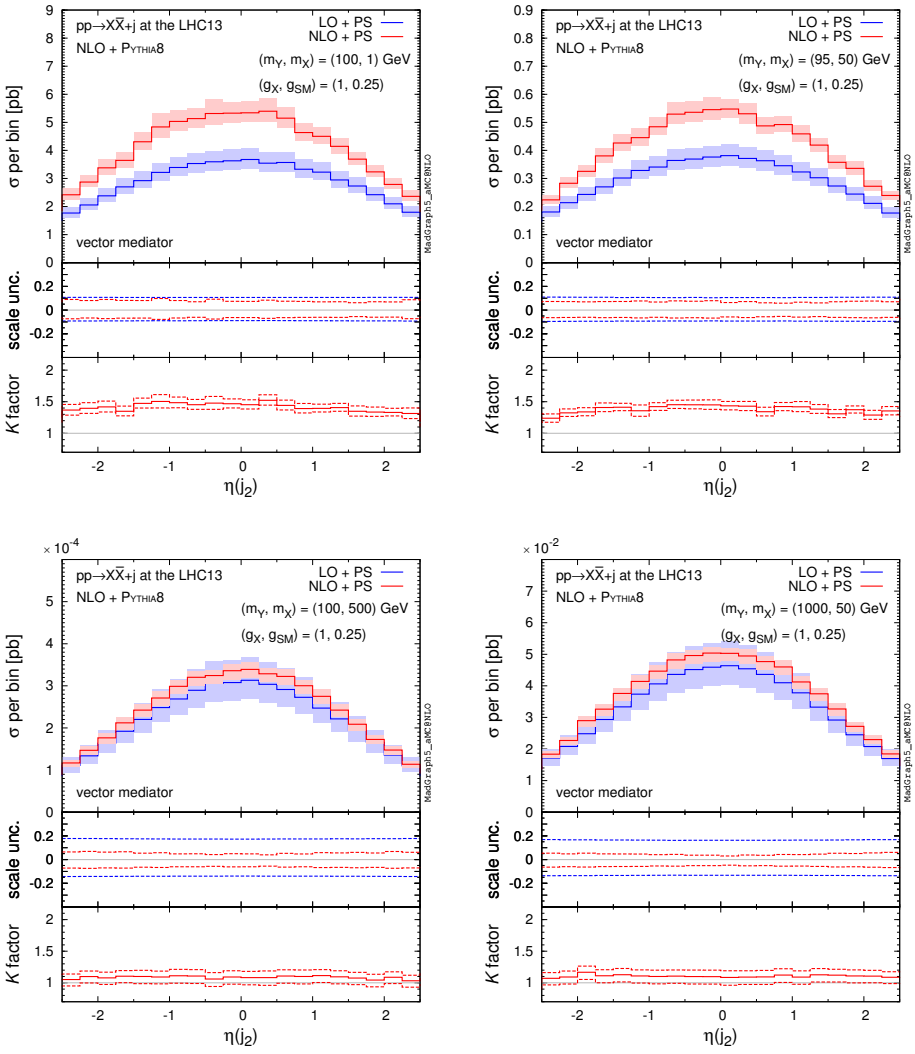


Figure 2.8: Same as Fig. 2.7, but for the second hardest jet.

predictions at the peak, *i.e.* $p_T(j_1) \sim 150$ GeV, to a very good degree. The agreement can be attributed to the imposed $\not{E}_T$ cut in (2.18), which forces the events into a back-to-back configuration of the leading jet and the Y_1 mediator (on average). We also note that the NLO scale uncertainty in the peak region becomes very small compared to the LO estimates.

The NLO corrections to $p_T(j_1)$ distributions affect not only the overall rate, but the shape of the distribution as well. In the low-p_T region, K factors are about $1.2 - 1.5$.

In the high p_T region, we find significant NLO effects again for the $(m_Y, m_X) = (100, 1)$ and (95, 50) GeV cases (top panels), but not for the $(m_Y, m_X) = (100, 500)$ and (1000, 50) GeV cases (bottom panels). We note that the scale uncertainty does not significantly reduce at NLO in the p_T regions away from the peak, especially for the light mediator and DM case (top panels). Significant differences in NLO contributions and theoretical uncertainties in different regions of the $p_T(j_1)$ spectrum suggest that the proper modelling of the hardest jet differential distributions has to go beyond the simple scaling by a constant K factor.

Apart from the highest p_T jet which is modelled by the hard matrix element, all other jets in the LO simulation are generated by the parton shower. By contrast, the NLO corrections include real emission diagrams which can contain two hard and well-separated partons in the final state as well as virtual corrections to one parton emission. One could expect significant differences between LO and NLO in the kinematic distributions of the second highest p_T jet. For the $(m_Y, m_X) = (100, 1)$ and (95,50) GeV cases (top panels), we observe giant K factors in the high-p_T tails of the distributions. The large difference between LO and NLO computations is a consequence of the inadequacy of the parton shower to accurately model high-p_T emissions. In Fig. 2.6 (bottom panels), on the other hand, we find no significant differences between LO and NLO for the overall rate and shape of the second jet emission in case of very heavy mediators ($i.e.$ $m_Y = 1$ TeV) or heavy DM ($i.e.$ $m_X = 500$ GeV), suggesting that the second hardest jet is described very well by the parton shower. This is because the scale of the shower is very high and therefore extra parton emission from the parton shower can be sufficiently hard.

Features similar to those observed in $p_T(j_{1,2})$ also occur in distributions of the (second) hardest jet pseudo-rapidity ($\eta(j_{1,2})$), shown in Figs. 2.7 and 2.8. For the light mediator/DM (top panels), we observe that the rate at which the hardest jet is emitted at NLO in the low rapidity region is enhanced by a factor about 1.5, with the corrections falling off with the increase in rapidity. However, even though the overall rate for the second-hardest jet increases by a factor of roughly ~ 1.5 the shape of the $\eta(j_2)$ distribution is affected only mildly. In the case of heavy mediator/DM, the hardest jet is emitted at a lower rapidity (on average) at a significantly higher rate compared to light mediators as illustrated by the width of the η distributions in Fig. 2.7. As the hardest jet typically recoils against $\not{E}_T$, this explains why the $\not{E}_T$ spectrum falls off more quickly for lighter mediators than for the heavier ones.

In addition to total and differential production cross sections for the $pp \to X\bar{X} + j$ process, we study NLO effects for different jet multiplicities in the final state using the FxFx merging procedure [79] within the framework of MG5_aMC. We consider

$$pp \to X\bar{X} + 0, 1, 2 \,\text{jets}\,. \tag{2.19}$$

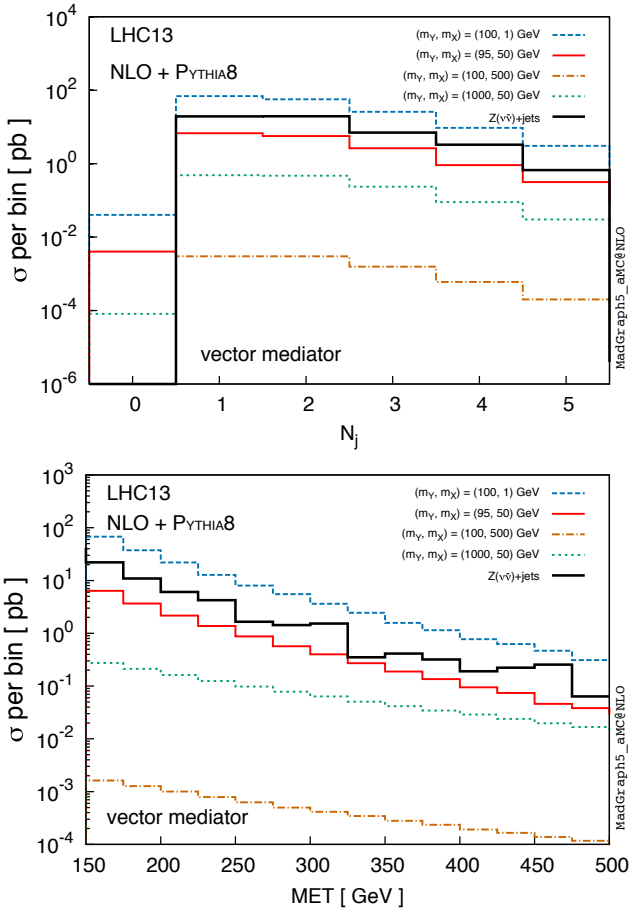


Figure 2.9: N_j and $\not{E}_T$ distributions for various signal benchmark points and $Z(\nu\bar{\nu})+$ jets, where $\not{E}_T > 150$ GeV and jets with $p_T > 30$ GeV and $|\eta| < 4.5$ are considered. We assume a pure vector mediator and Dirac DM with the coupling parameters $g_X = 1$ and $g_{\rm SM} = 0.25$.

with merging scales at 45 and 30 GeV for 2- and 1-jet merged samples, respectively. We find that effects of jet merging at NLO are mild and within 10%.

2.2.3 Comparison of signal distributions to the Standard Model

In discussions of NLO corrections to DM production, it is important to consider how the possible signal events at NLO look in the midst of large SM backgrounds. For the purpose of illustration, we consider only the largest background in mono-jet searches for DM, *i.e.* Z+jets and simulate it to NLO merged up to 2 extra jets via the FxFx method.

Figures 2.9 and 2.10 show an example comparison of the Z+jets channel to several benchmark points of the simplified model discussed in previous sections. The shape of signal jet multiplicity distributions resembles the Z+jets distribution to a good degree, while the overall rate varies wildly depending on the model point. Note that events containing one jet are produced at almost an identical rate to $2j$ events and comparable to $3j$ events, both in Z+jets and all of the benchmark model points we considered. The production rate for different jet multiplicities implies that it could be beneficial to consider DM searches beyond mono-jet, either inclusive, or at fixed jet multiplicities.

Next, the $\not{E}_T$ (as well as the hardest jet p_T) distributions for mediators of mass $\sim 100\ \mathrm{GeV}$ with light DM naturally resemble the Z+jets distribution in shape, as the kinematics of the $\not{E}_T$ and hardest jet are determined by the mass scale of the heavy object ($i.e.$ the Z boson or the mediator). For heavy mediators, the $\not{E}_T$ and $p_T(j_1)$ distributions fall off with a milder slope, suggesting that the signal to background ratio (S/B) in searches for DM could be improved by requiring a higher p_T^{min} for the hardest jet.

The p_T distribution of the second hardest jet, on the other hand, seems to display a similar shape in all model points, as well as the Z+jets background channel. Requiring a high p_T on the second jet would hence not improve neither S/B nor the signal significance, suggesting that in searches which exploit the presence of a second jet, only minimum cuts on $p_T(j_2)$ should be applied. Note that the modelling of the second jet from LO calculations grossly underestimates the overall rate in case of lighter mediators for $p_T \gtrsim 100\ \mathrm{GeV}$, as illustrated in Fig. 2.6.

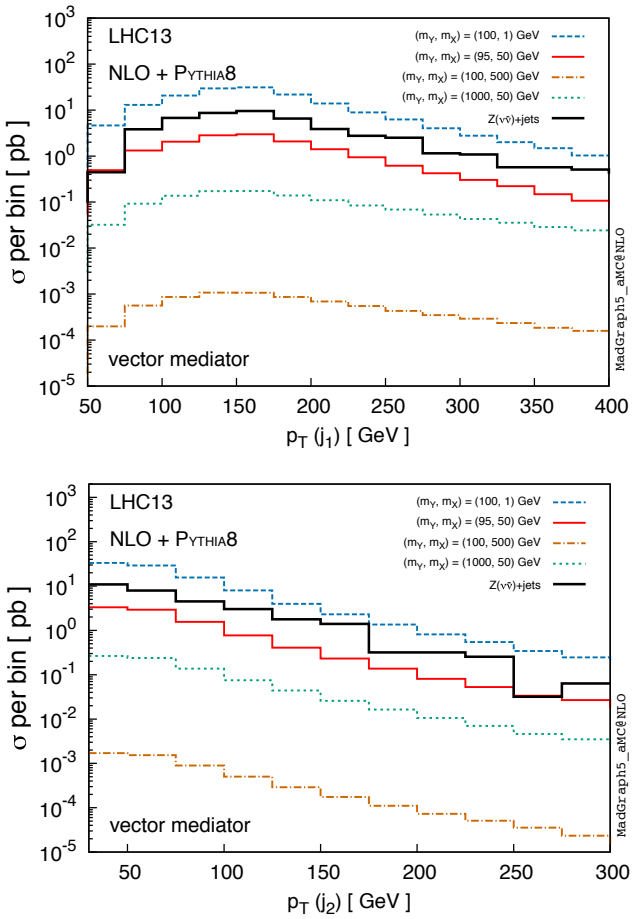


Figure 2.10: Same as Fig. 2.9 but for $p_T(j_1)$ and $p_T(j_2)$ distributions.

2.3 Dark matter production with a top-quark pair

In the spin-0 mediator model, due to the normalisation of the Yukawa couplings in the Lagrangian (2.11), the most relevant tree-level process at the LHC is

$$pp \to X\bar{X} + t\bar{t}\,. \tag{2.20}$$

Such models have in the past been studied in the context of EFT [115–117] and simplified models [104, 106], and searched for at the LHC Run I [118, 119]. Past work on DM interactions with the top quarks has mainly focused on LO estimates, with only

(m_Y, m_X) [GeV]			scalar	pseudo-scalar
10	undecayed	$\sigma_{\rm LO}$ [pb]	$2.278 \times 10^{1}\,^{+28.0}_{-20.4}\,\pm 4.2\,\%$	$5.202 \times 10^{-1}\,^{+30.8}_{-22.0}\,\pm 6.0\,\%$
		$\sigma_{\rm NLO}$ [pb]	$2.435 \times 10^{1}\,^{+5.4}_{-8.5}\,\pm 1.8\,\%$	$5.431 \times 10^{-1}\,^{+7.4}_{-10.2}\,\pm 2.6\,\%$
		K factor	1.07	1.04
(10, 1)	$m_Y > 2m_X$	$\sigma_{\rm LO}$ [pb]	$2.294 \times 10^{1}\,^{+28.0}_{-20.5}\,\pm 4.2\,\%$	$5.500 \times 10^{-1}\,^{+30.8}_{-22.1}\,\pm 6.0\,\%$
		$\sigma_{\rm NLO}$ [pb]	$2.460 \times 10^{1}\,^{+5.4}_{-8.5}\,\pm 1.8\,\%$	$5.739 \times 10^{-1}\,^{+7.4}_{-10.2}\,\pm 2.6\,\%$
		K factor	1.07	1.04
(10, 50)	$m_Y < 2m_X$	$\sigma_{\rm LO}$ [pb]	$2.415 \times 10^{-3}\,^{+30.5}_{-21.8}\,\pm 5.8\,\%$	$3.329 \times 10^{-3}\,^{+33.9}_{-23.8}\,\pm 8.7\,\%$
		$\sigma_{\rm NLO}$ [pb]	$2.340 \times 10^{-3}\,^{+5.8}_{-9.1}\,\pm 2.8\,\%$	$3.133 \times 10^{-3}\,^{+7.5}_{-11.0}\,\pm 3.9\,\%$
		K factor	0.97	0.94
100	undecayed	$\sigma_{\rm LO}$ [pb]	$8.226 \times 10^{-1}\,^{+28.7}_{-20.9}\,\pm 4.4\,\%$	$2.442 \times 10^{-1}\,^{+32.2}_{-22.9}\,\pm 7.2\,\%$
		$\sigma_{\rm NLO}$ [pb]	$8.391 \times 10^{-1}\,^{+5.3}_{-8.6}\,\pm 2.1\,\%$	$2.431 \times 10^{-1}\,^{+7.6}_{-10.7}\,\pm 3.2\,\%$
		K factor	1.02	1.00
(100, 1)	$m_Y > 2m_X$	$\sigma_{\rm LO}$ [pb]	$8.135 \times 10^{-1}\,^{+28.8}_{-20.9}\,\pm 4.4\,\%$	$2.464 \times 10^{-1}\,^{+32.4}_{-23.0}\,\pm 7.2\,\%$
		$\sigma_{\rm NLO}$ [pb]	$8.207 \times 10^{-1}\,^{+4.8}_{-8.3}\,\pm 2.1\,\%$	$2.427 \times 10^{-1}\,^{+7.0}_{-10.4}\,\pm 3.2\,\%$
		K factor	1.01	0.98
(95, 50)	$m_Y \lesssim 2m_X$	$\sigma_{\rm LO}$ [pb]	$7.986 \times 10^{-3}\,^{+29.5}_{-21.3}\,\pm 5.0\,\%$	$1.404 \times 10^{-2}\,^{+32.9}_{-23.3}\,\pm 7.8\,\%$
		$\sigma_{\rm NLO}$ [pb]	$7.897 \times 10^{-3}\,^{+5.5}_{-8.8}\,\pm 2.4\,\%$	$1.362 \times 10^{-2}\,^{+7.4}_{-10.8}\,\pm 3.5\,\%$
		K factor	0.99	0.97
1000	undecayed	$\sigma_{\rm LO}$ [pb]	$1.571 \times 10^{-3}\,^{+40.2}_{-27.0}\,\pm 17.1\,\%$	$1.827 \times 10^{-3}\,^{+40.4}_{-27.1}\,\pm 17.4\,\%$
		$\sigma_{\rm NLO}$ [pb]	$1.127 \times 10^{-3}\,^{+10.9}_{-13.6}\,\pm 8.7\,\%$	$1.297 \times 10^{-3}\,^{+10.8}_{-13.7}\,\pm 8.8\,\%$
		K factor	0.72	0.71
(1000, 1)	$m_Y > 2m_X$	$\sigma_{\rm LO}$ [pb]	$7.499 \times 10^{-4}\,^{+40.8}_{-27.2}\,\pm 16.8\,\%$	$8.174 \times 10^{-4}\,^{+40.9}_{-27.3}\,\pm 17.0\,\%$
		$\sigma_{\rm NLO}$ [pb]	$5.201 \times 10^{-4}\,^{+8.4}_{-12.7}\,\pm 8.4\,\%$	$5.675 \times 10^{-4}\,^{+8.6}_{-12.9}\,\pm 8.5\,\%$
		K factor	0.69	0.69
(1000, 50)	$m_Y > 2m_X$	$\sigma_{\rm LO}$ [pb]	$7.354 \times 10^{-4}\,^{+40.7}_{-27.2}\,\pm 16.8\,\%$	$8.137 \times 10^{-4}\,^{+41.0}_{-27.3}\,\pm 17.0\,\%$
		$\sigma_{\rm NLO}$ [pb]	$5.125 \times 10^{-4}\,^{+8.6}_{-12.8}\,\pm 8.5\,\%$	$5.595 \times 10^{-4}\,^{+8.3}_{-12.7}\,\pm 8.5\,\%$
		K factor	0.69	0.69

Table 2.3: LO and NLO cross sections and corresponding K factors for DM pair production in association with a top-quark pair for the scalar and pseudo-scalar mediator scenario at the 13-TeV LHC. The uncertainties represent the scale and PDF uncertainties in per cent, respectively. We show several benchmark model points for the mediator and DM masses with the coupling parameters $g_X = 1$ and $g_{\rm SM} = 1$.

a few analyses including NLO corrections. Here we present a comprehensive study of NLO effects of DM interaction with top quarks in the framework of the simplified model. We note that a wide class of so called "top-philic DM" models exist where the LO production is via top loops. Ref. [120] studied such a scenario in a minimally model-dependent framework, while more recently, Ref. [102] presented concrete predictions for loop-induced DM production for the current LHC13 run, using the same simulation framework as in this work.

The code and events for the above process can be automatically generated by issuing the following commands in MG5_AMC:

```
> import model DMsimp_s_spin0
> generate p p > xd xd~ t t~ [QCD]
> output
> launch
```

We have checked that our model can reproduce the SM predictions for $pp \to ht\bar{t} \to \tau^+\tau^- t\bar{t}$ by adjusting the coupling and mass parameters. Note that we use the on-shell renormalisation for the NLO model construction. The top-quark decays can be subsequently performed by MADSPIN [121], which keeps production and decay spin correlations.

To illustrate the NLO effects, we consider pure scalar, Eqs. (2.12) and (2.13), or pure pseudo-scalar, Eqs. (2.14) and (2.15), couplings, and take

$$g_X = 1 \quad \text{and} \quad g_{\rm SM} = 1 \tag{2.21}$$

as the default couplings. With these values, the scalar and pseudo-scalar mediator width is $\Gamma_Y/m_Y \sim 0.06 - 0.1$ for $m_Y > 2m_X, 2m_t$, while $\Gamma_Y/m_Y \sim 0.04$ for $m_Y > 2m_X$ and $m_Y < 2m_t$. The width for scalar is slightly smaller due to the additional β^2 factor where $\beta = (1 - 4m^2_{X,t}/m^2_Y)^{1/2}$.

2.3.1 Total cross sections

We start by showing total production rates of $pp \to X\bar{X} + t\bar{t}$, where the top quark is considered stable. Table 2.3 shows the LO and NLO cross sections (in pb) for the scalar and pseudo-scalar mediator scenarios, where we use $m_t = 172$ GeV. The central renormalisation and factorisation scales are set to half the sum of the transverse mass of the top quarks and the missing transverse energy. We also present scale and PDF uncertainties in % as well as K factors.

For the total production rates, the NLO effects are very mild for the light mediator case, while they are significant for the heavy case. The inclusion of NLO corrections results in a considerable improvement of the scale uncertainties, from up to 40% at LO to typically only about 10% at NLO. Also, the PDF uncertainties are reduced by approximately a factor of two when going from LO to NLO.

Table 2.3 also shows clear differences between the overall production rates in the cases of scalar and pseudo-scalar mediators. For mediator mass of $\mathcal{O}(10)$ GeV we find that DM production cross section via scalar mediators is an order of magnitude larger compared to the production rate via the pseudo-scalar mediator with the same

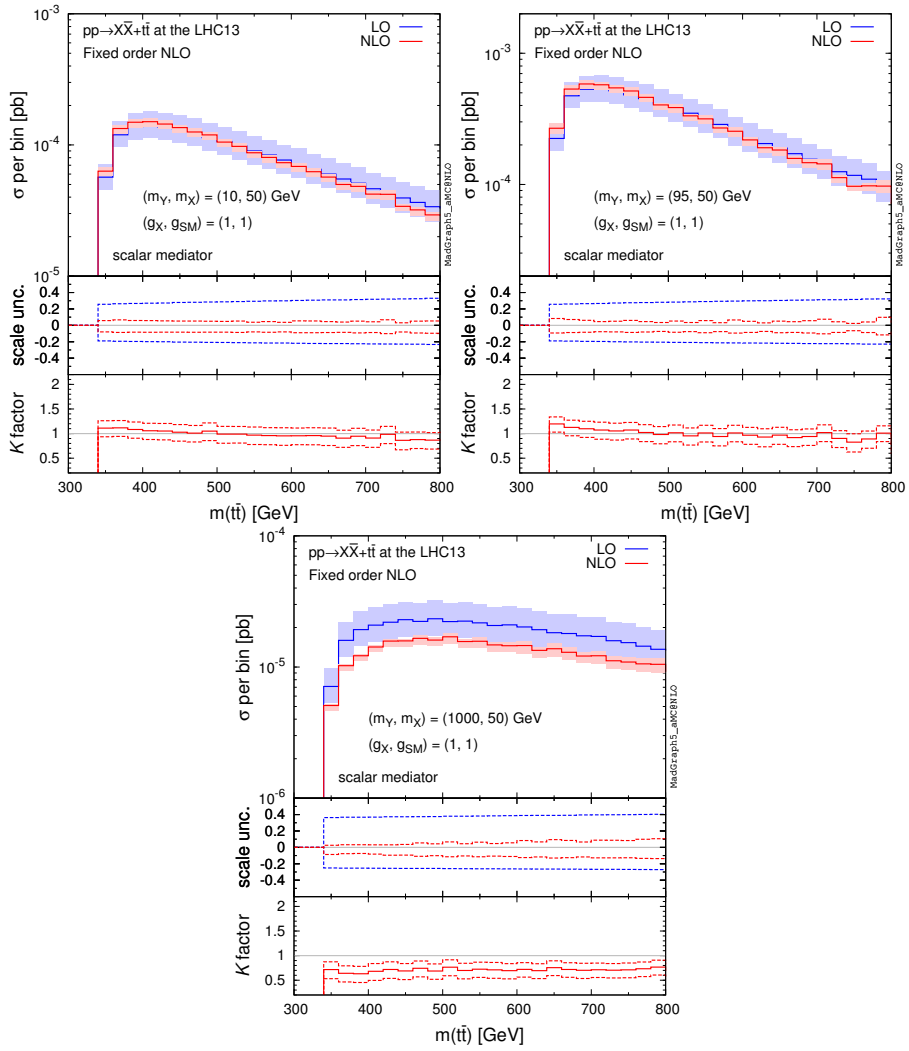


Figure 2.11: Distribution of the invariant mass of the top-quark pair for $pp \to X\bar{X}+t\bar{t}$ at the 13-TeV LHC for different mediator masses with the DM mass fixed at 50 GeV, where we assume a pure scalar mediator and Dirac DM. The middle and bottom panels show the differential scale uncertainties and K factors, respectively.

mass. The large difference occurs due to the fact that in case of $m_X < m_Y \ll m_t$, the production cross section is dominated by the $t \to tY_0$ fragmentation. In case of the scalar mediator, the $t \to tY_0$ fragmentation function contains terms with soft singularities of the form $(1-x)/x$ – where x is the momentum fraction carried by

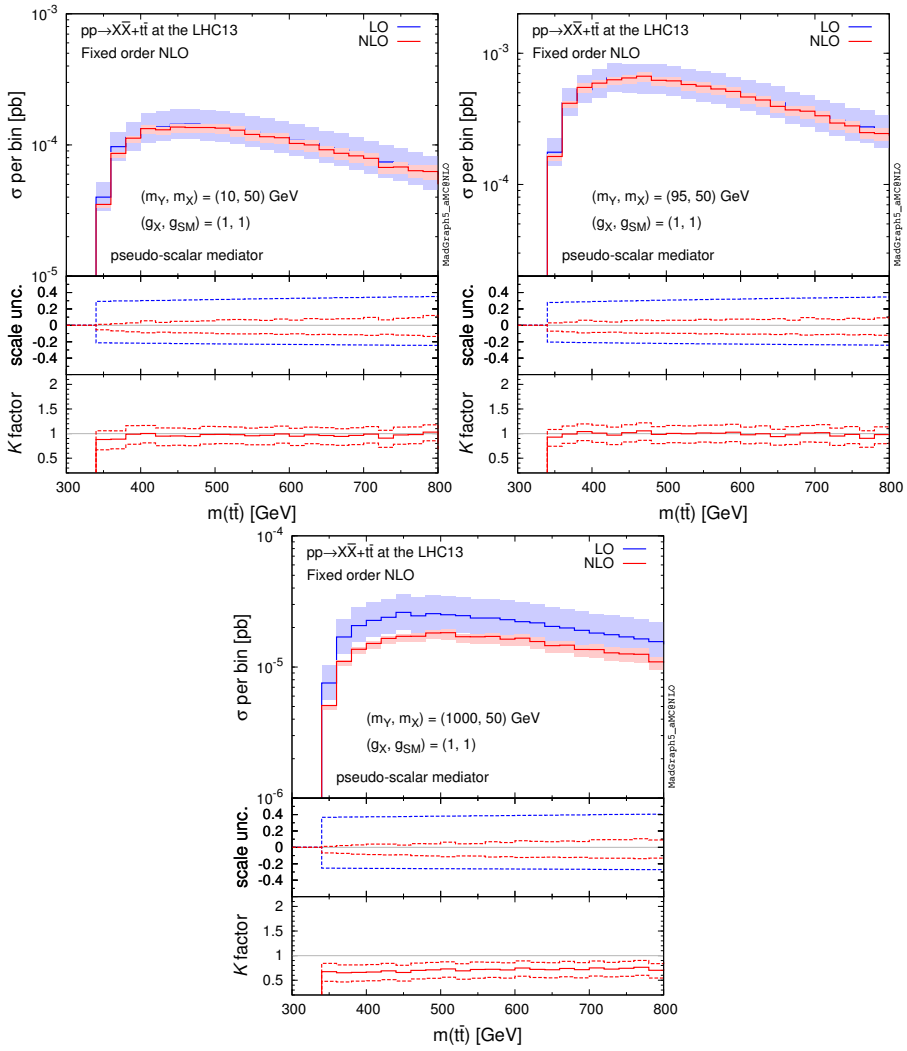


Figure 2.12: Same as Fig. 2.11, but for the pseudo-scalar mediator scenario.

the mediator – causing enhancements in the production rate [122]. The soft-enhanced term is absent in the case of a pseudo-scalar mediator [123], explaining the order of magnitude difference between the total rates of the scalar and pseudo-scalar mediators.

In cases where either DM or the mediator is produced close to threshold, we observe that the production cross section in the pseudo-scalar mediator case is larger. The effect can be attributed to the production rate originating mainly from top fusion diagrams. The production of a DM (Dirac) pair via scalar mediators $t\bar{t} \to Y_0 \to X\bar{X}$

at threshold can proceed only via a P-wave ($^3P_0$) and is hence suppressed by extra two powers of $\beta = \sqrt{1-4m_t^2/s}$ [124]. Conversely, production of DM pair via pseudo-scalar mediators can proceed via an S-wave ($^1S_0$) and hence does not suffer any kinematic suppression.

2.3.2 Differential distributions

For the study of differential distributions, we consider the invariant mass of the top-quark pair ($m(t\bar{t})$), without inclusion of a parton shower. Figures 2.11 and 2.12 illustrate the scalar and pseudo-scalar results, respectively, for different mediator masses (off-shell, threshold, and on-shell) with the DM mass fixed at 50 GeV. In all cases the shape of $m(t\bar{t})$ is well modelled by the LO calculation, and including a constant K factor reproduces the NLO results to an excellent degree, except in the threshold region. However, the LO calculation suffers from significant scale uncertainties which tend to increase with $m(t\bar{t})$, whereas the scale uncertainties are under much better control at NLO.

Whether DM is produced via scalar or pseudo-scalar mediators can have a dramatic effect on the shape of the $m(t\bar{t})$ distribution. In Fig. 2.13 we compare the NLO distributions in Figs. 2.11 and 2.12, where we normalise the histograms to unit area to point out the shape differences. We observe that the shape of the distribution is particularly enhanced for $m(t\bar{t}) \gtrsim 500$ GeV in the case of the pseudo-scalar mediator, while the scalar mediator distribution displays a much more prominent peak at lower $m(t\bar{t})$. The effect is severely damped in case of heavy mediators, where we find no clear differences between the shapes of the scalar and pseudo-scalar mediator distributions. Figure 2.13 suggests that scalar and pseudo-scalar mediators could be distinguished based on the shape of the $m(t\bar{t})$ distribution, as long as the mediator is sufficiently light and/or does not decay highly off-shell. An analogous observation has been made already in the case of the study of the CP properties of the Higgs boson [125].

2.4 Summary and comment on t-channel simplified models

Searches for DM are one of the main endeavours at the LHC Run II. Accurate and precise predictions for production rates and distributions are necessary to obtain robust constraints on DM models and characterise possible DM signals. In this chapter we have provided a general implementation of the simplified DM model approach into a calculation/simulation framework that allows to systematically evaluate and include

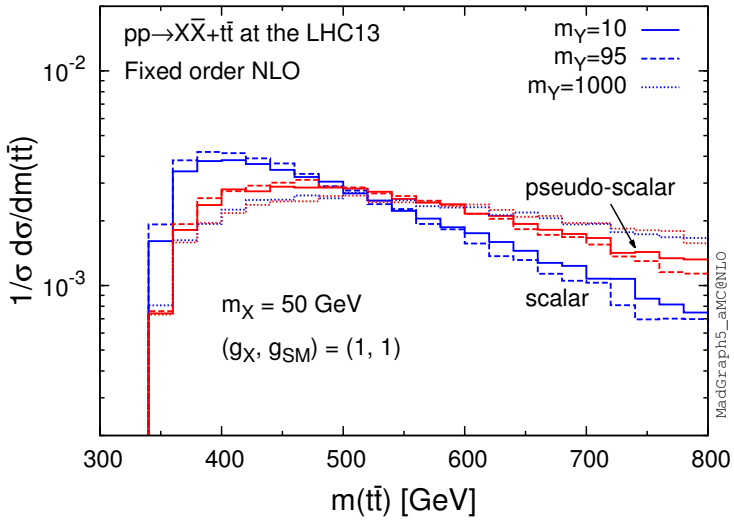


Figure 2.13: Comparison of $t\bar{t}$ invariant mass distributions between the scalar (blue) and pseudo-scalar (red) mediator models for different mediator masses.

NLO QCD corrections to the production of DM at the LHC. We have considered a class of simplified models where DM is a Dirac fermion and couples to the SM via either spin-1 or spin-0 s-channel mediators, making no restrictions on chiral couplings. For the purpose of illustration, we analysed the NLO effects on the DM production via vector and axial-vector mediators in the context of mono-jet signals. In addition, we have presented detailed predictions of DM production in association with a top-quark pair via scalar and pseudo-scalar mediators. We presented our results for various DM and mediator masses to cover benchmark points suggested by the ATLAS/CMS DM forum [69].

For $\not{E}_T$+jets in the spin-1 mediator model, our results show that higher-order corrections have a significant effect both on the overall production rate as well as on the shape of relevant differential distributions, with a sizeable reduction of the scale and PDF uncertainties. The NLO corrections to the LO production rates can be large, with K factors of up to $K \lesssim 2$, and typically occur in parts of the model parameter space where the mass scale of DM and mediator is $\mathcal{O}(10 - 100)$ GeV. For such scenarios, we also find large NLO effects on the shape of differential distributions in $\not{E}_T$ and the transverse momentum of the associated jets. Simplified models with heavy ($e.g.$ $\mathcal{O}(1)$ TeV) mediators/DM do not receive large NLO corrections, and we find that LO predictions describe both total production rates and shapes of differential distributions quite accurately. Distributions of the second hardest jet in the event are well modelled by the parton shower for heavy mediator/DM cases. On the other hand, for media-

tors/DM with masses of $\mathcal{O}(100)$ GeV, the inclusion of NLO effects is essential for a proper description of $p_T(j_2)$ and $\eta(j_2)$ distributions, especially in the high-p_T tails, where the NLO effects can be an order of magnitude.

Comparisons with the NLO predictions for the leading SM background channel reveal that considerations of either inclusive or exclusive jet samples beyond one jet could be beneficial for increasing the prospects for DM detection. The leading jet p_T distributions in case of heavy mediators display a milder decrease with the increase in p_T, suggesting that a significant improvement in S/B could be obtained by focusing on high-p_T regions. The second hardest jet p_T distribution, on the other hand, was characterised by a slope similar to the leading backgrounds, implying that more inclusive cuts on the second jet should be used.

For $\not{E}_T + t\bar{t}$ in the spin-0 mediator model, our results show that the NLO corrections are very mild for the light mediator case, while they are significant for the heavy case. We observed a drastic improvement of the theory uncertainties when going from LO to NLO. We have noted that the shape of the $m(t\bar{t})$ distribution can reveal the chiral structure of the DM-SM interactions, as long as the mediator is relatively light ($i.e.$ $\lesssim \mathcal{O}(100)$ GeV).

Then we comment on t-channel simplified models. A DM t-channel simplified model couples directly the DM candidate to a SM field through a mediator. This mediator could then be coloured. This new approach leads to a different phenomenology compared to s-channel simplified models, but has not been so extensively studied in the past. Actually the technology is ready to study such mechanisms in the MG5_AMC framework. Indeed we have put forward the interpretation of the mono-object signals in the SUSY context with a very light gravitino for the LHC in Ref. [2]. Extending the gravitino EFT to simplified SUSY models, other production channels can contribute leading to rather different final state features that in turn depend on the SUSY parameters. In this work we presented the complete set of production channels consistently treated in a unique framework that can provide accurate predictions for the general case *i.e.* gravitino pair production, gluino and squark pair production and associated gravitino production with gluinos and squarks which involves t-channel squark and gluino exchange. In addition, although the gravitino in our scenario is too light to be a cold DM candidate, the approach we have followed is fully general and can be used as a template for passing from an EFT approach to t-channel simplified models in the context of DM searches.

In conclusion, s-channel simplified models for DM will drive the future analyses at LHC Run II. However, we saw in this chapter that a proper treatment of NLO corrections is necessary to allow an accurate interpretation of the results. Therefore, such treatments should continue for future results at LHC. As a future perspective, a complete analysis of t-channel simplified models at NLO should be relevant to extract the

associated phenomenology. This goal could be achieved by exploiting our results in Ref. [2].

Chapter 3

MadDM: a numerical tool for dark matter physics

"We can only see a short distance ahead, but we can see plenty there that needs to be done."

Alan Turing (1912 - 1954)

Searching for DM at the interface of collider physics, astroparticle physics and cosmology is perhaps the most promising path to discovery and discrimination of different DM models, which requires substantial amount of computational power and relevant tools. While many collider event generators are publicly available [126], the number of numerical tools which are able to calculate signals of DM at the interface of collider physics and astroparticle physics remains very limited [127, 128]. MADDM [129] emerged as an attempt to build such a tool. The goal of the MADDM project is to form a simple, user friendly and all-in-one DM phenomenology framework in order to allow both experimentalists and theorists to calculate accurate signatures of generic DM models at colliders, in our galaxy and in the early Universe with only a few clicks of a button. We also aim to provide flexibility such that users easily replace the existing modules with their own implementation or link MADDM functionality with other existing tools.

The user friendly architecture of the MG5_AMC [78, 130] package provides an ideal framework for the development of MADDM. Numerous MG5_AMC additions and extensions offer many interesting directions that development of MADDM can go

into. Version 1.0 of MADDM focused on computation of DM relic density in a generic model [129]. Here we discuss the next step in the development of MADDM: direct detection of galactic DM. In addition to the ability to calculate DM-nucleon cross sections, MADDM v.2.0 goes a step further and provides the directional information of nuclear recoil, as well as the ability to simulate the effects of detector systematics on recoil distributions. To the best of our knowledge, MADDM is the first publicly available code with such a capability. The code is able to calculate double differential recoil rates, as a function of recoil angle and energy, as well as the energy distribution and angular distribution of nuclear recoil.

Directional information of DM scattering can be of great importance for the next generation of DM direct detection experiments. In case a DM signal is observed, directional information about nuclear recoil rates could lead to more precise measurements of intrinsic particle properties of DM [131] as well as astrophysical information such as the DM velocity distribution [132,133]. Conversely, if next generation direct detection experiments lead only to more stringent limits on DM mass and scattering cross section, directional detection could become crucial in overcoming the irreducible neutrino background [134].

Finally, MADDM v.2.0 incorporates a simplified functionality for testing model points against experimental constraints, whereby the user can choose the range of DM relic densities and upper bounds on DM-nucleon scattering cross sections for which the model is consistent with the experiments. The code will automatically compare the output of the calculation to the user specified constraints and determine whether the model point is allowed or not.

New version of MADDM follows the already established structure of MADDM v.1.0. A `Python` module generates relevant amplitudes for relic density and direct detection (with ALOHA [86]), while a `FORTRAN` module handles the heavy numerical calculations. As before, MADDM is compatible with UFO (Universal FeynRules Output [85]) model which contains a DM candidate and can be easily linked to any width or mass spectrum generator which can produce a Les Houches formatted parameter card [135,136].

The following sections describe the new functionality of the MADDM code for the direct detection of DM, while we refer the reader to Ref. [129] for more information on numerical calculation of DM relic density. Section 3.1 describes the theoretical background of DM direct detection, including directionality. We show several validations and example calculations using the MADDM v.2.0 code in Section 3.2. We finally summarise and give future prospects for the development of MADDM in Section 3.3. Appendix A is reserved for a description of the new MADDM code structure and conventions.

3.1 Review of direct detection and its implementation in MADDM

3.1.1 DM-nucleon elastic cross section

The possibility that DM could weakly interact with ordinary matter has led to a development of a myriad of experiments which search for signatures of galactic DM scattering off nuclei [137–141]. Being sensitive to the nuclear recoil of the scattering DM-nucleon event in underground detectors, experiments can constrain model parameters involved in the DM-nucleon (nucleus) elastic scattering cross section, while in the case of a discovery, the same information may be used to determine properties of DM particles. The abundance of independent experiments has so far led to important limits on the DM-nucleus cross section, among which the most recent (and most stringent) one comes from the LUX collaboration [53, 137, 142]. In this section, we give an overview of the theoretical formalism of DM-nucleus elastic scattering in order to allow the reader to understand the procedures MADDM performs in computing DM direct detection rates [143–145].

The MADDM v.2.0 code incorporates the following definition of the DM-nucleus **spin-independent** (SI) scattering cross section:

$$\sigma_{SI} = \frac{4}{\pi}\mu_A^2 \cdot \left[Z \cdot f_p + (A - Z) \cdot f_n\right]^2 , \tag{3.1}$$

where $\mu_A = \frac{m_\chi m_A}{m_\chi + m_A}$ is the DM-nucleus reduced mass and f_p (f_n) is the proton (neutron) spin-independent form factor [132, 134, 146]. We use Z to denote the number of protons in a nucleus and A to denote the number of protons and neutrons. Similarly, for **spin-dependent** (SD) interactions, we use the definition:

$$\sigma_{SD} = \frac{16}{\pi}\mu_A^2 \cdot \frac{J_A + 1}{J_A}\left(f_p' + f_n'\right)^2 , \tag{3.2}$$

where f_p' and f_n' are the proton/neutron spin-dependent form factors respectively, and J_A is the spin of the nucleus. Particle physics enters the calculation of $\sigma_{SD/SI}$ via the form factors f_N and f_N' where $N = p, n$.

The spin-independent quantity for a scalar current, f_N^S is defined as

$$f_N^S = m_N \sum_{q=u,d,s} \frac{\alpha_q}{m_q} f_N^{Sq} + \frac{2}{27} m_N f_N^{SG} \sum_{q=c,b,t} \frac{\alpha_q}{m_q}, \tag{3.3}$$

where α_q are the coefficients of the low energy matrix elements defined by

$$\langle \mathcal{M} \rangle (\chi q \to \chi q) = \alpha_q \left\langle \bar{\psi}_q \psi_q \right\rangle . \tag{3.4}$$

The quantities $f_N^{S\,q/G}$ are related to the low energy elastic scattering matrix elements as follows

$$\left\langle N \left| \bar{\psi}_q \psi_q \right| N \right\rangle = \frac{m_N}{m_q} \cdot f_N^{Sq} \qquad (\text{for } u,\, d,\, s)\,, \tag{3.5}$$

$$\left\langle N \left| \bar{\psi}_q \psi_q \right| N \right\rangle = \frac{2}{27} \frac{m_N}{m_q} \cdot f_N^{SG} \quad (\text{for } c,\, b,\, t)\,. \tag{3.6}$$

$f_N^{S\,q/G}$ are typically extracted from data or from chiral perturbation theory [147] and depend on the type of current which defines the DM-nucleon interaction. For a scalar current, the default $f_N^{S\,q}$ values for light quarks used in MADDM are:

$$\begin{aligned} f_p^{Su} &= 0.0153, \qquad f_n^{Su} = 0.0110, \\ f_p^{Sd} &= 0.0191, \qquad f_n^{Sd} = 0.0273, \\ f_p^{Ss} &= 0.0447, \qquad f_n^{Ss} = 0.0447, \end{aligned} \tag{3.7}$$

while f_N^{SG} is given by

$$f_N^{SG} = 1 - \sum_{q=u,d,s} f_N^{Sq}\,. \tag{3.8}$$

The interpretation for a **vector current** interaction is simpler. Since the vector current is conserved, the DM-nucleon form factor can be obtained from the sum of the currents of the valence quarks, *i.e.*:

$$f_N^V = \sum_{q=u,d} f_N^{Vq} \cdot \alpha_q\,, \tag{3.9}$$

where $f_p^{Vu} = f_n^{Vd} = 2$ and $f_p^{Vd} = f_n^{Vu} = 1$.

For spin-dependent interactions, the following equation defines the proton/neutron form factors $f_N^{'}$ in Eq. (3.2):

$$f_N^{'} = \sum_{q=u,d,s} \alpha_q\, \Delta_N^q\,. \tag{3.10}$$

This equation applies for both **axial-vector** and **tensor currents**. In MADDM, we use the following Δ_N^q default values for the axial-vector interaction:

$$\begin{aligned} \Delta_p^{AVu} &= \Delta_n^{AVd} &&= 0.842, \\ \Delta_p^{AVd} &= \Delta_n^{AVu} &&= -0.427, \\ \Delta_p^{AVs} &= \Delta_n^{AVs} &&= -0.085, \end{aligned} \tag{3.11}$$

while we use another set of coefficients for the tensor interaction:

$$\begin{aligned} \Delta_p^{Tu} &= \Delta_n^{Td} = 0.84, \\ \Delta_p^{Td} &= \Delta_n^{Tu} = -0.23, \\ \Delta_p^{Ts} &= \Delta_n^{Ts} = -0.046. \end{aligned} \tag{3.12}$$

Δ_p^{AVu} and Δ_p^{AVd} have been provided by HERMES and COMPASS experiments [148, 149] while tensor coefficients come from lattice calculations [150].

The coefficients α_q can be extracted from the full matrix elements for χq scattering via Fiertz transformations. While this is relatively straightforward to do analytically, numerical implementations of Fiertz transformations are non-trivial. In the following section, we discuss the numerical method MADDM uses to compute the low energy coefficients α_q from the full matrix elements in the χq scattering.

3.1.2 Projection operator method for extraction of low energy coefficients

The procedure for computing the low energy coefficients for DM-nucleon scattering in MADDM is similar to the procedure implemented in MICROMEGAS [145] [1]. At the quark level, the input quark-DM interacting Lagrangian at low energy can be rewritten as a set of effective operators as follows:

$$\mathcal{L}_{Q^2=0} = \sum_i \alpha_i \, \mathcal{O}_q^i \,, \tag{3.13}$$

where the operators $\mathcal{O}_q$ standing for χq scattering are defined in Table 3.1, and the index i runs over all the relevant contributions. The list of operators can be separated in odd and even operators under the interchange of quarks and anti-quarks as follows:

$$\begin{aligned} \mathcal{L}_{Q^2=0} &= (\mathcal{L}_{SI}^e + \mathcal{L}_{SI}^o) + (\mathcal{L}_{SD}^e + \mathcal{L}_{SD}^o) \\ &= \sum_{q,s} \alpha_{q,s}^{SI} \mathcal{O}_{q,s}^{SI} + \sum_{q,s} \alpha_{q,s}^{SD} \mathcal{O}_{q,s}^{SD}, \end{aligned} \tag{3.14}$$

where $q = u, d, s, c, b, t$ and s stands for even (e) or odd (o) operator. The Fiertz transformation which gives $\alpha_{q,s}$ coefficients projects the matrix element for $\chi q \to \chi q$ onto the set of effective operators. Numerically, this is equivalent to take the interference term of the matrix element for $\chi q \to \chi q$ scattering with the even effective operator

[1] For improved treatments on QCD effect in DM scattering off nucleon, see Ref. [151] and Ref. [152] for recent development.

	DM spin	Even	Odd
SI		scalar current	vector current
	0	$2M_\chi S S^* \bar{\psi}_q \psi_q$	$i\left(\partial_\mu S\, S^* - S\partial_\mu S^*\right)\bar{\psi}_q\gamma^\mu\psi_q$
	1/2	$\bar{\psi}_\chi\psi_\chi\bar{\psi}_q\psi_q$	$\bar{\psi}_\chi\gamma_\mu\psi_\chi\bar{\psi}_q\gamma^\mu\psi_q$
	1	$2M_\chi A^*_{\chi\mu}A^\mu_\chi\bar{\psi}_q\psi_q$	$i\left(A^{*\alpha}_\chi\partial_\mu A_{\chi\alpha} - A^\alpha_\chi\partial_\mu A^*_{\chi\alpha}\right)\bar{\psi}_q\gamma_\mu\psi_q$
SD		axial-vector current	tensor current
	1/2	$\bar{\psi}_\chi\gamma^\mu\gamma^5\psi_\chi\bar{\psi}_q\gamma_\mu\gamma_5\psi_q$	$-\frac{1}{2}\bar{\psi}_\chi\sigma_{\mu\nu}\psi_\chi\bar{\psi}_q\sigma^{\mu\nu}\psi_q$
	1	$\sqrt{6}\left(\partial_\alpha A^*_{\chi\beta}A_{\chi\nu} - A^*_{\chi\beta}\partial_\alpha A_{\chi\nu}\right)\epsilon^{\alpha\beta\nu\mu}\bar{\psi}_q\gamma_5\gamma_\mu\psi_q$	$i\frac{\sqrt{3}}{2}\left(A_{\chi\mu}A^*_{\chi\nu} - A^*_{\chi\mu}A_{\chi\nu}\right)\bar{\psi}_q\sigma^{\mu\nu}\bar{\psi}_q$

Table 3.1: List of effective operators taken from Ref. [145], implemented into MADDM. S, ψ_χ and A_χ correspond to scalar, fermion and vector DM fields, respectively.

matrix element for the same process. The projection over the effective operators will select either SI or SD contributions since Eq. (3.13) is written in an orthogonal basis.

The even and odd coefficients can be further separated by considering scattering off of both quarks and anti-quarks. The sum and difference of the even and odd coefficients can be written as:

$$\alpha_{q,e} + \alpha_{q,o} = \frac{|\mathcal{M}^{q*}\cdot\mathcal{M}^{q,e}_{\rm eff}|}{|\mathcal{M}^{q,e}_{\rm eff}|^2}, \tag{3.15}$$

$$\alpha_{q,e} - \alpha_{q,o} = \frac{\left|\mathcal{M}^{\bar{q}*}\cdot\mathcal{M}^{\bar{q},e}_{\rm eff}\right|}{\left|\mathcal{M}^{\bar{q},e}_{\rm eff}\right|^2}, \tag{3.16}$$

where the $|\mathcal{M}^{q,e}_{\rm eff}|^2$ in the denominator takes into account the fact that the effective operators are not properly normalized. In Eq. (3.16) we used the property that the odd coefficient changes sign under the interchange of $q \to \bar{q}$. Note that the procedure of projection operators for extracting $\alpha_{q,s}$ is completely generic although the list of effective operators is non-exhaustive. Indeed, operators such as $\bar{\psi}\gamma_5\psi$ are neglected since they are suppressed in the zero momentum limit.

3.1.3 Differential nucleus recoil rate

The direct detection module of MADDM allows the user to calculate quantities relevant for DM-nucleus scattering beyond the spin-independent and spin-dependent cross section. One is, for instance, often interested in studies of nucleus recoil rates, where traditionally the quantity of interest has been dR/dE, the differential nuclear recoil rate as a function of recoil energy. However, valuable information is contained in the angular distribution of the recoil rate $dR/d\Omega$. And despite the fact that no currently

operating experiment has the ability to efficiently measure directionality of the nuclear recoil with high statistics, there are few ongoing efforts in this direction as well as concrete proposals for future experiments [131, 134, 153–156]. Hence, we deemed it important to include the ability to calculate the angular rates into the MADDM code.

One reason why angular information could be important is that low energy recoil events recorded by direct detection experiments lie well within the range dominated by cosmogenic backgrounds and those resulting from radioactivity. A strong signature of DM may come from directional detection, which exhibits a very large forward-backward asymmetry (A_{FB}) in the angular distribution of nuclear recoil events. A large A_{FB} would be difficult to mimic with any known backgrounds as one expects the angular distribution of such processes to be roughly uniform.

The fact that background processes are (typically) spatially isotropic could be used to overcome another impeding problem. As the direct detection bounds on the DM-nucleon cross sections get lower, neutrino backgrounds will present an obstacle [157] and directional detection could provide a way to circumvent the so called "neutrino floor" [158].

In case a signal is ever observed, the study of directionality in DM-nucleus recoils will be of foremost interest. The angular distribution of the recoil rates could provide useful information about the astrophysical aspects of the DM galactic halo profile [132, 159], as well as information on the anisotropy in the DM halo velocity distribution and prospects for more accurate measurements of the DM mass and interaction cross section [131].

We begin by considering our solar system moving through the Galactic "DM-wind" in the direction of the Cygnus $X-2$ constellation as illustrated in Fig. 3.1. A DM particle of mass m_χ, incident at velocity $\mathbf{v} = v(\sin\alpha\cos\beta\,\hat{\mathbf{x}} + \sin\alpha\sin\beta\,\hat{\mathbf{y}} + \cos\alpha\,\hat{\mathbf{z}})$ in the detector, elastically scatters off a target nucleus of mass m_N, stationary in the detector, and causes it to recoil with velocity $\mathbf{u} = u(\sin\theta\cos\phi\,\hat{\mathbf{x}} + \sin\theta\sin\phi\,\hat{\mathbf{y}} + \cos\theta\,\hat{\mathbf{z}})$ and momentum $\mathbf{q}$ in the direction (θ, ϕ). The event rate per unit recoil energy and unit recoil solid angle is

$$\frac{d^2R}{dE_R d\Omega_{(\theta,\,\phi)}} = \frac{2\,\rho_0}{m_\chi}\int \frac{d\sigma}{dq^2 d\Omega_{(\theta,\,\phi)}} v f(\mathbf{v}) d^3v, \tag{3.17}$$

where ρ_0 is the DM density in our local galaxy and $f(\mathbf{v})$ is the velocity distribution of the DM in the galactic halo. The differential cross section

$$\frac{d\sigma}{dq^2 d\Omega_{(\theta,\phi)}} = \frac{\sigma_{\chi N}}{8\pi\mu^2 v} F^2(q)\delta\big(v\cos\theta - \frac{q}{2\mu}\big), \tag{3.18}$$

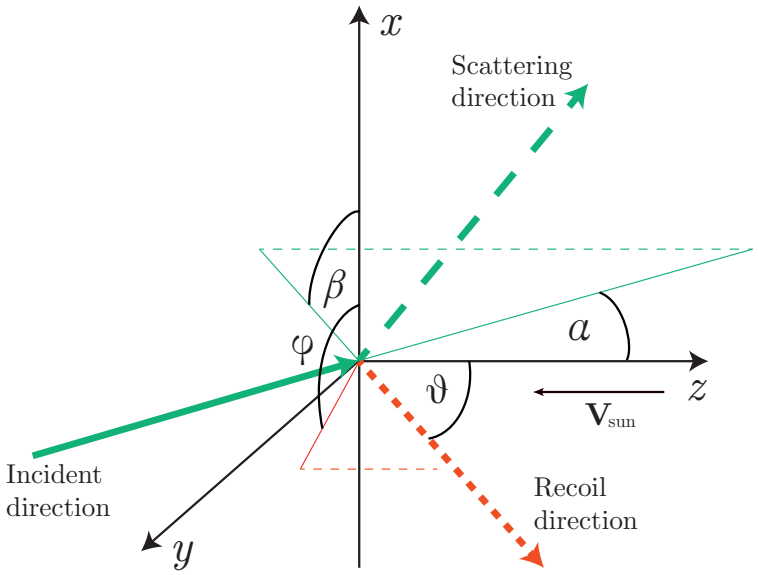


Figure 3.1: Geometry of DM scattering off a target nucleus in the detector. The DM is incident at an angle (α, β) relative to the **z** axis. The nucleus recoils in the (θ, ϕ) direction. Note that β and ϕ angles lie in the x, y plane. The thin and dashed thin lines serve to illustrate the projection of the incoming and recoil vectors onto the z axis and the xy plane.

is obtained from the two body scattering phase space distribution [133]. Here, $\mu = m_\chi m_N/(m_\chi + m_N)$ is the reduced mass of the DM-nucleus system, $q = \sqrt{2\, m_N\, E_R}$ is the recoil momentum with E_R the recoil energy, θ is the recoil angle which determines the direction between the recoiling nucleus and the initial DM trajectory, while $\sigma_{\chi N}$ is the DM-nucleus scattering cross section, weighted by the nuclear elastic scattering form factor $F(q)$. Assuming the nucleus is a sphere with uniform density, the form-factor is the Fourier transform of the nuclear density and includes all the relevant nuclear effects. For example, we consider the Helm form factor as described in Ref. [160] for the spin-independent case. The DM-nucleus cross section is summed over contributions from the spin-independent (σ_{SI}) and spin-dependent (σ_{SD}) cross sections respectively, as defined in Eq. (3.1) and Eq. (3.2) respectively. Eq. (3.17) becomes

$$\frac{d^2 R}{dE d\Omega_{(\theta,\phi)}} = \frac{N_0\, \rho_0\, \sigma_{\chi N}}{\pi\, A\, r\, m_\chi^2} F^2(q) \int \delta(v\cos\theta - \frac{q}{2\mu}) f(\mathbf{v}) d^3 v, \tag{3.19}$$

where $r = 4m_N m_\chi/(m_N + m_\chi)^2$, $N_0 = 6.022 \times 10^{26}\ \mathrm{kg}^{-1}$ is Avogadro's number, $m_N = 0.932$ A is the target mass and A the atomic mass number (the factor of 0.932 is the value of atomic mass units (AMU) in GeV). We assume a Maxwell-Boltzmann velocity distribution truncated at the DM escape velocity.

Finally we use Eq. (3.19) to simulate the scattering of DM with the nucleus in a detector. We take into account the energy and angular resolutions of a generic detector as applied to the distribution of the scattering events. We assume a Gaussian resolution function to smear the distribution of recoil events in both energy and angle with standard deviations $\sigma_E = \lambda\sqrt{E}$ (the energy resolution) and σ_θ (constant angular resolution) as in Ref. [131]. Default resolutions are given by $\lambda = 1$ and $\sigma_\theta = 30^\circ$ with an option for users to implement their own detector resolutions.

3.2 Validation

We performed validations of the MADDM code in a diverse class of benchmark models. In each case, we verified that the code reproduces accurately the results from existing literature or public codes such as MICROMEGAS.

3.2.1 Validation of the DM-nucleon cross section calculation

Simplified DM Models

The simplest benchmark model we consider for validation is a scalar DM which communicates to the SM via the Higgs boson. The model contains only one diagram contributing to direct detection *i.e.* a t-channel Higgs exchange. The Higgs-DM coupling is included in the $\frac{\delta}{2}|H|^2 S^2$ operator where S is the DM scalar field. It implies that the model leads only to spin-independent cross section.

For the purpose of validating calculations of the spin-dependent cross sections, we consider a similar simplified model, with an axial-vector mediator which couples through fermionic DM and SM via the following Lagrangian:

$$\mathcal{L}_A = g_\chi^A\, \bar{\chi}\gamma_\mu\gamma_5\chi Y_1^\mu + g_q^A\, \bar{q}\gamma_\mu\gamma_5 q Y_1^\mu\,, \tag{3.20}$$

where χ and Y_1 are the DM and mediator fields, respectively. Figure 3.2 shows our results for proton/neutron DM cross section for the two simplified models against results obtained with MICROMEGAS. In both cases, we find an excellent agreement between MADDM and MICROMEGAS with the differences at $\lesssim 1\%$ level. We have

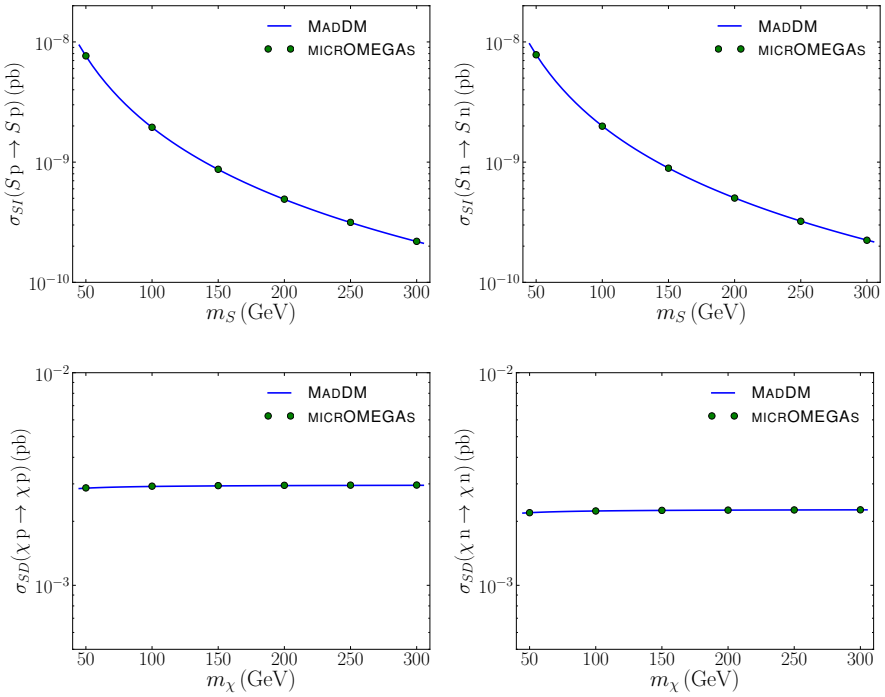


Figure 3.2: Spin-independent elastic scattering cross section of scalar DM in the simplified SM model scenario with proton and neutron for $\delta = 0.1$ (top panel). Spin-dependent elastic scattering cross section of Dirac fermion DM with proton and neutron for $g_\chi^A = 0.1$ (lower panel).

also checked that the results from MadDM are consistent with micrOMEGAs in case of simplified models with different mediators (scalar, fermion and vector) and different DM candidates (scalar, fermion and vector).

Minimal Universal Extra Dimensions

After validating MadDM for a class of simplified models, we turn to more complex models. For this purpose, we chose to examine the results of MadDM for the Minimal Universal Extra Dimension model (MUED) against the results in existing literature.

MUED is the simplest model containing a Kaluza-Klein (KK) DM candidate among extra dimensions theories. The lightest KK particle, the KK-photon (γ_1) appears as a DM candidate in vanilla UED scenarios. At tree level, the inverse radius R^{-1} of the

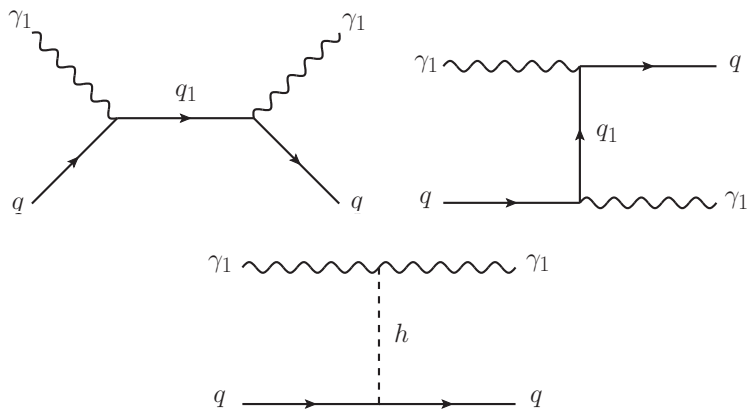


Figure 3.3: Feynman diagrams for elastic scattering of KK photon with a quark.

extra-dimension corresponds roughly to the mass of the massive fields at level one. The mass splitting between KK-quark (q_1) and KK-photon,

$$\Delta = \frac{m_{q_1} - m_{\gamma_1}}{m_{\gamma_1}}\,, \tag{3.21}$$

plays an important role as a free parameter in direct detection. The details and phenomenology of MUED will not be discussed here since it has been studied extensively in the past [161–164] and we will proceed directly to the comparison of MADDM results on direct detection to the results in literature.

The diagrams contributing to DM-nucleon cross section are displayed in Fig. 3.3. The Higgs-exchange diagram contributes to SI DM-nucleon cross section while the other two diagrams involving KK quarks contribute both for SI and SD DM-nucleon cross sections. We compared the MADDM results against those using the private code used in Refs. [161, 164]. The results, shown in Fig. 3.4, show perfect agreement between MADDM and the private code over a wide range of DM masses and for several values of Δ. The DM-neutron cross sections are also in excellent agreement.

Minimal Supersymmetric Standard Model

Finally, we also validated MADDM for SPS1a benchmark point in Minimal Supersymmetric Standard Model (MSSM) [165]. MSSM neutralino DM is similar to KK photon DM in that the processes relevant for direct detection typically proceed via

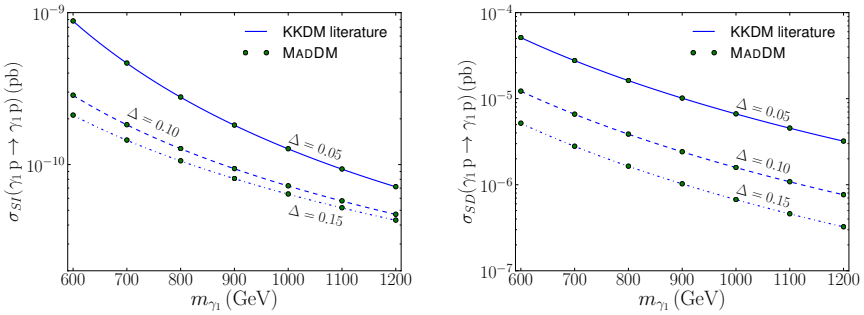


Figure 3.4: Spin-independent (left panel) and spin-dependent (right panel) DM-proton cross section for MUED. The blue curves correspond to theoretical values coming from Kaluza-Klein DM literature [163, 164]. The green points are the MadDM data. We show the results for three values of the Δ parameter.

squark exchange in the s- and u-channels and Higgs exchange in the t-channel (see Fig. 3.3). We compare MADDM with MICROMEGAS for DM-nucleon cross section for several SPS points. The ratio of the two tools cross sections indicates that MADDM agrees with MICROMEGAS to $\sim 1\%$ level, with the exception of the SPS5 point. We have checked that the statement is also true if we vary the neutralino mass around the SPS1a point ($m_{\tilde{\chi}_1^0} = 96.68\,\mathrm{GeV}$).

3.2.2 Recoil rates

Upon validating the DM-nucleon scattering cross section results from MADDM, we proceed to the recoil rates for DM scattering off a target nucleus. As an example, we play with a simple, model independent validation of the recoil rate calculation, where we simply assume that the DM-nucleon cross section $\sigma_{\chi n} = 10^{-9}$ pb, chosen for the purpose of comparison with the results from Ref. [139]. To reproduce the SI recoil rates as a function of energy/angle as in Ref. [139], we employ the differential recoil spectrum of Eq. (3.19), integrated over time and angle/energy. Figure 3.5 shows the spin-independent recoil rates as a function of recoil energy (top panel) and recoil angle (lower panel). We find that both distributions are in a very good agreement with the results found in Ref. [139], over a wide range of target materials. For other complete examples of validations of the recoil rates in MADDM, see the original paper [3].

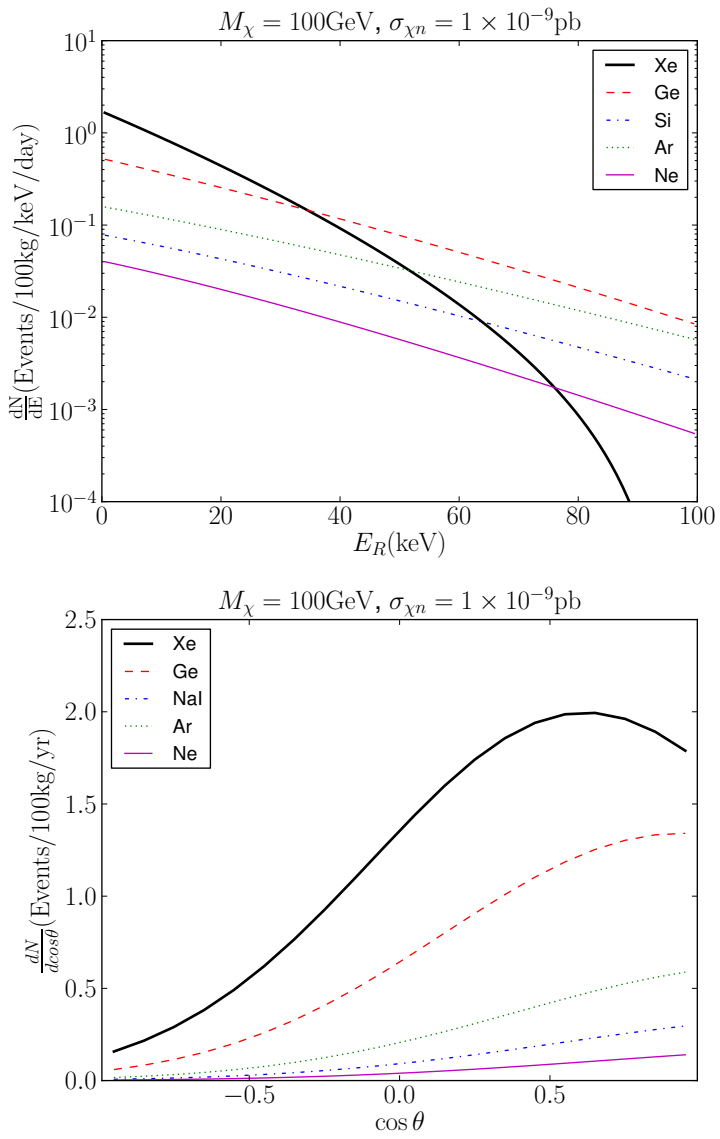


Figure 3.5: Nuclear recoil energy (top panel) and angular (lower panel) distributions for spin-independent interactions for different materials, assuming a 100 kg detector measuring events over one year for a DM mass of 100 GeV and DM-nucleon cross section of 1×10^{-9} pb.

3.3 Summary and outlook

In order to efficiently combine results from various DM searches sparked a demand for a new generation of numerical tools. MADDM is an on-going effort to bridge DM collider phenomenology with astrophysics and cosmology of DM, with the ultimate goal to provide an "all in one" DM phenomenology package which can be easily incorporated into the future DM searches at the LHC.

In this chapter, we presented MADDM v2.0, which includes direct detection of DM in a generic UFO model. The code computes the total DM-nucleus scattering rate, recoil energy spectrum and angular distributions of DM elastic scattering off nuclei for various target materials, including user-provided detector resolution and detector efficiency. MADDM v2.0 follows the "easy to use, easy to install" philosophy of the previous version, featuring great flexibility so that users can replace the existing modules with their own implementation or link MADDM functionality with other existing tools. We have performed a detailed validation of MADDM against MICROMEGAS and private codes for various benchmark DM models and found excellent agreements with existing tools and literature.

We believe that the direct detection module we developed will help people to easily set constraints on their DM models. On the other hand, experimentalists could also use MADDM v2.0 to set direct detection constraints on their simplified models interpretation of the results as they did it for relic abundance with MADDM v1.0 (*e.g.* in Ref. [166]). In the future, the direct detection module of MADDM should be updated to handle twist-2 operators. For example, such operators appear in DM models with a spin-2 mediator and the direct detection module of MADDM is not currently able to deal with them. The future implementation of twist-2 operators will be based on Ref. [151].

In addition to relic abundance and direct detection, the future renditions of the code will also provide ability to calculate cosmic-ray fluxes from DM annihilation, including gamma rays, cosmic electrons/positrons and protons/anti-protons. The code will be linked to DRAGON which simulates the propagation of charged particles in the Galaxy [43]. Furthermore, the MG5_AMC framework allows for computations of amplitudes for loop induced diagrams [78], giving us an opportunity to create the first automated DM tool which can calculate relic density, direct detection and indirect-detection signals originating in loop-induced processes.

The next version of MADDM will also be fully integrated in the MG5_AMC tool, taking advantage of the whole MG5_AMC machinery *i.e.* the possibility to compute automatically mediator width and to use the built-in MG5_AMC commands to scan

over a wide range of model parameters. These new features are already available as beta version on the MADDM launchpad webpage [167].

Chapter 4

Exploration of simplified top-philic dark matter model

"The value of achievement lies in the achieving."

Albert Einstein (1879 - 1955)

In this chapter we illustrate how comprehensive studies of simplified DM models can be performed, exploring their full four-dimensional parameter space while taking into account constraints from collider physics, astroparticle physics and cosmology. For concreteness, we focus on a class of simplified models where the DM dominantly couples via a scalar mediator to top quarks (*i.e.* 'top-philic DM' scenarios). Yet, the methodology we employ is general and can be applied to other scenarios as well. We provide detailed examinations of the two-dimensional projections of the full parameter space, and we demonstrate that striking features in the structure of the viable parameter space emerge through the combination of all current constraints. We also stress that in addition to collider searches for DM in channels with large missing energy, in this study we also consider resonance searches in channels with fully reconstructed final states, which can be useful to constrain the properties of the mediators.

We perform the study of simplified top-philic DM models by using a combination of simulation tools, including the MG5_aMC event generator [78], the FeynRules package [77, 88], the Delphes 3 detector simulator [168], the MadDM program [3, 129] and the MadAnalysis 5 platform [169–171], together with an efficient parameter sampling technology based on the MultiNest algorithm [172, 173]. We explore

the full four-dimensional parameter space of the model in the light of existing collider and astroparticle constraints. Our analysis also represents a proof of concept for a unified numerical framework for comprehensive DM studies at the interface of collider physics, astrophysics and cosmology. This has direct implications for DM searches at colliders, as comprehensive phenomenological studies of DM models can be used to drive the experimental efforts towards the regions of the parameter space that are not already ruled out by astrophysical and cosmological constraints. In addition, we have also implemented previously unavailable experimental analyses into the MADANALYSIS 5 platform, providing an added benefit of our work for future collider studies which go beyond searches for DM.

This chapter is organised as follows. Section 4.1 describes the details of the simplified top-philic DM model under consideration and discusses the constraints on the model parameter space that are implemented in our analysis setup. All cosmology and astrophysics constraints are discussed in section 4.2. Collider constraints from searches with and without missing transverse energy are investigated in section 4.3. Finally we combine and discuss cosmological, astrophysical and collider constraints in section 4.4. We provide more information on the mediator width in appendix B and present the validation of the CMS $t\bar{t} + \not{E}_T$ and monojet implementation in the MADANALYSIS 5 framework in appendix C.

4.1 Simplified top-philic dark matter model and its numerical implementation

The simplified top-philic DM model that we consider is constructed by supplementing the SM with a Dirac-type fermionic DM candidate X and a scalar mediator Y_0. This model corresponds to a restriction of the general DMSIMP model studied in Chapter 2. The interactions of the two particles are described by the Lagrangian

$$\mathcal{L}_{t,X}^{Y_0} = -\Big(g_t \, \frac{y_t}{\sqrt{2}} \, \bar{t}t + g_X \, \bar{X}X\Big) Y_0 \,, \tag{4.1}$$

where the new physics interaction strengths are denoted by g_t and g_X for the mediator couplings to the SM sector and to DM respectively. We have assumed a minimally flavour-violating [174] scalar theory where the mediator couples to quarks with a strength proportional to the SM Yukawa couplings, so that we neglect all light quark flavour couplings and only include the coupling of the mediator to the top quark, $y_t = \sqrt{2} m_t / v$ where $v = 246$ GeV is the Higgs vacuum expectation value and m_t is the top quark mass. According to the spirit of simplified models, the above Lagrangian is not invariant under the SM gauge group. In ultraviolet completions where Y_0 is one of the components of an $SU(2)_L$ doublet, as in the Two-Higgs-Doublet Model, our

simplified model corresponds to scenarios with a high degree of alignment. In this case, the couplings of the gauge bosons to the heavier CP-even scalar are suppressed, *e.g.* $\cos(\beta-\alpha)\sim 0$ where $\tan\beta$ consists of the ratio of the vacuum expectation values of the neutral components of the two Higgs doublets and α is the CP-even Higgs mixing angle (see *e.g.* [175, 176]). Such setups are in particular common in minimal supersymmetric realisations. In contrast, if the mediator is a gauge singlet, it should mix with the Higgs sector, leading to a more complex phenomenology as in the so-called Higgs portal DM models (see *e.g.* the works of Refs. [177–182]).

The model contains four free parameters (two couplings and two masses),

$$\{g_t,\, g_X,\, m_X,\, m_Y\}\,, \tag{4.2}$$

while the width Γ_Y is fixed by the remaining model parameters. In addition to the Lagrangian of Eq. (4.1), we could also have considered mediator couplings to leptons. They however cannot be well constrained by LHC searches and DM direct detection data, and we have excluded them from our model description.

The Lagrangian of Eq. (4.1) induces dimension-five couplings of the mediator to gluons and photons via loop diagrams of top quarks. The loop-induced operators can be relevant in the context of both astrophysical and collider searches for DM. The couplings of the mediator to gluons and photons are given, at the leading order (LO), by the effective operators

$$\mathcal{L}_g^{Y_0} = -\frac{1}{4}\frac{g_g(Q^2)}{v}\,G^a_{\mu\nu}G^{a,\mu\nu}Y_0 \qquad \text{and} \qquad \mathcal{L}_\gamma^{Y_0} = -\frac{1}{4}\frac{g_\gamma(Q^2)}{v}\,F_{\mu\nu}F^{\mu\nu}Y_0\,, \tag{4.3}$$

with the effective couplings being

$$g_g(Q^2) = g_t\frac{\alpha_s}{3\pi}\,\frac{3}{2}F_S\Big(\frac{4m_t^2}{Q^2}\Big) \qquad \text{and} \qquad g_\gamma(Q^2) = g_t\frac{8\alpha_e}{9\pi}\,\frac{3}{2}F_S\Big(\frac{4m_t^2}{Q^2}\Big)\,. \tag{4.4}$$

In the above expressions, Q^2 denotes the virtuality of the s-channel resonance, while F_S is the one-loop form factor

$$F_S(x) = x\Big[1+(1-x)\arctan^2\Big(\frac{1}{\sqrt{x-1}}\Big)\Big]\,, \tag{4.5}$$

with $F_S(x)\to 2/3$ for $x\gg 1$. Eq. (4.4) contrasts with the SM Higgs case where the effective Higgs-photon coupling receives contributions from vector-boson loop-diagrams that are absent in our simplified DM model setup. As a result, the gluon and photon effective couplings to Y_0 are characterised by a larger hierarchy compared to their Higgs counterparts.

The tree-level partial decay widths of the scalar mediator are given by

$$\Gamma(Y_0 \to t\bar{t}) = g_t^2 \frac{3y_t^2 m_Y}{16\pi} \beta_t^3 \, \Theta(m_Y - 2m_t)\,, \tag{4.6}$$

$$\Gamma(Y_0 \to X\bar{X}) = g_X^2 \frac{m_Y}{8\pi} \beta_X^3 \, \Theta(m_Y - 2m_X)\,, \tag{4.7}$$

where $\beta_{t,X} = \sqrt{1 - 4m_{t,X}^2/m_Y^2}$ and $\Theta(x)$ is the Heaviside step function, and we ignored the top quark width in the expression for $\Gamma(Y_0 \to t\bar{t})$. The loop-induced Y_0 partial widths are

$$\Gamma(Y_0 \to gg) = g_t^2 \frac{\alpha_s^2 m_Y^3}{72\pi^3 v^2} \left| \frac{3}{2} F_S\Big(\frac{4m_t^2}{m_Y^2}\Big) \right|^2, \tag{4.8}$$

$$\Gamma(Y_0 \to \gamma\gamma) = g_t^2 \frac{\alpha_e^2 m_Y^3}{81\pi^3 v^2} \left| \frac{3}{2} F_S\Big(\frac{4m_t^2}{m_Y^2}\Big) \right|^2. \tag{4.9}$$

The Y_0 partial width to photons is by construction always smaller than the partial decay width into a pair of gluons by virtue of $\alpha_s^2/\alpha_e^2 \sim 100$. In addition to a coupling suppression, other decay processes such as the loop-induced Y_0 decays into $Z\gamma$, ZZ and hh final states receive a kinematic suppression. Indeed, we expect these channels to be irrelevant compared to the gg contribution. For example, the ZZ contribution in the limit of heavy mediator should be comparable to the photon one *i.e.* very small. Couplings of Y_0 to ZZ and hh could also appear at tree level in our model, but in the spirit of simplified models, we define them to be vanishing. In the following we hence safely approximate the total decay width for the mediator to be the sum of Eqs. (4.6), (4.7) and (4.8).

The total decay width and the branching ratios of the mediator into $t\bar{t}, X\bar{X}, gg$ and $\gamma\gamma$ final states are displayed in Fig. 4.1 for different choices of new physics couplings and masses. Light mediators with masses below the top-quark pair or the DM pair decay thresholds are narrow states, while above these thresholds, large Γ_Y/m_Y values are possible in particular for large couplings. For mediators with $m_Y \lesssim m_t, m_X$, the dominant decay channel is into a pair of gluons. In contrast, heavy mediators with mass $m_Y > m_t, m_X$ decay predominantly into pairs of top quarks and/or DM particles, where the exact details of the partial width values strongly depend on the masses and couplings. The branching ratio of Y_0 to photons is always suppressed, as argued above. We present in appendix B the dependence of the Γ_Y/m_Y ratio on the g_t and g_X couplings for different mass choices and on the m_Y and m_X masses for different coupling choices.

Our top-philic DM model can be probed in different ways including astrophysical and collider searches, as listed in table 4.1. The relative importance of the various searches

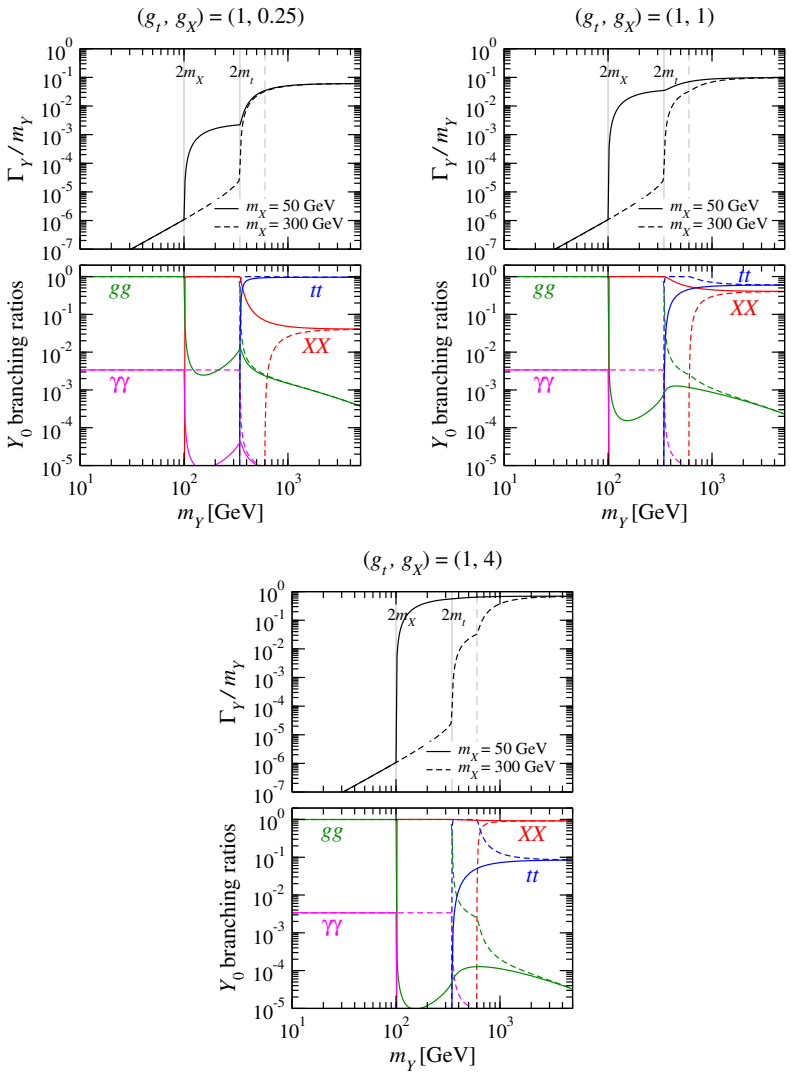


Figure 4.1: Ratio of the mediator width to its mass Γ_Y/m_Y (upper panels) and mediator branching ratios (lower panels) as a function of the mediator mass for different coupling choices and a DM mass fixed to $m_X = 50$ GeV (solid lines) and 300 GeV (dashed lines).

depends on the hierarchy of the DM, mediator and top-quark masses, as well as on the hierarchy between the couplings. Starting with the DM relic density, the annihilation cross section is dominated by subprocesses with top-quark final states for $m_X > m_t$,

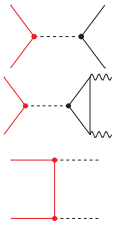
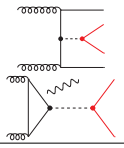
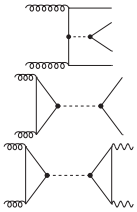
Cosmology Astrophysics	relic indirect		$m_X > m_t$ $m_X < m_t$ $m_X > m_Y$	Planck, FermiLAT
	direct		$m_X > 1$ GeV	LUX, CDMSLite
Colliders	$\not{E}_T$		$m_Y > 2m_X$ $m_Y > 2m_X$	$+t\bar{t}$ $+j, +Z, +h$
	no $\not{E}_T$		$m_Y > 2m_t$ $m_Y > 2m_t$ $m_Y < 2m_X, 2m_t$	$4t$ $t\bar{t}$ $jj, \gamma\gamma$

Table 4.1: Signatures of our simplified top-philic dark matter model.

and by annihilation into gluons and to a lesser extent photons for light DM particles with $m_X < m_t$. If the mediator is lighter than the DM state, an additional annihilation channel into a pair of mediators can open up. The annihilation mechanisms into top-quarks, gluons/photons and mediators moreover provide an opportunity to indirectly search for DM, *e.g.* in gamma-ray data. The interactions of the DM particles with nuclei, relevant for direct detection experiments, proceed via mediator exchanges. The mediator-nucleon coupling is in turn dominated by the scattering off gluons through top-quark loops.

DM production at the LHC proceeds either through the production of the mediator in association with top quarks, or from gluon-fusion through top-quark loops. Searches at the LHC can be classified into two categories regarding the nature of the final states that can contain missing transverse energy $\not{E}_T$ or not. Searches involving missing energy may include final state systems containing a top-quark pair and probe in this way the associated production of a top-antitop-mediator system where the mediator subsequently decays into a pair of DM particles. Alternatively, the mediator can be produced via gluon fusion through top-quark loops, where the probe of the associated

	Observable	Value/Constraint	Comment
Measurement	$\Omega_{\rm DM}h^2$	0.1198 ± 0.0015	Planck 2015 [12]
Limits	Γ_Y/m_Y	< 0.2	Narrow width approximation
	Γ_Y	$> 10^{-11}$ GeV	Ensures prompt decay at colliders
	$\sigma_n^{\rm SI}$	$< \sigma_{\rm LUX}^{\rm SI}$ (90% CL)	LUX bound [142] ($m_X > 8$ GeV)
	$\sigma_n^{\rm SI}$	$< \sigma_{\rm CDMS}^{\rm SI}$ (95% CL)	CDMSlite bound [58] ($1\,\text{GeV} < m_X < 8\,\text{GeV}$)

Table 4.2: Summary of the observables and constraints used in this analysis.

events consists of tagging an extra radiated object. This yields the well-known mono-jet, mono-Z and mono-Higgs signatures. We do not consider the monophoton channel, as photon emission is forbidden at LO in our simplified model by means of charge conjugation invariance. The second search category is related to final states without any missing energy, *i.e.* when the mediator decays back into SM particles. This includes decays into top-quarks, leading to final states comprised of four top quarks, into a top-quark pair, as well as into a dijet or a diphoton system via a loop-induced decay. This is, however, relevant only for on-shell (or close to on-shell) mediator production.

We proceed with a description of the numerical setup for our calculations. In the following sections, we explore the full four-dimensional model parameter space and present results in terms of two-dimensional projections. We perform the sampling using the MULTINEST algorithm [172,173]. We have chosen to limit the coupling values to a maximum of π to ensure perturbativity. Table 4.2 summarises the constraints that we have imposed on the model parameter space.

Throughout our study, we assume that X is the dominant DM component, namely that it fully accommodates a relic density $\Omega_{\rm DM}h^2$ as measured by the Planck satellite [12]. Concerning the direct detection of DM, we consider the currently most stringent bounds on the spin-independent (SI) nucleon-DM cross section as measured by LUX for DM with $m_X > 8$ GeV [142] and by CDMSLite for 1 GeV$< m_X < 8$ GeV [58]. For the purpose of the relic density and direct detection cross section calculations, we utilise MADDM [3, 129] (see chapter 3).

We derive collider constraints on our model using the MG5_AMC [78] framework and the recast functionalities of MADANALYSIS 5 [169–171] (where appropriate). We apply the LHC constraints on the top-philic DM model with two different procedures. On one side, we reprocess the scenarios that accomodate the observed relic density and that are compatible with LUX and CDMSLite data. However, we also study the collider bounds on the parameter space independently of any astrophysics and cosmology consideration and by relaxing the narrow width requirement (allowing Γ_Y/m_Y to be of $\mathcal{O}(1)$) as well. In order to increase the sensitivity of the LHC searches, we

allow for wider coupling ranges of $10^{-2} < g_X < 2\pi$ and $10^{-2} < g_t < 2\pi$. The collider study without any cosmological and astrophysical constraint therefore includes the cases where the DM is not a standard thermal relic (*i.e.* its relic density is a result of a non-thermal mechanism or a non-standard evolution of the Universe). Details are provided in section 4.3 and appendix C for what concerns the validation of the CMS analyses that we have implemented in MADANALYSIS 5 for this work.

4.2 Cosmological and astrophysical constraints

We begin our analysis of the simplified top-philic DM model with a detailed discussion of the cosmological and astrophysical constraints.

Concerning indirect detection, top-philic DM annihilation in the present Universe could result in fluxes of cosmic rays and prompt gamma-rays, which can be used to infer useful limits on the model parameter space. The annihilation of a $X\bar{X}$ pair in the galactic halo (or in dense environments of galactic centres) and the subsequent production of a secondary gamma ray flux is dictated by the same processes that set the relic abundance. Additionally, a direct coupling of the mediator to a pair of prompt photons is induced at higher order in perturbation theory via a loop of top quarks. Hence, the process $X\bar{X} \to \gamma\gamma$ exists and yields the production of two monochromatic photons that could be detected in searches for lines in the gamma-ray spectrum. Unfortunately, searches for gamma-ray signals of DM annihilation weakly constrain our simplified top-philic DM model. We have investigated results from gamma-ray line searches in the inner galactic region [183], as well as continuum gamma-ray measurements from dwarf spheroidal galaxies [184] and found no meaningful exclusion of the parameter space once the relic density and direct detection constraints are imposed. The lack of useful bounds is expected, as the annihilation of DM in the present Universe is p-wave suppressed. This contrasts with scenarios in which the mediator is a pseudoscalar state, where the gamma-ray constraints should be significantly stronger. Therefore we only focus on relic density and direct detection constraints in this section.

4.2.1 Constraints from dark matter relic density

DM annihilation in the early Universe is determined, in the simplified top-philic DM model, by a combination of three processes,

$$X\bar{X} \to t\bar{t} \quad (\mathrm{I})\,, \qquad X\bar{X} \to gg \quad (\mathrm{II})\,, \qquad \text{and} \qquad X\bar{X} \to Y_0 Y_0 \quad (\mathrm{III})\,,$$

where we have omitted the annihilation into photons as it is always suppressed compared to the annihilation into gluons. The first two processes proceed via an s-channel Y_0 exchange (first two rows of table 4.1), while the third process consists of a t-channel X exchange (third row of table 4.1). The resonance structure of the s-channel processes implies that the width of Y_0 potentially plays an important role in the determination of the relic density assuming a dominant annihilation via the processes (I) and (II), while the effects of the Y_0 width are mostly negligible if the annihilation dominantly proceeds via the t-channel X exchange process (III).

According to the hierarchy between the DM mass m_X, the mediator mass m_Y and the top quark mass m_t, different situations can occur. Qualitatively, one expects that:

- for $m_Y \gtrsim m_X \gtrsim m_t$: process (I) is dominant as the tree-level annihilation into a pair of top quarks is kinematically allowed, the annihilation into gluons being loop suppressed, and the one into a pair of mediators kinematically suppressed;
- for $m_X \lesssim m_t,\, m_Y$: DM annihilates into a pair of gluons as in process (II), since it is the only kinematically allowed channel;
- for $m_t \gtrsim m_X \gtrsim m_Y$: relic density is determined by process (III) since annihilation into top quarks is kinematically forbidden and the one into gluons occurs away from the resonant pole of m_Y;
- for $m_X > m_t, m_Y$ and $m_Y < 2m_t$: similarly to the case above, the dominant annihilation mechanism is process (III), as annihilation into top quarks occurs far from the resonant pole and is suppressed kinematically;
- for $m_X > m_t, m_Y$ and $m_Y > 2m_t$: processes (I) and (III) are competitive and the dominant process among the two is determined by the hierarchy between the g_t and g_X couplings.

Requiring our simplified top-philic DM model to result in a DM relic density consistent with the most recent Planck measurements [12] implies strong constraints on the viable regions of the parameter space. As an illustration, we consider the region of the parameter space in which $m_t \gtrsim m_X \gtrsim m_Y$, where we expect the dominant annihilation mechanism of DM to be process (III) and to give rise to a pair of mediators. In this region, the thermally averaged annihilation cross section approximately reads

$$\langle \sigma v_{\mathrm{rel}} \rangle_{\mathrm{ann}} \sim \frac{g_X^4}{m_X^2} \sim 10^{-9}\ \mathrm{GeV}^{-2}, \tag{4.10}$$

so that it is clear that imposing that the relic density predictions agree with Planck data leads to a stringent constraint on the ratio g_X^2/m_X. The argument is more involved in parameter space regions where the total mediator width Γ_Y plays a role, as the

relevant quantity involved in the relic density calculation is in general not $\langle\sigma v_{\rm rel}\rangle_{\rm ann}$ but $\int {\rm d}x \langle\sigma v_{\rm rel}\rangle_{\rm ann}(x)$ where $x \equiv m_X/T$ and $\langle\sigma v_{\rm rel}\rangle_{\rm ann}$ is a non trivial function of x. This is especially true, for instance, for the Breit-Wigner-type amplitudes that appear in processes (I) and (II).

In order to provide a more detailed quantitative analysis, we have performed a four-dimensional scan on the top-philic DM model parameter space and examined the effects of imposing relic density constraints on the allowed/ruled out parameter sets. Figures 4.2 and 4.3 reveal the rich structure of the four-dimensional parameter space allowed by relic density measurements. The bulk of the allowed parameter points lies in the region where $m_X > m_Y$, and the annihilation cross section is dominantly driven by process (III). This region of the parameter space has the particularity of not being reachable by traditional monojet, monophoton, mono-Z and mono-Higgs searches at colliders. The decay of the mediator into a pair of DM particles is indeed not kinematically allowed, so that any new physics signal will not contain a large amount of missing energy. The model can however be probed at colliders via dijet, diphoton, $t\bar{t}$ (plus jets) and four-top analyses. We elaborate on this point more in section 4.3.2. The characteristic mediator width Γ_Y in this region tends to be extremely small, with values of at most 10^{-4} GeV as shown in the top panel of Fig. 4.2. This is expected as the width is mostly controlled by the decays into gluons, and into top quarks in the regions where this decay is kinematically allowed, the decay into a pair of DM particles being forbidden.

In the region where $m_X \gtrsim m_t$ and $m_Y \gtrsim 2m_t$, the mediator decay into a $t\bar{t}$ final state is kinematically allowed and the DM annihilation cross section is driven by the $X\bar{X} \to Y_0 \to t\bar{t}$ process. The only other parameter space region that is not ruled out by the relic density data is centered around the resonance region where $m_Y \sim 2m_X$. The extension of the region away from the resonance pole is due to the Y_0 width that can reach $\mathcal{O}(10)$ GeV. The resonant region extends to lower m_X and m_Y values, and is the only allowed region when both m_X and m_Y are smaller than m_t (but with Y_0 decays into a pair of DM particles being allowed). This has interesting implications for LHC searches as the low DM/mediator mass region is the one where colliders have the best sensitivity, in particular through monojet searches (see for instance section 4.3.1).

Relic density constraints favour g_X couplings of $\mathcal{O}(1)$ in most of the scanned parameter range as evident in the top panel of Fig. 4.3, regardless of the actual value of the g_t coupling which is irrelevant in the $m_X \gtrsim m_Y$ region (lower panel of Fig. 4.3) as it does not enter the calculation of the relic density.

The structure of the ruled out parameter space regions shows several other interesting features. The most striking one is that almost the entire region where $m_Y \gtrsim 2m_X$

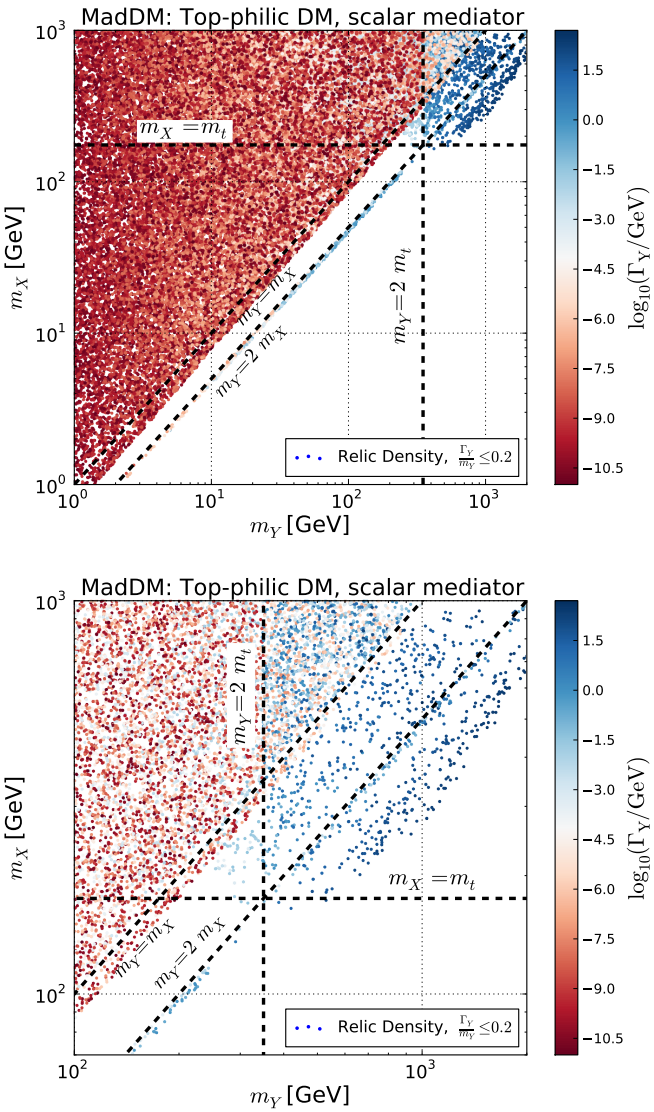


Figure 4.2: Results of our four-dimensional parameter scan using MADDM projected onto the (m_Y, m_X) plane. The top panel shows the projection with the colourmap representing the values of Γ_Y. The lower panel shows the zoomed-in upper right region of the top panel. All represented points feature a relic density in agreement with Planck data and $\Gamma_Y/m_Y \leq 0.2$.

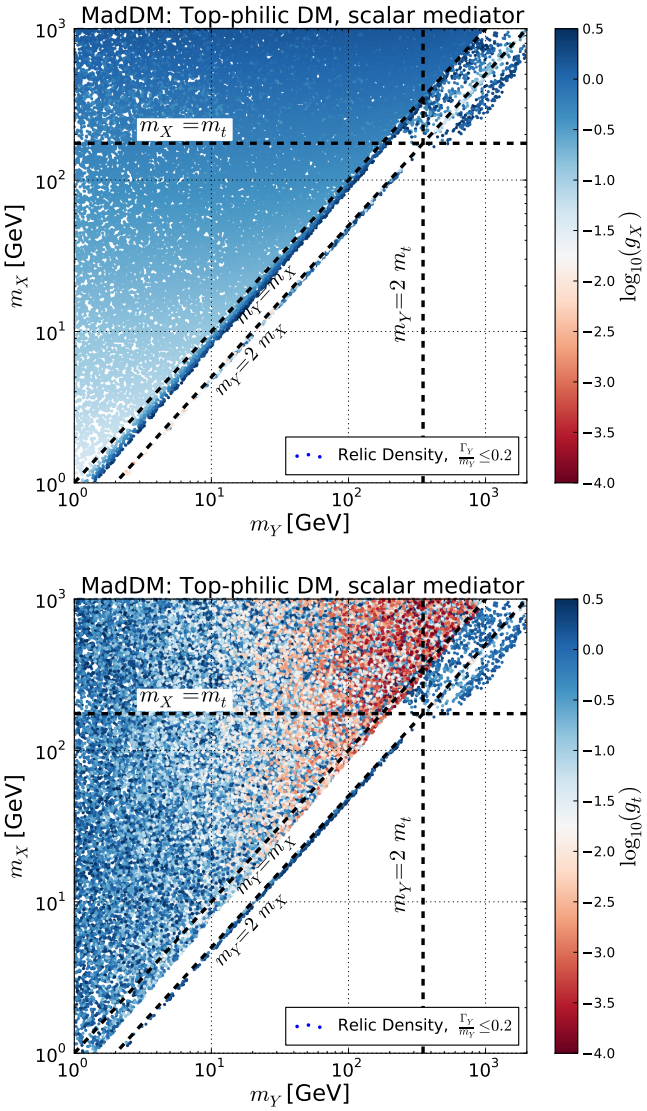


Figure 4.3: Results of our four-dimensional parameter scan using MADDM projected onto the (m_Y, m_X) plane. The top and lower panels show the projections with the colourmap representing the values of g_X and g_t respectively. All represented points feature a relic density in agreement with Planck data and $\Gamma_Y/m_Y \leq 0.2$.

does not lead to predictions of a DM relic density in agreement with the observations. There are also no allowed points for $m_X \lesssim m_t$, except very close to the resonance line. This region is characterised by a dominant mediator decay into gluons, which results in typical $\Gamma_Y/m_Y \ll 1$, a small total DM annihilation cross section, and hence an overproduced DM. The upper limit imposed on the size of the couplings is largely responsible for the absence of allowed points in the region. For instance, taking any m_X value so that the predicted relic density agrees with the observed value, an increase in m_Y will result in a decrease of the annihilation cross section, in turn leading to a higher relic density. The only way (away from the resonance) to restore the correct relic density is then to increase the size of g_X and/or g_t. However, our results show that even for couplings of $\mathcal{O}(1)$, the cross section in this region is too small not to overproduce DM.

The region of parameter space between $m_Y \sim m_X$ and $m_Y \sim 2m_X$ is consistent with the above-mentioned argument. This strip of the ruled out parameter space can be seen as a part of the larger ruled out region for which $m_Y \gtrsim m_X$. Tuning m_X to be close to $m_Y/2$ and assuming a relatively small Γ_Y value is the only way to enhance the DM annihilation cross section and not overproduce DM.

In addition to projections of the allowed parameter space onto the (m_Y, m_X) plane, we have also studied several other projections. Figure 4.4 shows the projections of our results onto the (g_X, g_t) plane (top panel) and (m_X, g_t) plane (lower panel), where we show m_X and m_Y as a colourmap in the first and second panel respectively. Regardless of the value of m_X and m_Y in the considered scan range, there are no solutions for g_X and g_t which satisfy the relic density constraint in the region where $g_t \lesssim 10^{-2}$ and $g_X \lesssim 10^{-1}$. This finding is consistent with the top panel of Fig. 4.3 where we have found that a correct relic density favours g_X couplings of $\mathcal{O}(1)$. Furthermore, we can observe that only couplings of $\mathcal{O}(1)$ result in $\Gamma_Y \gtrsim \mathcal{O}(1)$ GeV, while in the majority of the allowed (g_X, g_t) parameter space regions $\Gamma_Y/m_Y \ll 1$.

We find no striking features in the (m_X, g_t) projection of the scanned parameter space. The unpopulated regions in the lower left corners are artifacts of the lower limit on the coupling size of 10^{-4}.

As a last remark, allowing the scalar mediator to couple to all quarks and leptons would only have a minor impact on our results. The region dominated by the process (III) will indeed stay unchanged, since it is insensitive to the coupling between Y_0 and the SM fermions. As far as it concerns DM annihilation via an s-channel Y_0 exchange, one would have to sum up over all the possible final states kinematically open. This would increase the total annihilation cross section and decrease $\Omega_{\rm DM}h^2$, implying that the constraint of having $\Omega_{\rm DM}h^2 \sim 0.12$ leads to a rescaling of all fermionic couplings towards smaller values with respect to the g_t values shown in this work. The major

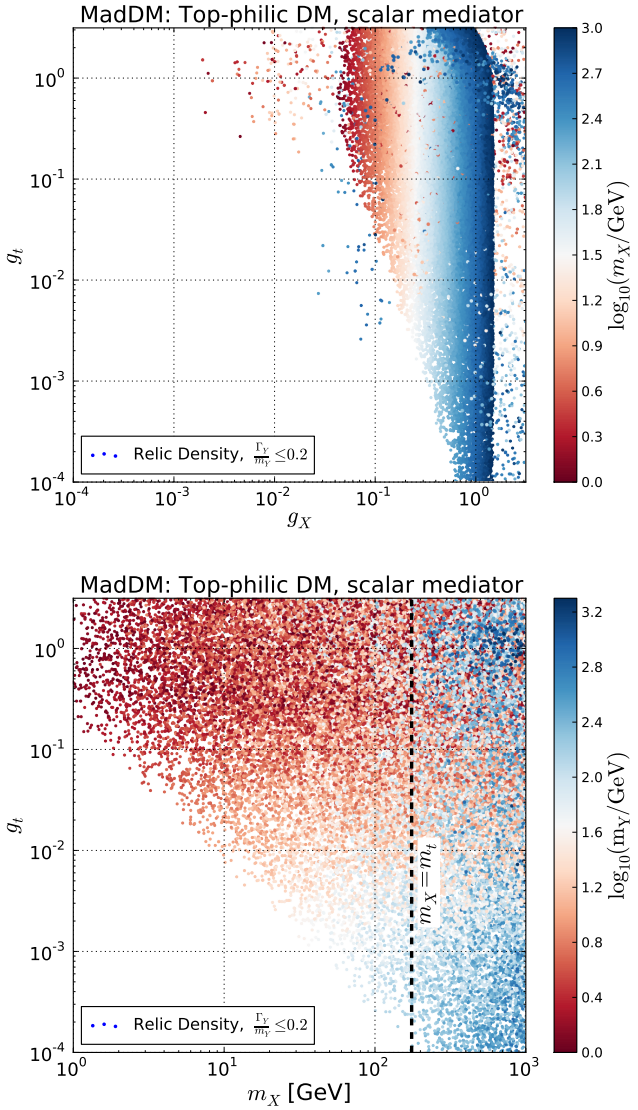


Figure 4.4: Results of our four-dimensional parameter scan using MADDM, projected onto the (g_X, g_t) plane (top) and (m_X, g_t) plane (lower). All represented points feature a relic density in agreement with Planck data and a narrow width mediator.

difference would reside in a potentially larger decay width for Y_0 and hence wider "bands" of the resonance regions of the allowed parameter space.

4.2.2 Constraints from direct detection

Simplified models of DM which feature couplings to quarks and gluons can also be bounded by results from underground direct DM detection experiments. In top-philic DM scenarios, DM scatters off nucleons via the t-channel exchange of Y_0, where the scattering off gluons via triangle top loops accounts for the dominant contribution to the DM-nucleon scattering rate.

The spin independent (SI) DM-nucleon cross section is given by

$$\sigma_{SI}^{n} = \frac{4}{\pi}\left(\frac{m_X m_n}{m_X + m_n}\right)^2 \left[\frac{2}{27}\frac{m_n}{m_t}\frac{g_X g_t}{m_Y^2} f_G\right]^2 , \tag{4.11}$$

where $f_G \equiv 1 - \sum_{q\leq 3} f_q = 0.921$ [147, 185][1] is the gluon form factor and the sum runs over the light quarks $q = u, d, s$, where $m_n \approx 0.938$ GeV is the nucleon mass and $m_t = 173$ GeV is the top quark mass. The expression in Eq. (4.11) does not depend on Γ_Y, simplifying the constraints which can possibly be derived from direct detection. For instance, considering a scenario in which generic m_X and m_Y masses are fixed and where the dominant annihilation process is process (I), direct detection directly constraints the product $g_X g_t$. Extracting the constraint on this quantity in a generic fashion is much more complicated in the case of DM annihilation in the early Universe and at colliders, as the processes involved in DM relic density and DM production calculations intrinsically depend on a quantity which is proportional to $g_X g_t/\Gamma_Y$.

The running of the g_X and g_t couplings could have an effect on the value of the spin independent DM-nucleon scattering cross section [187,188]. However, a proper inclusion of the running couplings would require a careful treatment of the renormalisation group evolution via multiple energy scales which is beyond the scope of our current effort. Instead, we restrict here our calculations to constant g_X and g_t values. The effect of the running couplings would then be equivalent to a rescaling of g_X and g_t to different values.

Next, we have repeated the four-dimensional parameter scan from section 4.2.1 including bounds stemming from direct detection. Figures 4.5 and 4.6 show the results

[1] The gluon form factor suffers from relatively large uncertainties on the strange quark content of the nucleons [186], which we here omit.

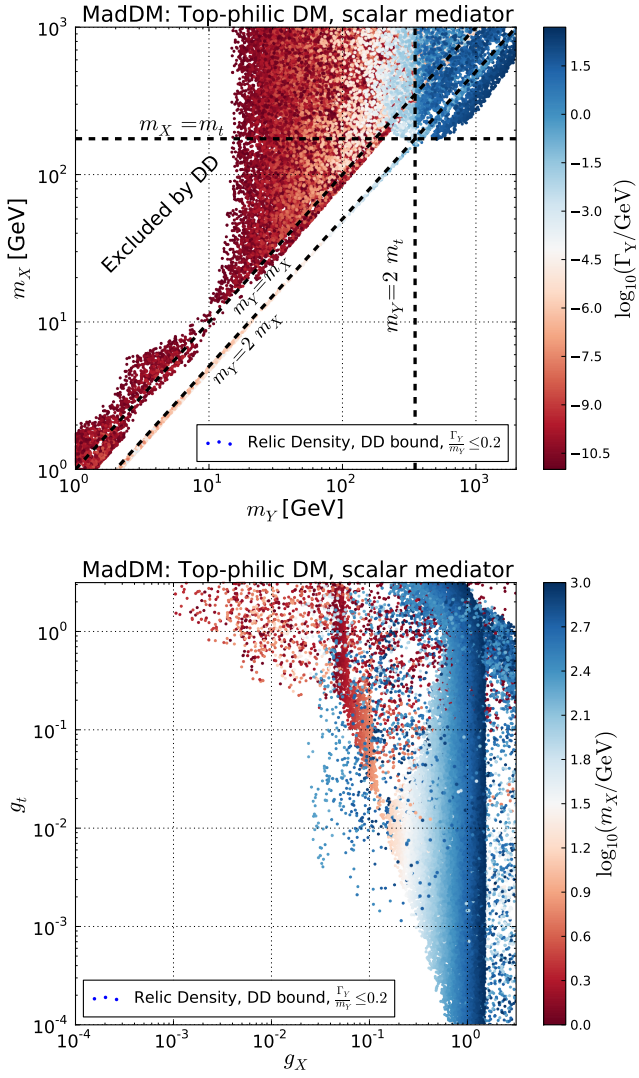


Figure 4.5: Results of our four-dimensional parameter scan using MADDM. The top panel shows the projection of the scan into the (m_Y, m_X) plane with a colourmap representing the values of Γ_Y. The lower panel shows the projection of the allowed points into the (g_X, g_t) plane with a colourmap given by m_X. All represented points feature a relic density in agreement with Planck data, a narrow width mediator and accommodate the direct detection constraints.

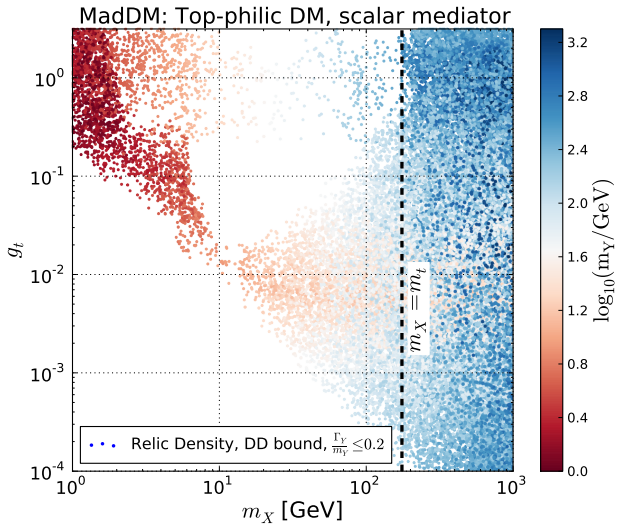


Figure 4.6: Same as Fig. 4.5 but with a projection onto the (m_X, g_t) plane with a colourmap denoting the values of m_Y.

of the scan, projected onto three different planes, where we removed the points excluded by the 95% confidence limit (CL) bound from LUX and CDMSLite. Direct detection rules out a major portion of (m_Y, m_X) space allowed by the relic density constraints (regardless of the coupling value) in the region where $m_X \gtrsim m_Y$, where collider bounds are irrelevant. Figures 4.5 and 4.6 hence serve as a good example for the complementarity among direct detection, relic density and collider bounds. In the (g_X, g_t) plane, direct detection does not rule out a well defined-region (lower panel of Fig. 4.5), indicating that for any pair of couplings (g_X, g_t) in the range of $[10^{-4}, \pi]$ which are allowed by the relic density constraint, it is always possible to find a pair of (m_Y, m_X) values which are not ruled out by direct detection data. In the (m_X, g_t) projection, we finally observe that direct detection rules out a well-defined portion of the parameter space. Furthermore, the constraint also rules out small width points for $g_X \gtrsim 0.1$ and $m_X \gtrsim m_t$. Direct detection bounds are indeed more sensitive to DM masses in the ballpark of 10 to 200 GeV and quickly deteriorate at larger DM masses, since the event rate in the detector scales as $1/m_X^2$. We also see that the direct detection exclusion limit is able to rule out a large portion of the parameter space where Y_0 is light, below 30 GeV, while the sensitivity is quickly lost for heavier masses of the scalar mediator. This can be understood by the $1/m_Y^2$ dependence of the SI elastic cross section of Eq. (4.11). Both mass dependences are illustrated by Fig. 4.6.

4.3 Collider constraints

As discussed in section 4.1, simplified top-philic DM scenarios can be probed at colliders through the production of the mediator either in association with a top-quark pair or through a top-quark loop. Depending on the mass and coupling hierarchy, the mediator decays either into a pair of DM particles, which results in signatures including missing transverse energy, or into SM final states. The size of the cross sections associated with these two classes of mediator production mechanisms is depicted in Fig. 4.7 where we present their dependence on the mediator and DM masses m_Y and m_X. For the case where the mediator is singly produced, we use the Higgs cross section values that are reported in the Higgs Cross Section Working Group documentation [189] and that are evaluated at the next-to-next-to-leading order (NNLO) accuracy in QCD. For all the other cases, the hard-scattering cross section is convoluted with the NNPDF 2.3 [190] set of parton distribution functions (PDF) within MG5_AMC, the PDFs being accessed via the LHAPDF library [109, 191]. We employ a five-flavour-number scheme, and LO and NLO PDFs are used where relevant. The renormalisation and factorisation scales are set to half the sum of the transverse mass of all the final-state particles both for LO and NLO calculations, and the scale uncertainty is estimated by varying the two scales independently by a factor of two up and down. Additional details on the calculation of the $Y_0 t\bar{t}$ cross section are provided in ref. [1] while loop-induced processes are extensively documented in ref. [102].

All the cross sections shown in Fig. 4.7 are proportional to g_t^2 and we therefore arbitrarily choose $g_t = 1$ as a benchmark. In this case, sizeable cross sections of $10^1 - 10^3$ pb are expected for the production of light mediators with $m_Y \lesssim 100$ GeV at a centre-of-mass energy of 8 TeV (left panel), the dominant mechanism being the loop-induced $gg \to Y_0$ production mode. Requiring an extra hard jet in the final state reduces the cross section by a factor which depends on the missing energy (or the jet transverse momentum p_T) selection, and the production rates are not sensitive to the mediator mass as soon as the latter is smaller than the $\not{E}_T$ selection threshold. The cross sections for producing the mediator in association with a SM Higgs or Z boson are further suppressed. In contrast, the cross section related to the production of the mediator in association with a top-quark pair is significant for light mediators, but falls off quickly with the increase in the mediator mass due to phase-space suppression. As a result, a change in the collider energy from 8 to 13 TeV is important for heavy mediators and the cross section can be enhanced by about an order of magnitude. In the right panel of Fig. 4.7, we further show first that the cross sections are constant when the DM particle pair is produced through the decay of an on-shell mediator, and next that they are considerably suppressed when the mediator is off-shell, especially for the $t\bar{t}X\bar{X}$ channel.

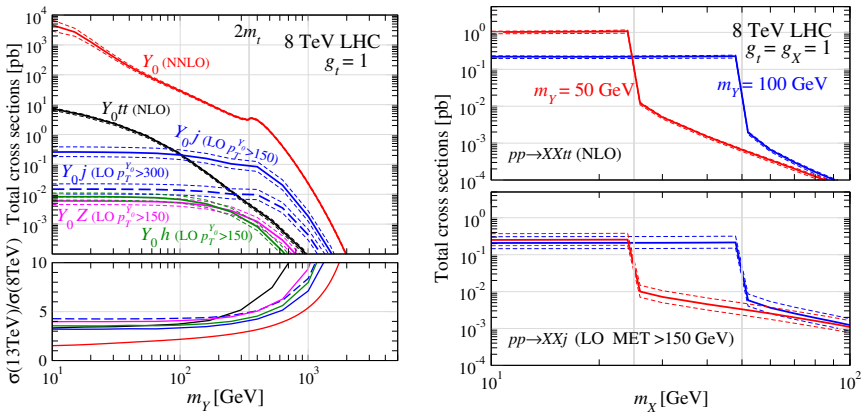


Figure 4.7: Left: Total cross sections (with scale uncertainties) for various mediator production channels (with $g_t = 1$) at a centre-of-mass energy of $\sqrt{s} = 8$ TeV as a function of the mediator mass. The NNLO cross section for single mediator production $\sigma(Y_0)$ is taken from the Higgs Cross Section Working Group report, the $Y_0t\bar{t}$ one is computed at NLO accuracy and all other loop-induced processes are evaluated at LO accuracy. The monojet (Y_0j), mono-Z (Y_0Z) and mono-Higgs (Y_0h) cross sections include a transverse momentum cut on the mediator as indicated in the figure. In the lower panel, we show the ratios of the cross sections evaluated at a centre-of-mass energy of $\sqrt{s} = 13$ TeV over those at 8 TeV. Right: Cross sections for $t\bar{t} + \not{E}_T$ and monojet (with $\not{E}_T > 150$ GeV) production for a mediator mass of $m_Y = 50$ and 100 GeV and at a centre-of-mass energy of $\sqrt{s} = 8$ TeV given as a function of the DM mass.

As already mentioned, the collider searches which provide the most relevant constraints on simplified top-philic DM models are based on the production channels shown in Fig. 4.7 and can in general be divided into two categories. The first category involves signals with missing transverse energy originating from the production of DM particles that do not leave any trace in the detectors and that are accompanied by one or more SM states. The most relevant searches of this type are the production of DM in association with a top-quark pair and the loop-induced production of DM in association with a jet, a Z boson or a Higgs boson. This is discussed in section 4.3.1. The second category of searches relies on Y_0 resonant contributions to SM processes. In our scenario, dijet, diphoton, top-pair and four-top searches are expected to set constraints on the model parameter space. This is discussed in section 4.3.2. As shown below, missing-energy-based searches and resonance searches are complementary and necessary for the best exploration of the model parameter space at colliders.

Final state	Imposed constraint	Reference	Comments
$\not{E}_T + t\bar{t}$	See appendix C.1	CMS [119]	Semileptonic top-antitop decay
$\not{E}_T + j$	See appendix C.2	CMS [192]	
$\not{E}_T + Z$	$\sigma(\not{E}_T > 150\ \text{GeV}) < 0.85\,\text{fb}$	CMS [193]	Leptonic Z-boson decay
$\not{E}_T + h$	$\sigma(\not{E}_T > 150\ \text{GeV}) < 3.6\,\text{fb}$	ATLAS [194]	$h \to b\bar{b}$ decay
jj	$\sigma(m_Y = 500\ \text{GeV}) < 10\,\text{pb}$	CMS [195]	Only when $m_Y > 500\,\text{GeV}$
$\gamma\gamma$	$\sigma(m_Y = 150\ \text{GeV}) < 30\,\text{fb}$	CMS [196]	Only when $m_Y > 150\,\text{GeV}$
$t\bar{t}$	$\sigma(m_Y = 400\ \text{GeV}) < 3\,\text{pb}$	ATLAS [197]	Only when $m_Y > 400\,\text{GeV}$
$t\bar{t}t\bar{t}$	$\sigma < 32\,\text{fb}$	CMS [198]	Upper limit on the SM cross section

Table 4.3: Summary of the 8 TeV LHC constraints used in this paper.

In the rest of this section, we study collider constraints independently from the cosmological and astrophysical ones, and we dedicate section 4.4 to their combination. We moreover allow the mediator couplings to be as large as 2π and do not impose any constraint on the mediator width over mass ratio. We summarise the relevant 8 TeV LHC constraints used in this study in table 4.3 and give details on the $t\bar{t} + \not{E}_T$ and monojet searches that have been recast in the MADANALYSIS 5 framework in appendix C.

4.3.1 Constraints from searches with missing transverse energy

The $t\bar{t} + \not{E}_T$ final state

DM production in association with a top-quark pair ($t\bar{t} + \not{E}_T$) has been explored by both the ATLAS [118] and CMS [119] collaborations within the 8 TeV LHC dataset, and limits have been derived in particular in the effective field theory approach [115, 116]. Such analyses could however be used to derive constraints in other theoretical contexts, and we choose to recast the CMS search to constrain the parameters of the simplified top-philic DM model under consideration. In this work, we simulate $t\bar{t}X\bar{X}$ events at the NLO accuracy in QCD by making use of MG5_AMC. The first study of the genuine NLO effects on the production of a system composed of a pair of top quarks and a pair of DM particles has been presented in ref. [1] in which NLO K-factors have been investigated both at the total cross section and differential distribution level for a series of representative benchmark scenarios. Here, we explore the impact of the NLO corrections on the exclusion limits originating from the $t\bar{t}+\not{E}_T$ channel.

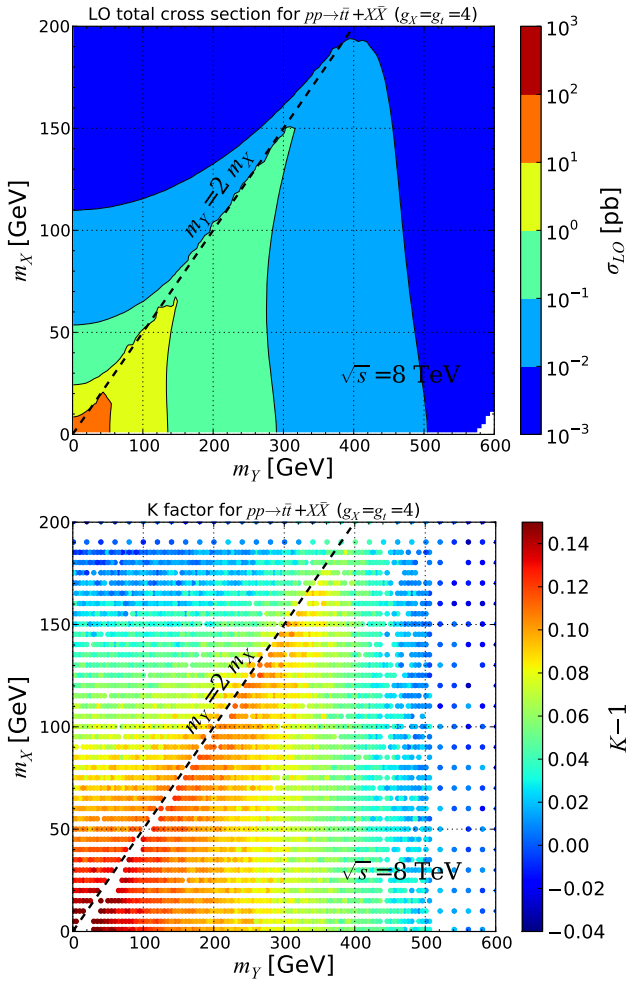


Figure 4.8: LO cross sections (top) and corresponding K-factors (lower) for $pp \to t\bar{t}X\bar{X}$ at $\sqrt{s} = 8\,\text{TeV}$ as a function of the mediator and DM masses. The top and DM couplings to the mediator are set to 4.

In order to examine the reach of the CMS search, we start by performing a two-dimensional scan of the mediator and DM masses with fixed mediator couplings, similar to figure 7 in ref. [106]. The same scan is performed at both LO and NLO accuracy concerning the simulation of the hard scattering process, which allows us to determine the impact of the QCD corrections on the exclusion bounds. Before presenting the results for the excluded regions and to facilitate the discussion, we show the dependence of the LO cross section for $g_t = g_X = 4$ on the new physics masses and the

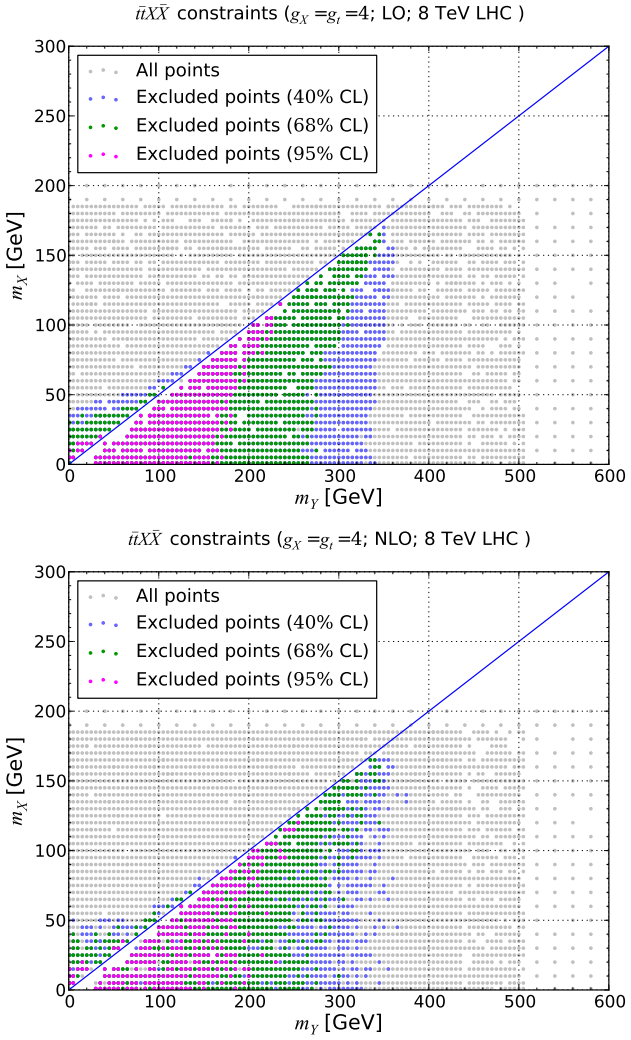


Figure 4.9: Constraints on simplified top-philic DM scenarios from the CMS 8TeV $t\bar{t} + \not{E}_T$ analysis [119]. The top and DM couplings to the mediator are set to 4 while the mediator and DM masses are allowed to vary freely. LO and NLO exclusions are respectively shown in the top and lower panels of the figure.

corresponding K-factors in Fig. 4.8. The cross section is the largest in the low mass regions where the mediator can resonantly decay to a pair of DM particles, and falls steeply in the off-shell regions. In particular, the region where $2m_X < m_Y < 2m_t$ is characterised by mediator decays either into a pair of DM particles or into a pair of

gluons. These two decay rates are related by (see section 4.1)

$$\frac{\Gamma(Y_0 \to gg)}{\Gamma(Y_0 \to X\bar{X})} = \frac{g_t^2}{g_X^2} \frac{\alpha_s^2}{9\pi^2\beta_X^3} \frac{m_Y^2}{v^2} \sim \left(\frac{g_t}{g_X}\right)^2 \times 10^{-5} \frac{m_Y}{\text{GeV}}, \tag{4.12}$$

which suggests that the decay rate into a pair of DM particles is always significantly higher, except in the case of a large hierarchy between the couplings ($g_t/g_X \gtrsim 100$). For $m_Y > 2m_t$, the $Y_0 \to t\bar{t}$ decay mode is open, and $t\bar{t} + \not{E}_T$ production turns out to be suppressed by the visible decay channels of the mediator, unless $g_X > g_t$. Such a feature has already been illustrated in Fig. 4.1. The NLO K-factors related to $t\bar{t} + \not{E}_T$ production (lower panel of Fig. 4.8) are found to vary from 0.96 to 1.15 in the range of masses examined here, the QCD corrections being more important in the low mass region.

The results for the exclusion regions are shown in Fig. 4.9 when LO (top panel) and NLO (lower panel) simulations are used; see more details on the recasting procedure in appendix C.1. Setups excluded at the 40%, 68% and 95% confidence level (CL) are marked separately in the figures. As expected from the total cross section results, all excluded points (at the 95% CL) lie in the triangular low-mass region where the mediator resonantly decays into a DM particle pair. The exclusion region reaches mediator masses of about 200–250 GeV if close to threshold ($m_Y \sim 2m_X$). This region is in fact not exactly triangular as for a given mediator mass, not all DM masses below $m_Y/2$ are excluded. This is related to the parametric choice of $g_t = g_X = 4$ for which the mediator width can become large. In this case, the narrow width approximation is not valid and the $t\bar{t} + \not{E}_T$ cross section acquires a dependence on the DM mass even in the resonant region.

Comparing the LO and NLO results, we observe that in the low mass resonant region where the K-factor is small and of about 1.10, the exclusion contours are mildly modified and this small 10% shift in the cross section does not lead to any significant change. For larger mediator masses, the K-factors are ~ 1 and therefore do not imply a modification of the exclusion regions, if the central prediction at the default choice of scale is considered. However, the inclusion of NLO corrections significantly reduces the theoretical error and thus leads to sharper exclusion bounds.

Mono-X final states

In addition to the constraints that can be derived by means of $t\bar{t} + \not{E}_T$ probes and that have been discussed in the previous section, mono-X searches can also be relevant for obtaining bounds on our top-philic DM model. Monojet [192, 199, 200], mono-Z [193, 201–204] and mono-Higgs [194, 205–207] signals have been searched for during the first run of the LHC, and these search results could be recast to constrain the

DM model studied in this work. In contrast to tree-level DM production in association with a pair of top quarks, the production of a pair of DM particles with a jet, a Z-boson or a Higgs boson proceeds via a gluon fusion top-quark loop diagram. Although they have been largely studied by ATLAS and CMS, monophoton analyses cannot be used as charge conjugation invariance forbids the existence of a monophoton signal for the spin-0 mediator scenario.

Monojet

We start by discussing constraints that can be imposed by the CMS 8 TeV monojet analysis [192]. For this study, hard-scattering events are generated at the LO accuracy within MG5_aMC, and the matching with parton showers is made with PYTHIA 6. The results are analysed in MADANALYSIS 5 that also takes care of the detector simulation using its interface with DELPHES 3. This recasting procedure allows us to exclude any specific parameter space point at any desired confidence level, our exclusion being conservatively derived on the basis of the signal region that drives the strongest bound. This limitation is related to the lack of public information, the statistical model used by CMS for the combination being not available. One can find more details for the recasting procedure in appendix C.2.

Similar to the $t\bar{t}+\not{E}_T$ analysis of the previous section, we perform a two-dimensional scan on the mediator and DM masses while fixing both new physics couplings to $g_t = g_X = 4$ (as in figure 5 in ref. [106]). Figure 4.10 shows our results, where we represent the scenarios excluded at the 40%, 68% and 95% CL. The bulk of the excluded points lie again in the triangular low-mass region where the mediator resonantly decays into a pair of DM particles. Except for the small subset of points excluded at the 40% and 68% CL in the region where $m_Y < 2m_X$, the extent of the exclusion region is determined by the significant reduction of the monojet cross section below the resonant production threshold already presented in Fig. 4.7. The $pp \to Y_0 j$ cross section indeed rapidly falls with m_Y, reaching levels beyond the sensitivity of the 8 TeV search at $m_Y \sim 500$ GeV. In addition to the decrease of the $Y_0 j$ production cross section, the opening of the mediator decay mode into a top-antitop system when $m_Y > 2m_t$ leads to a further reduction of the monojet production rate. In comparison with the $t\bar{t}+\not{E}_T$ case, the monojet search overall appears to be more constraining, especially for higher mediator mass values thanks to the larger monojet cross section.

As shown in ref. [102], the shape of key monojet differential distributions differs in the resonant and in the off-shell parameter space regions. While the total cross section falls dramatically in the off-shell region $m_Y < 2m_X$ (as shown in Fig. 4.7), the $\not{E}_T$ and jet transverse momentum distributions tend to be harder for off-shell production

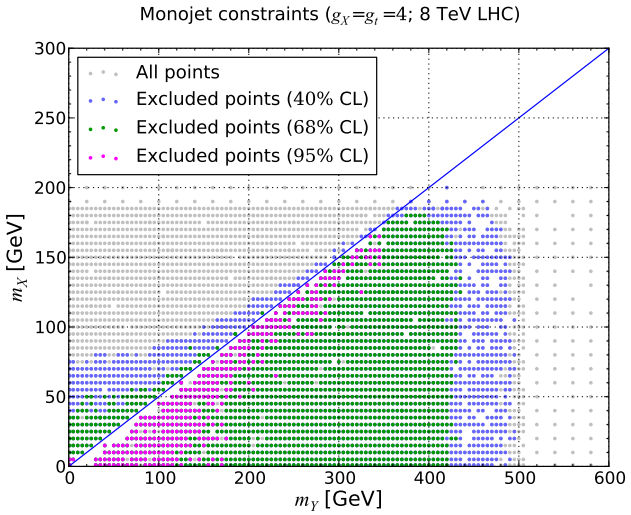


Figure 4.10: Constraints on the simplified top-philic DM model from the CMS 8 TeV monojet analysis [192]. The top and DM couplings to the mediator are set to 4 while the mediator and DM masses are allowed to vary freely.

compared to resonant cases. This implies that for off-shell scenarios a larger fraction of events features high missing transverse energy ($\not{E}_T$ >250 GeV) and populates the different signal regions of the CMS analysis. As a result, a better sensitivity is found than what one might expect from considering the total cross section alone. This feature leads to the exclusion of DM scenarios where $m_Y < 2m_X$, as depicted in Fig. 4.10.

In our simulation of the monojet signal, we have ignored the possible impact of the merging of event samples featuring different final state jet multiplicities. A reliable description of the high transverse momentum spectra of the leading jet typically necessitates the merging of event samples including at least one and two jets in the final state [102]. We have explicitly verified that for both resonant and off-shell scenarios, employing a merged sample does not have a big impact on the $\not{E}_T$ distribution and therefore on the resulting exclusion contours. This originates from the analysis selection strategy that requires one single hard jet and rather loose requirements on the second jet, so that the configuration that dominates consists of a single hard jet recoiling against the missing energy. Such a configuration is described similarly by the one-jet and merged samples.

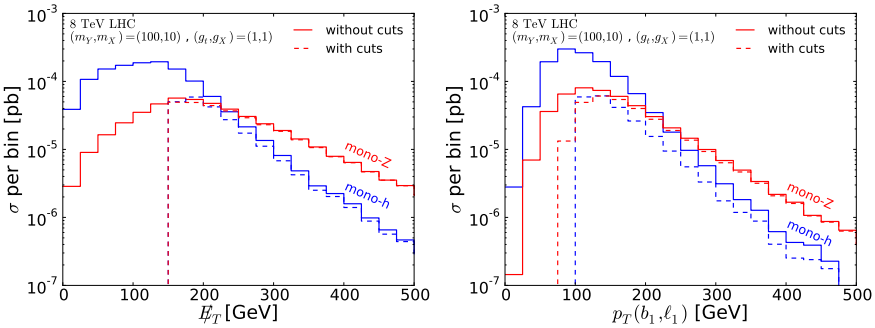


Figure 4.11: Distributions of missing transverse energy and of the transverse momentum of the leading lepton (b-quark) for mono-Z (-Higgs) production at $\sqrt{s} = 8\,\text{TeV}$ for $(m_Y, m_X) = (100, 10)\,\text{GeV}$ and $(g_t, g_X) = (1, 1)$, without and with including the analysis selections.

Mono-Z and mono-Higgs

In addition to the use of monojet processes, we explore the possibility of constraining the parameter space of our model using mono-Z and mono-Higgs production. While the production rates are much smaller than the monojet rate as seen in Fig. 4.7, the backgrounds can be also small. Therefore, these search channels can be sensitive to the top-philic simplified DM model, as we will see below. Here, instead of employing a full recasting procedure as in the $t\bar{t}+\not{E}_T$ and monojet analyses, we perform parton-level analyses to provide rough estimates of the constraints on our model parameters.

We rely on the CMS search for DM production in association with a Z-boson that decays leptonically [193], in which a 95% CL upper limit on the visible cross section of 0.85 fb is obtained once a $\not{E}_T$ requirement of at least 150 GeV and the minimal detector selection requirements for the leptons ($p_T^\ell > 20\,\text{GeV}$ and $|\eta^\ell| < 2.5$) are considered. We generate events for this process, and after applying the above fiducial selection requirements we obtain a cross section of 0.30 fb for $(m_Y, m_X) = (100, 10)\,\text{GeV}$ and $g_t = g_X = 1$. We show in Fig. 4.11 the $\not{E}_T$ and leading lepton transverse momentum distributions (red lines) without and with applying the selection strategy. While we have not performed a detailed study, simple estimates show good prospects for setting limits on the parameter space of the model using the mono-Z analysis results. Using the upper limit of 0.85 fb, scenarios with couplings close to $g_t \sim 2$ could be excluded in the resonant region ($m_Y > 2m_X$) with $m_Y < 100\,\text{GeV}$. For larger mediator masses, the cross section starts to fall due to the reduction of the phase space. In the off-shell region ($m_Y < 2m_X$), the mono-Z cross section suffers from the same drastic decrease seen in Fig. 4.7 for the $t\bar{t} + \not{E}_T$ and monojet cases.

The same procedure can be repeated to constrain the parameter space of the model using mono-Higgs events on the basis of the results of the ATLAS search for DM production in association with a Higgs boson decaying into two bottom quarks [194]. This search results in a 95% CL upper limit on the visible cross section of 3.6 fb for a $\not{E}_T$ threshold of 150 GeV. In order to estimate a limit, we generate events for $(m_Y, m_X) = (100, 10)$ GeV and $g_t = g_X = 1$, and require the two b-quarks to have a transverse momentum $p_T^{b_1} > 100$ GeV and $p_T^{b_2} > 25$ GeV, a pseudorapidity $|\eta^b| < 2.5$ and to be separated in the transverse plane by an angular distance $\Delta R(b_1, b_2) < 1.5$. Moreover, we only select events exhibiting at least 150 GeV of missing transverse energy. We show again in Fig. 4.11 the $\not{E}_T$ and leading b-quark transverse momentum distributions (blue lines) without and with applying the above-mentioned selection requirements. We then include a b-tagging efficiency of 60% and extract an upper limit on the g_t coupling by comparing our results to the ATLAS limit. Coupling values of $g_t > 2$ are found to be excluded for $m_Y > 2m_X$ with $m_Y < 100$ GeV. All other parameter space regions suffer from the same limitations as the mono-Z case.

From our naive parton-level analysis, we have seen that mono-Z and mono-Higgs signals show promising signs of setting constraints on the parameter space of the model and therefore deserve dedicated studies, which will be reported elsewhere (see also ref. [208]). The sensitivity to such signals will benefit from applying more aggressive $\not{E}_T$ thresholds to ensure the reduction of the corresponding backgrounds. As seen in Fig. 4.11, we obtain a rather hard $\not{E}_T$ distribution [102], especially for mono-Z production. The result implies that an increase in the $\not{E}_T$ threshold requirement in future analyses could lead to a significant improvement of the sensitivity, especially given the fact that SM backgrounds rapidly fall off with the increase in missing energy.

4.3.2 Constraints from searches without missing transverse energy

In this section we set constraints on the simplified top-philic DM model based on experimental results coming from dijet, diphoton and top-antitop resonances searches as well as four-top signals.

Dijet and diphoton resonance search results could (in principle) be used to constrain the simplified top-philic DM model. Due to double-loop suppressions, mediator-induced contributions to dijet and diphoton production are only relevant in the parameter space regions where $m_Y < 2m_X, 2m_t$ ($i.e.$ where the mediator cannot decay

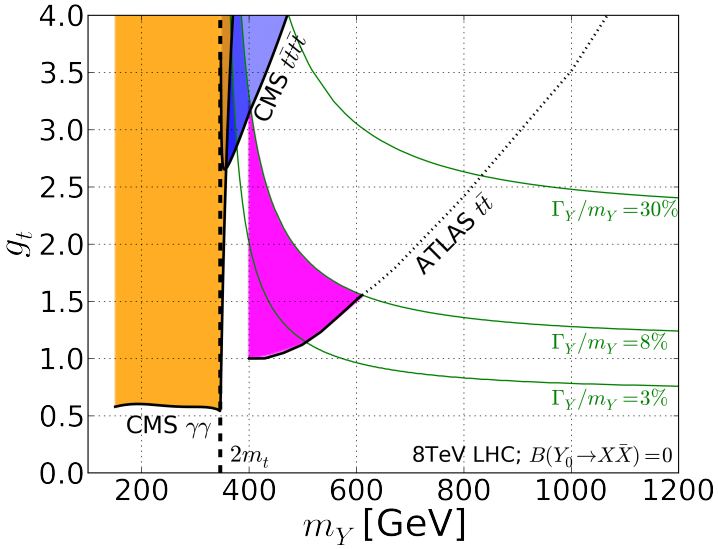


Figure 4.12: Resonance search constraints from the LHC results at a collision centre-of-mass energy of 8 TeV on the simplified top-philic DM model presented in terms of the mediator mass m_Y and the g_t coupling. The different coloured areas are excluded by the diphoton [196] (orange), $t\bar{t}$ [197] (magenta) and $t\bar{t}t\bar{t}$ [198] (blue) searches. We include information on the mediator width to mass ratios (green curves). We assume a negligible branching ratio to the invisible sector.

into top quarks and/or DM particles). The partial mediator decay rate into gluons is then always dominant (as mentioned in section 4.1) since

$$\frac{\Gamma(Y_0 \to \gamma\gamma)}{\Gamma(Y_0 \to gg)} \sim \frac{8}{9}\frac{\alpha_e^2}{\alpha_s^2} \approx 10^{-3} \,. \tag{4.13}$$

All LHC dijet resonance searches focus on the dijet high invariant-mass region, leading to no useful constraints on the top-philic DM model. The lowest mediator mass that is probed is ~ 500 GeV, with a visible cross section restricted to be smaller than 10 pb [209].

Although the branching ratio of the mediator into a photon pair is very small, the background associated with a diphoton signal is low so that one expects to be able to obtain stringent constraints on the model from the diphoton search results. We focus here on the CMS 8 TeV diphoton search [196] that investigates resonance masses

ranging from 150 GeV to 850 GeV and derives limits on the corresponding cross section. For instance, the 95% CL upper bound on the mediator-induced diphoton production cross section $\sigma(pp \to Y_0 \to \gamma\gamma)$ is of 20 fb (4 fb) for a mediator mass of 150 GeV (300 GeV). Making use of the $pp \to Y_0$ cross section values shown in Fig. 4.7 and the $Y_0 \to \gamma\gamma$ branching ratio computed from the formulas shown in section 4.1, we present diphoton constraints on the model in the (m_Y, g_t) plane in Fig. 4.12. These results assume that the DM particle is much heavier than the mediator that can thus not resonantly decay invisibly. The constraints are found to be stringent below the $2m_t$ threshold, where the g_t coupling cannot be larger than 0.6.

For scenarios with mediator masses above the top-antitop threshold ($m_Y > 2m_t$), $t\bar{t}$ resonance searches [197, 210] can be used as probes of the model. In our setup, loop-induced resonant mediator contributions can indeed enhance the $t\bar{t}$ signal, in particular when there is a large coupling hierarchy ($g_t \gg g_X$) or mass hierarchy ($2m_t < m_Y < 2m_X$). We derive constraints on our model from the ATLAS 8 TeV $t\bar{t}$ resonance search [197] that relies on the reconstruction of the invariant mass of the top-quark pair to derive a 95% CL exclusion on the existence of a new scalar particle coupling to top quarks. The associated cross section limits range from 3.0 pb for a mass of 400 GeV to 0.03 pb for $m_Y = 2.5$ TeV, assuming that the narrow width approximation is valid with a mediator width being of at most 3% of its mass and that there is no interference between the new physics and SM contributions to the $t\bar{t}$ signal.

Constraints are computed using the NNLO mediator production cross section (see Fig. 4.7) and the relevant top-antitop mediator branching ratio derived from the formulas presented in section 4.1. The latter is in fact very close to one in the relevant region, the mediator decays into DM particle pairs being kinematically forbidden and those into gluons and photons loop-suppressed. The results are presented in the (m_Y, g_t) plane in Fig. 4.12. This shows that scalar mediators with masses ranging from 400 GeV to 600 GeV could be excluded for g_t couplings in the $[1, 4]$ range, the exact details depending on m_Y and on the fact that the narrow-width approximation must be valid. This demonstrates the ability of the $t\bar{t}$ channel to probe a significant portion of the $m_Y > 2m_t$ region of the model parameter space. In the region where $2m_t$, $2m_X < m_Y$, the partial decay $Y_0 \to X\bar{X}$ reduces the $t\bar{t}$ signal and therefore limits the sensitivity of the search.

Scenarios featuring a mediator mass above twice the top-quark mass can be probed via a four-top signal, since the mediator can be produced in association with a pair of top quarks and further decay into a top-antitop system. Theoretically, the SM four-top cross section has been calculated with high precision [211], but the sensitivity of the 8 TeV LHC run was too low to measure the cross section. Instead, an upper limit on the cross section at a centre-of-mass energy of 8 TeV has been derived [198, 212]. The four-top production rate is constrained to be below 32 fb [198], a value

that has to be compared to the SM prediction of about 1.3 fb. Only models with new physics contributions well above the background (see *e.g.* ref. [213]) can therefore be constrained by the four-top experimental results.

In our top-philic DM model, the new physics contributions to the four-top cross section can be approximated by the $t\bar{t}Y_0$ cross section, the branching ratio $B(Y_0 \to t\bar{t}) \sim 1$. Using the NLO cross section (see Fig. 4.7), we derive limits that we represent in the (m_Y, g_t) plane in Fig. 4.12. A small region of the parameter space with $g_t > 2.5$ and in which the mediator mass lies in the $[2m_t, \sim 450\ \mathrm{GeV}]$ mass window turns out to be excluded. The weakness of the limit is related to the steeply decreasing cross section for $pp \to Y_0 t\bar{t}$ with the increase in m_Y.

In all the above studies where the final state does not contain any missing energy, the mediator width has been assumed narrow. Concerning the diphoton channel, this assumption holds within the entire excluded region as only loop-suppressed gluon and photon mediator decays are allowed. In the region where $m_Y > 2m_t$, the width of the mediator rises quickly with its mass, and the width over mass ratio rapidly exceeds the 3% value that has been imposed in the ATLAS $t\bar{t}$ resonance search [197] as can be seen in Fig. 4.12. The reinterpretation of the ATLAS results to a generic $t\bar{t}$ resonance model should therefore be made carefully, as the limit cannot be necessarily applied to scenarios featuring significantly larger mediator widths. This is shown in Fig. 4.12 by a dotted line, and we can also observe that most of the points that would have been excluded by the ATLAS search do not fulfil the requirement of a width below 3% of the mediator mass. In our excluded region of the parameter space, we allow the mediator width to reach 8% of its mass, by the virtue of the experimental resolution on the invariant mass of the $t\bar{t}$ system. This leads to the exclusion of scenarios with mediator masses up to 600 GeV.

The ATLAS resonance $t\bar{t}$ study claims that varying the width of the resonance from 10% to 40% for the massive gluon model results in a loss in sensitivity by a factor 2 for a 1 TeV resonance. An extension of the reinterpretation of the ATLAS limits on our simplified top-philic DM model to the case of larger resonance widths could then be performed by rescaling the limits by the appropriate correction factor. We have nonetheless found that no additional points are excluded even without rescaling the sensitivity of the search as the ATLAS analysis rapidly loses sensitivity for resonance masses above 600 GeV. Considering model points with a mediator width to mass ratio of at most about 8% therefore provides a realistic exclusion over the entire model parameter space.

Mediator resonance searches at 8 TeV show good prospects of constraining our simplified top-philic DM model, especially in the mediator mass range of 150–345 GeV and 400–600 GeV by means of the diphoton and top-pair searches respectively. So far, the $t\bar{t}$ resonance searches are strictly applicable to a limited parameter space region of

the simplified model, and considering larger widths in the interpretation of the future results would allow for a more straightforward reinterpretation of the limits to a wider range of parameters. Concerning the four-top analysis, it can presently only exclude a restricted part of the parameter space, but future measurements are expected to lead to more competitive bounds.

Finally, the $pp \to t\bar{t} + j$ channel could also be used to probe DM models coupling preferably to top quarks. This has been for instance shown in ref. [120] where a loop-induced production of $t\bar{t}j$ can in some cases lead to interesting constraints on top-philic models of new physics. In our case, they are nonetheless not expected to give more stringent constraints than the $t\bar{t}$ resonance searches. One could also consider the $pp \to t\bar{t}tj$ and $pp \to t\bar{t}Wt$ processes [120]. Because of the magnitude of the electroweak couplings, these processes are characterised by cross sections smaller than when four top quarks are involved, and are hence not likely to set more stringent constraints on the class of models under consideration.

4.4 Combined constraints

The final segment of our comprehensive study of top-philic DM simplified models is a combined study of astrophysical and collider constraints. We find that in the region where $g_X, g_t \leq \pi$, the 8 TeV collider results that provide relevant bounds (once the relic density and direct detection constraints are imposed) originate from direct mediator production searches when the mediator further decays into a pair of SM particles. Figure 4.13 illustrates our results and shows the scenarios that are excluded by resonant diphoton and top-pair searches as well as by the four-top analysis. All points in the plot accommodate the DM relic density and direct detection constraints, while the colours indicate points excluded by individual complementary collider bounds. The vast majority of excluded points lie in the region where $2m_X > m_Y$ with $m_Y \in [150, 600]$ GeV. This is the region where the mediator decay into a pair of DM particles is kinematically forbidden, ensuring large branching fractions for decays into SM particles. The diphoton resonance search excludes points below the $2m_t$ threshold, while $t\bar{t}$ results constrain the $400 < m_Y < 600$ GeV region. The four-top probe is able to exclude a narrow parameter space region close to $m_Y \sim 2m_t$, in agreement with the findings shown in Fig. 4.12.

Relaxing the requirements on the relic density, the direct detection and the upper bound on the coupling strengths allows for another meaningful study of combined collider constraints. For this purpose we have performed a joint analysis of collider

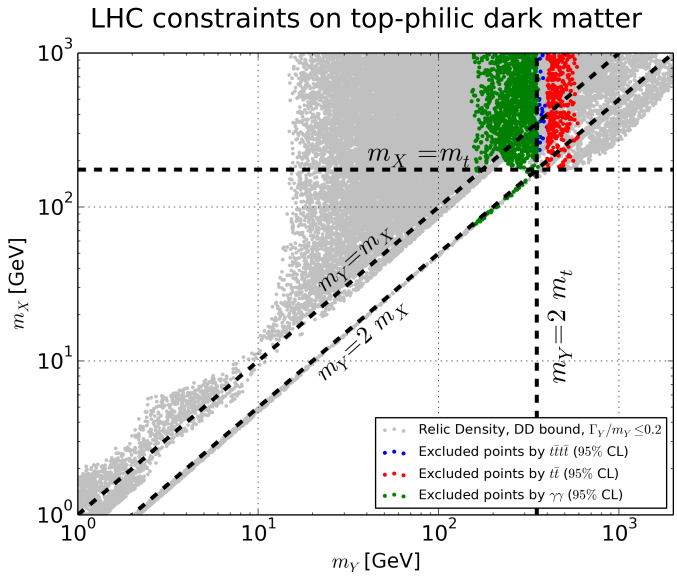


Figure 4.13: Results of our four-dimensional parameter scan projected onto the (m_Y, m_X) plane once constraints set from the LHC results are imposed. The points excluded by the diphoton, the $t\bar{t}$ and the four-top considered searches all satisfy the relic density, narrow width and direct detection constraints.

bounds on the top-philic simplified DM model in the scope of a four-dimensional parameter scan with a flat likelihood function over all dimensions. We have performed the scan by restricting the couplings to be smaller than 2π, as well as by allowing the mediator widths to reach 50% of the mediator mass. Figure 4.14 shows the model points which are excluded by the combination of all collider results. Figures containing the points excluded by individual LHC Run I collider results are shown in Appendix D. We find that the 8 TeV monojet searches exclude model points which lie mainly in and around the triangle bounded by the $m_Y = 2m_X$ and $m_Y = 2m_t$ lines, where the characteristic g_t which is excluded by the 8 TeV results is of $\mathcal{O}(10)$. The region in which the excluded points are located is reasonable, as we expect any significant monojet signal in the region where $m_Y > 2m_X$. Furthermore, we expect the branching ratio to missing energy to be lower in the region where $m_Y > 2m_t$ due to the kinematically allowed decays into a pair of top quarks. This in turn leads to a lower signal cross section in all channels with missing energy and hence a lower number of points which can be excluded by monojet searches in the $m_Y > 2m_t$ region.

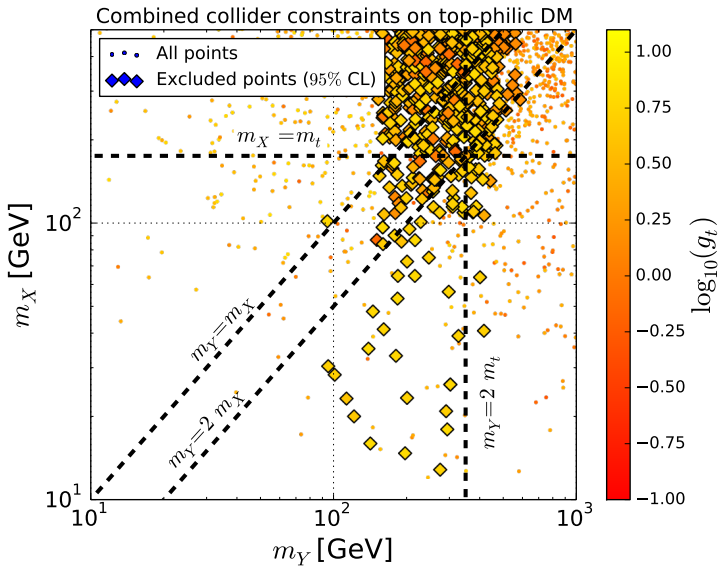


Figure 4.14: Combined constraints derived from the LHC Run I results on the simplified top-philic DM model. The panel shows a combination of all relevant collider constraints (monojet, $t\bar{t} + \not{E}_T$, resonant $t\bar{t}$, four top and diphoton searches). We use a four-dimensional parameter scan, uniform on the linear scale. The results assume couplings smaller than 2π and $\Gamma_Y/m_Y < 0.5$, with no constraints from astrophysics or cosmology being imposed.

The points excluded by the 8 TeV $t\bar{t} + \not{E}_T$ measurements lie in roughly the same region as the points excluded by the monojet search, but with a more defined edge of $m_Y = 2m_t$. Conversely, the 8 TeV $t\bar{t}$ resonance search provides constraints in the region of $m_Y \in [400, 600]$ GeV and $m_X \gtrsim 100$ GeV, and is able to rule out g_t couplings of $\mathcal{O}(1)$. The four top searches constrain roughly the same region of the (m_Y, m_X) parameter space as the $t\bar{t}$ searches. However, the characteristic size of the couplings four top searches are able to constrain is significantly larger than the case of $t\bar{t}$.

Finally the diphoton resonance search excludes $m_Y \in [150, 2m_t]$ GeV with $2m_X > m_Y$, ruling out g_t couplings larger than 0.6. In the (m_Y, m_X) plane, we can observe that the constraints arising from all mediator resonance searches, *i.e.* the diphoton and $t\bar{t}$ analyses, are largely complementary to those issued from searches in channels with large missing energy.

Conclusion

This thesis aimed at combining cosmological, astrophysical and collider DM searches for the sake of completeness and accuracy. As the nature of DM is still unknown, we used a minimal phenomenological approach to describe DM physics. We built DM simplified models to achieve this aim. For the first time we computed collider cross sections at NLO accuracy in a simplified model framework. We also made a big step forward providing an unified numerical framework for DM physics, linking MG5_aMC to MadDM.

In chapter 2, we set up the theoretical framework of DM simplified models. Such a class of models only contains four degrees of freedom while keeping the salient features of UV-complete theories. Unlike effective field theories, DM simplified models preserve unitarity at the typical energy scales involved at LHC. On top of that, we investigated the possible effects of taking into account higher order QCD corrections at LHC. We found that going to NLO considerably reduces the scale uncertainties and might affect the shape of differential distributions compared to LO ones.

In chapter 3, we reported on MadDM which provides a consistent framework to compute DM relic density and direct detection rates in generic models. We focused on the recent implementation of direct detection searches into MadDM v 2.0. Additionally, the implementation of twist-2 operators in the direct detection module of MadDM is ongoing. As a future perspective, MadDM will also be able to compute indirect detection rates as well as NLO cross sections in the MG5_aMC framework.

In chapter 4 we gathered together the collider studies and the cosmological and astrophysical constraints from MadDM in the DM simplified model approach of Chapter 2. For this purpose, we presented a comprehensive analysis of simplified top-philic DM models, in the scope of collider physics, astrophysics and cosmology. Our study considered the full four dimensional model parameter space, where we treated the

experimental constraints on the model space both separately and in conjunction with each other. The requirement of predicting the measured relic density $\Omega_{\rm DM}h^2$ gives the most stringent constraint on the viable regions of the parameter space. Most of the region where $m_Y > m_X$ cannot accommodate the observed relic density, except near the resonance $m_Y \sim 2m_X$ and for $m_X > m_t$. Direct detection data complementary exclude large portions of the parameter space in the $m_Y < m_X$ region once experimental results from LUX and CDMSLite are accounted for. In the context of DM indirect detection, we studied prospects for further model constraints from gamma-ray flux measurements originating from dwarf spheroidal galaxies and the gamma-ray lines issued from the inner galactic region. In the specific model we consider, the DM annihilation cross section is p-wave suppressed, leading to indirect detection bounds which are too weak to provide additional constraints on the parameter space.

Collider searches from LHC Run I at $\sqrt{s} = 8$ TeV can constrain the parameter space beyond the limits obtained from the relic density and direct detection, but apply mostly in the limit of coupling values $\gtrsim 1$. We found that for couplings of $\lesssim \pi$, the resonant $t\bar{t}$ and diphoton searches are able to exclude a fraction of model points in the regions of $m_Y \sim 400 - 600$ GeV and $m_Y \sim 150 - 350$ GeV respectively, even upon assuming astrophysical and relic density constraints.

In addition to studying collider signatures of the top-philic DM simplified model as a complementary way of DM detection, we performed a study of collider constraints without assuming relic density and direct detection (as well as extended the parameter range to include coupling values of $< 2\pi$ and $\Gamma_Y \leq 0.5 m_Y$). Our results for a four dimensional parameter scan show that (in the scenario where astrophysical and cosmological constraints are not relevant), $\not{E}_T + j$ and $\not{E}_T + t\bar{t}$ at 8 TeV results provide meaningful bounds on the model parameter space in the $2m_X < m_Y < 2m_t$ region, but only for $g_t, g_X \gtrsim \pi$. In the $m_X > m_t$ region, the resonant $t\bar{t}$ searches are again able to exclude some model points in the $m_Y \sim 400 - 500$ GeV region, while $\gamma\gamma$ measurements provide constraints in the $m_Y < 2m_t$ region. We have also explored the prospects of using rarer processes such as four-top production as well as mono-Z and mono-Higgs production to constrain our model. While we have not performed a detailed analysis we have found that these processes show promising signs of further constraining the parameter space of our model and deserve dedicated studies.

For the purposes of our study we have recast the CMS monojet and $\not{E}_T + t\bar{t}$ searches in the framework of MADANALYSIS 5, which allows us to reliably extract constraints on our model, and can benefit future collider studies which go beyond our simplified model and even beyond DM searches. Another important aspect of our work, is the use of NLO QCD predictions for the $\not{E}_T + t\bar{t}$ process to constrain our model. While we find that K-factors for this process are close to one, the importance of taking higher order effects into account lies in the reduced theoretical uncertainties of the NLO

results. We have shown that the uncertainties in the CL estimates significantly reduce with the inclusion of higher order QCD terms which clearly illustrates the importance of higher order corrections on the interpretation of DM searches at colliders.

The complete analysis of Chapter 4 has only been done for LHC Run I due to the lack of preliminary results at LHC Run II at that time. However, it would be interesting to redo the analysis when the Run II results will be available. This should be the motivation of a future work as well as allowing the mediator to be a pseudo-scalar particle. Unlike the scalar case, indirect detection should be able to constrain the parameter space for a pseudo-scalar mediator since cross sections will not be p-wave suppressed.

As a future perspective, considering DM simplified models with spin-2 mediator could also be a very interesting path. For a long time, the complex structure of such models has been an obstacle to study its phenomenology. However, lots of effort have been made to implement a spin-2 mediator in the MG5_AMC framework for collider studies [214]. Today, spin-2 mediator becomes more popular. Ref. [215, 216] already covered DM simplified models with a spin-2 mediator (Y_2) at LHC, but a combined study of cosmological, astrophysical and collider constraints would be an asset especially if we manage to implement correctly the 4-point interaction necessary to compute $X\bar{X} \to Y_2 Y_2$ cross sections (see Ref. [217]). So far, only t-channel diagrams involving the exchange of a DM particle are available.

So far, we only focused on s-channel DM simplified models seeking for simplicity but t-channel DM simplified models have a richer QCD structure and it would be challenging to study combined constraints on DM using the same procedure we applied in this thesis. Actually, as we saw in the summary of Chapter 2, the technology is ready to study such mechanisms in the MG5_AMC framework. Indeed we have put forward the interpretation of the mono-object signals in the supersymmetry context with a very light gravitino for the LHC, where the technology used would apply for t-channel DM simplified models [2].

The last step towards a unified numerical framework for DM physics consists in implementing indirect detection rates into MADDM. We already worked with the MG5_AMC team in order to include loop-induced processes for indirect detection searches. Such feature had never been implemented so far. Once indirect detection rates are integrated in MADDM v3.0, the unified framework MG5_AMC/MADDM for DM physics will be fully operational.

Appendix A

How to Use MadDM v.2.0

Addition of the direct detection code to the existing MADDM package follows the syntax and philosophy of the previous MADDM version. The code is split up into the `Python` and the `FORTRAN` modules, whereby diagram generation and the structure of folders and files are handled by `Python`, and the numerical calculations are performed by the `FORTRAN` module. As in the previous version, the code does not require any pre-compilation. Simply placing the code within a MG5_AMC folder suffices. However, `Numpy` is now a pre-requisite for running the MADDMv.2.0 code. In order to use the plotting functionality, `Matplotlib` is also required.

In the following we briefly describe how to use the MADDM code relevant for direct detection of DM. We also describe the structure of MADDM v.2.0 and the UFO model conventions for the user input. For a detailed description of the main functions of the MADDM v.2.0 package, see the original paper [3].

As in version 1.0, the main MADDM program can be executed via the `maddm.py` script. The interface will prompt the user to enter the name of the UFO DM model (TAB auto-complete included), a name of the projects, as well as offer a choice of available computations (relic density, DM-nucleon cross sections and recoil rates). The `Python` module of MADDM will then proceed to generate all the relevant scattering/annihilation diagrams and set up the directory structure of the user defined project in `Projects/<projectname>` folder.

The user can choose to enter the DM candidate manually, or to allow MADDM to determine the DM candidate automatically (the code assumes that the lightest particle with the PDG code greater than 25 and zero width is the DM candidate). The code

also offers the user to edit the default parameter card, and pre-set the model parameters before it searches for the DM candidate.

Upon determining the DM candidate, MADDM will attempt to find co-annihilation candidates. The user is prompted to enter the mass splitting within which the co-annihilation partners are deemed to contribute significantly to the calculation of relic density (the default is 10 %).

Finally, the code will prompt the user to edit the `maddm_card.inc` file, which contains all relevant parameters for the numerical calculations. These include, but are not limited to precision parameters for the relic density calculation, nucleon form factors for direct detection, choices of target materials and detector parameters. Upon execution and output of the results, the code will offer the user the option to perform a parameter scan. Alternative to the user interface in `maddm.py` the MADDM code can also be run within any user defined `Python` script. We provide such an example in the `example.py` file.

A.1 Structure of MADDM v.2.0

MADDM v.2.0 follows the directory and file structure of MadDM v.1.0. The `Python` module is arranged into the following simple structure:

- `EffOperators`: A folder containing UFO files for effective operators, which are used to extract the low energy coefficients of the $\chi q \to \chi q$ matrix elements. The UFO files were generated using the FeynRules 2.0 convention (see Section A.2 for more details.).
- `ExpData`: all experimental data used by MADDM is stored in this folder. Currently, only the LUX exclusion bound for the spin-independent DM-nucleon cross section is included. Future versions of MADDM will include a more elaborate database of experimental bounds.
- All user defined projects are automatically output into the `Projects` folder. All numerical calculations and result output is written into the `Projects` folder.
- `Templates` contains necessary `FORTRAN` routines and template files for relic density and direct detection. The structure of the `Template` folder serves as a skeleton for a user defined Project.
- `MGoutput.py` contains a simplified version of the MadGraph output routines, which write the matrix elements into `FORTRAN` files. The routines within

`MGoutput.py` will write the `matrix.f` files, into the `Projects` folder, but will omit writing the additional files which are not necessary for MADDM to run, but are ordinarily written by MadGraph output routines.

- `darkmatter.py` contains the essential part of MADDM `Python` module. The routines within this library contain class definitions for the `darkmatter` objects, as well as numerous functions which find DM candidates and generate the MADDM `FORTRAN` module.
- A self contained example of a MADDM calculation without the use of the user interface can be found in `example.py`. The example calculation goes through the process of importing a user defined UFO model, finding the DM candidate, generating the `FORTRAN` module and calculating the DM-nucleon cross section and relic density.
- `init.py` contains the definitions and functions used by the MADDM user interface.
- `maddm.py` is the main `Python` executable. It will initiate the user interface defined in `init.py` and lead the user through the steps of DM relic density and calculations relevant for DM-nucleon scattering.
- `param_scan_default.py` is a pre-defined parameter scanning `Python` script. The file contains a skeleton of the `Python` code which will scan over DM model parameters and calculate relevant physical quantities. In order to run the parameter scanning script, a minimum of user intervention is required. All places where user input is necessary are marked, and limited to the choice of DM model parameters, number of parameter to scan over and definitions of parameter ranges.

The `FORTRAN` module in each `Projects` folder contains the following 7 subdirectories.

- `Cards`: A directory which contains `param_card.dat`. The structure and placement of the parameter card follows the standard formats of the MG5_AMC framework.
- `Source` directory contains `FORTRAN` code for the DM model, as well as necessary HELAS libraries.
- `include` directory contains various include files for the `FORTRAN` code. The `maddm_card.inc` which contains user defined parameters of the DM relic density and direct detection calculations is located in the `include` folder. Note that any changes in the `maddm_card.inc` file will only be reflected upon the re-compilation of the MADDM `FORTRAN` module.

- Amplitudes for relic abundance and direct detection are saved under `matrix_elements`.
- All results (relic density, cross sections and distributions) are found in `output` directory.
- `src` directory contains the MADDM `FORTRAN` code. The main program is located in the `maddm.f` file.

All the other files in the main directory are executable and perform the following tasks.

- `maddm.x` is the main `FORTRAN` executable. All output of the `maddm.x` will be written into the `output/maddm.out` file by default.
- `make_plots` is a `Python` script containing calls to plotting MADDM plotting routines. All calls are commented out by default. Note that it is necessary to install both `Numpy` and `Matplotlib` in order for plotting functionality to work in MADDM.
- `plotting.py` is a library of user friendly plotting functions. For examples of how to use plotting functionality of MADDM, see `make_plots`. Function definitions use libraries from both `Numpy` and `Matplotlib`.

A.2 UFO Model Conventions

Now we proceed to discuss some important conventions on UFO files required by the MADDMv.2.0 code. We implemented the projection operator formalism in MADDM v.2.0 via a recent feature of MG5_AMC which allows the user to merge two UFO model files. We provide UFO models with vertices of effective operators as a part of the MADDM code, so that an interference term between the matrix elements of the user defined model, and the effective operators can be extracted. The vertices are then automatically added to the DM model provided by the user during the execution of the code. The merging procedure of MG5_AMC is sensitive to the UFO convention and the user should take special care to make sure that the DM model used in MADDM is compatible with the effective operator models embedded in MADDM v.2.0[1]. We have generated our set of effective operators with FeynRules 2.0. We advise the user to test the merging procedure in MG5_AMC before running MADDM in order to avoid UFO conflicts. Using this UFO convention, the DM particle should be defined as

[1]The statement is relevant only for direct/directional detection. Relic density will proceed correctly without regard for the UFO version.

```
DM = Particle(pdg_code = pdg code,
              ...
              spin = 1,
              mass = Param.DMMASS,
              width = Param.WDM,
              ...)
```

in case of a real scalar DM (for example). In this convention, **it is compulsory to assign a PDG code to the DM particle as well as a mass and a width**. Next, the mass and width block parameters have to match the following template:

```
DMMASS = Parameter(name = 'DMMASS',
                   ...
                   lhablock = 'MASS',
                   lhacode = [ pdg code ])

WDM = Parameter(name = 'WDM',
                ...
                lhablock = 'DECAY',
                lhacode = [ pdg code ])
```

where the `lhablock` and `lhacode` parameters should be exactly like the template when replacing the PDG code by the PDG code of the DM particle. Note also that we cannot use `mdm` for the DM mass name due to conflict with internal MADDM parameters. For the same reason, if the user wants to define new coupling orders, the following ones should not be used : `SIEFFS`, `SIEFFF`, `SIEFFV`, `SDEFFF`, `SDEFFV`. These coupling orders ensure the internal proper functioning of MADDM.

Finally, the user should **make sure that direct detection diagrams have a QED order lower or equal to 2** since MADDM generates diagrams with the `QED=2` flag.

Appendix B

Mediator width

As supplementary material of Chapter 4, Fig. B.1 shows the relative mediator width Γ_Y/m_Y in the (g_t, g_X) plane for different mass choices. The magnitude of the mediator width depends on the hierarchy among the different decay processes *i.e.* $t\bar{t}$, $X\bar{X}$, gg and $\gamma\gamma$. Diphoton channel is negligible compared to the others and will not be discussed. Figure B.1 shows that the Y_0 resonance can be considered as narrow (*i.e.* $\Gamma_Y/m_Y < 0.03$) when only the gg decay mode is involved. As soon as $t\bar{t}$ and $X\bar{X}$ decay channels are opened, the ratio Γ_Y/m_Y grows quickly, reaching 20% for $g_t, g_X \sim 2$. The narrow width approximation is valid below couplings of $\mathcal{O}(1)$. Figure B.2 shows the relative mediator width Γ_Y/m_Y in the (m_Y, m_X) plane for different coupling choices. When $g_t, g_X \leq 1$, Γ_Y/m_Y never exceeds 10% and the narrow width approximation is reliable for a wide region of the parameter space. In the kinematic regions where Y_0 decays to X and/or top quarks is allowed, increase in either g_t or g_X quickly leads to Γ_Y/m_Y ratio above 20%.

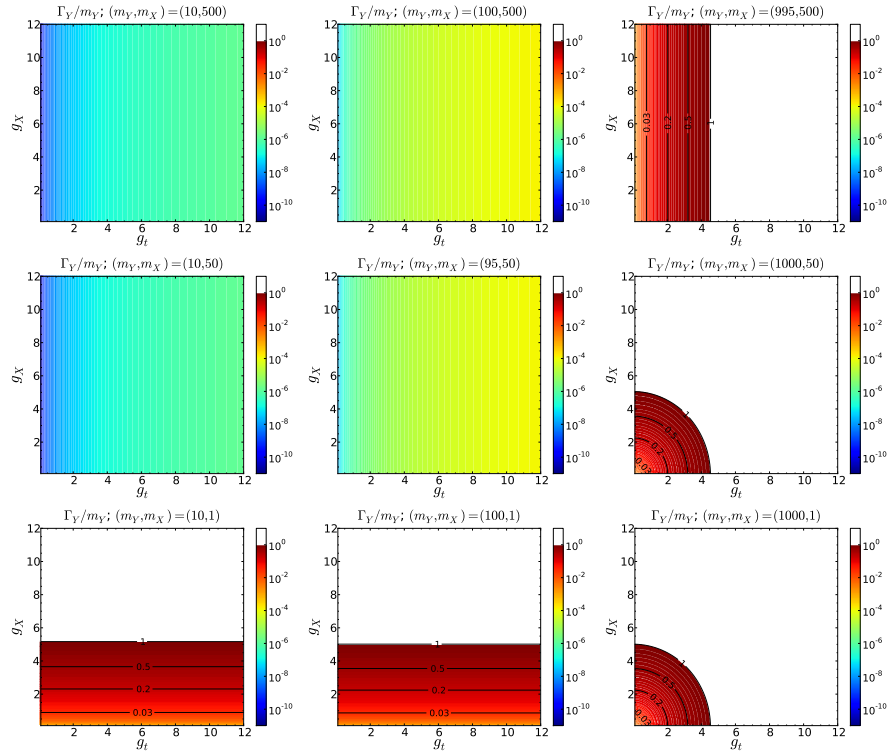


Figure B.1: Γ_Y/m_Y in the (g_t, g_X) plane for different mass choices (expressed in GeV). The colour bar shows the numerical value of the width to mass ratio.

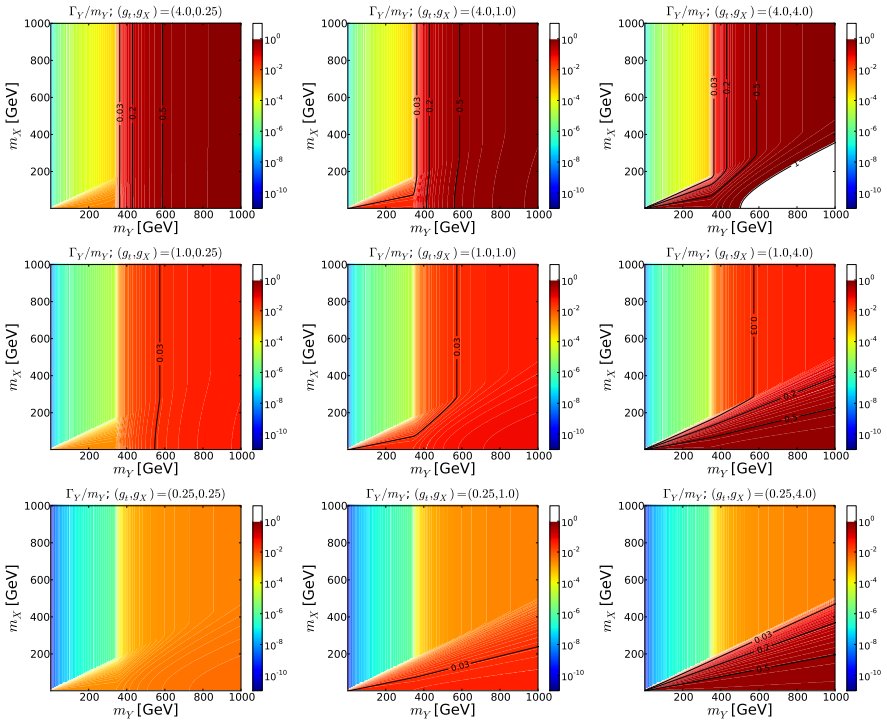


Figure B.2: Γ_Y/m_Y in the (m_Y, m_X) plane for different coupling choices. The colour bar shows the numerical value of the width to mass ratio.

Appendix C

Recasting of LHC searches within the MADANALYSIS 5 framework

In this appendix, we detail the implementation, within the MADANALYSIS 5 framework [169–171], of the two DM searches that we have investigated in this work. More precisely, this consists of the CMS-B2G-14-004 analysis [119] that probes final states comprised of a top-antitop system produced in association with a pair of invisible DM particles (see Section C.1) and the CMS-EXO-12-048 analysis [192] related to the production of a pair of DM particles together with a hard jet (see Section C.2). Both recasting codes have been validated within the version 1.3 of MADANALYSIS 5, although the monojet search reimplementation is also compatible with the version 1.2 of the program. The simulation of the detector response is performed with the standard DELPHES 3 package that we have run from the MADANALYSIS 5 platform. In the monojet case, we have used the standard CMS detector parametrisation that is the shipped with MADANALYSIS 5, while in the top-antitop plus missing energy case, we have designed a dedicated detector card. For both setups, jets are reconstructed on the basis of the anti-k_T algorithm [112] with a radius parameter set to 0.5, as implemented in FASTJET [113].

The validation of both our reimplementations is based on material provided by CMS. Two UFO models [85], one for each of the recast analyses, have been shared so that we have been allowed to generate specific DM signals for which CMS has released public cutflow charts and differential distributions. Using MG5_AMC [78] (with the

leading order set of CTEQ6 parton densities [218]) and PYTHIA 6 [96] (with the Z_2^* tune [219] for the description of the underlying events) for the simulation of the hard scattering process and of the parton showering and hadronisation, respectively, we have generated signal events that have been analyzed with MADANALYSIS 5. Our results have been confronted to the CMS official numbers, which has allowed us to assess the validity of our recasting codes. Our simulation procedure moreover includes the generation of matrix elements containing up to two extra jets that we have merged according to the MLM prescription [220, 221], the merging scale being set to 40 GeV.

All PYTHIA 6, DELPHES 3 and MG5_AMC configuration cards can be downloaded from the public analysis database webpage of MADANALYSIS 5,
`http://madanalysis.irmp.ucl.ac.be/wiki/PublicAnalysisDatabase`,
while the recasting C++ codes associated with the CMS-EXO-12-048 and CMS-B2G-14-004 analyses can be found on INSPIRE [222, 223].

C.1 The CMS top-antitop plus missing energy search (CMS-B2G-14-004)

In order to validate our reimplementation of the CMS-B2G-14-004 search in MADANALYSIS 5, we focus on a new physics model that features the production a pair of DM particle X of mass $m_X = 1$ GeV in association with a top-antitop pair via a four-fermion interaction. The CMS event selection strategy requires a large amount of missing transverse energy, a single isolated lepton and multiple jets, and uses $19.7\ \text{fb}^{-1}$ of proton-proton collision data recorded at a centre-of-mass energy of $\sqrt{s} = 8\ \text{TeV}$.

The CMS-B2G-14-004 analysis relies on single electron and muon triggers, with lower p_T thresholds of 27 GeV and 24 GeV respectively, and the reconstructed electron (muon) candidate is imposed to be isolated in such a way that the sum of the transverse momenta of all objects lying in a cone of radius $R = 0.3$ centered on the lepton has to be smaller than 10% (12%) of the lepton p_T. Event preselection finally requires that the lepton p_T is larger than 30 GeV and pseudorapidity $|\eta|$ is smaller than 2.5 (2.1 for muons). It additionally demands the presence of at least three jets of $p_T > 30$ GeV and $|\eta| < 2.4$ with one of them being b-tagged, as well as missing energy $\not{E}_T > 160$ GeV. The signal region is defined by selecting events with a large amount of missing transverse energy $\not{E}_T > 320$ for which the transverse mass M_T that is constructed from the lepton and the missing energy is larger than 160 GeV. Moreover, the missing transverse momentum and the two leading jets are asked to

	Selection step	CMS	$\epsilon_i^{\rm CMS}$	MA5	$\epsilon_i^{\rm MA5}$	$\delta_i^{\rm rel}$
0	Nominal	224510		224510		
1	Preselection			15468.5	0.069	
2	$\not{E}_T > 320$ GeV	4220.8		4579.8	0.296	
3	$M_T > 160$ GeV	3390.1	0.803	3648.2	0.797	0.75%
4	$\Delta\Phi(j_{1,2}, \not{E}_T) > 1.2$	2963.5	0.874	3124.3	0.856	2.06%
5	$M_{T2}^W > 200$ GeV	2267.6	0.765	2403	0.769	-0.52%

Table C.1: Comparison of results obtained with our MADANALYSIS 5 reimplementation (MA5) and those provided by the CMS collaboration (CMS). The efficiencies are defined in Eq. (C.1) and the relative difference between the CMS and the MADANALYSIS 5 results $\delta_i^{\rm rel}$ in Eq. (C.2).

be well separated in azimuth, $\Delta\Phi\left(j_{1,2}, \not{E}_T\right) > 1.2$, and the M_{T2}^W variable [224] is enforced to be greater than 200 GeV.

In Table C.1, we confront the cutflow chart that has been obtained with MADANALYSIS 5 to the official results of CMS for the benchmark scenario under consideration. For each step of the selection, we have calculated the related efficiency defined as

$$\epsilon_i = \frac{n_i}{n_{i-1}} \,, \tag{C.1}$$

where n_i and n_{i-1} mean the event number after and before the considered cut, respectively. The *relative difference* information given in the table corresponds to the difference between the MADANALYSIS 5 and the CMS efficiencies, normalized to the CMS result,

$$\delta_i^{\rm rel} = 1 - \frac{\epsilon_i^{\rm MA5}}{\epsilon_i^{\rm CMS}} \,. \tag{C.2}$$

An agreement at the percent level has been found all over the selection procedure. Moreover, we compare several (normalized) differential distributions as calculated with MADANALYSIS 5 when all selection steps but the one related to the represented kinematic variable are included with the public CMS results in Fig. C.1. A very good agreement can again be observed.

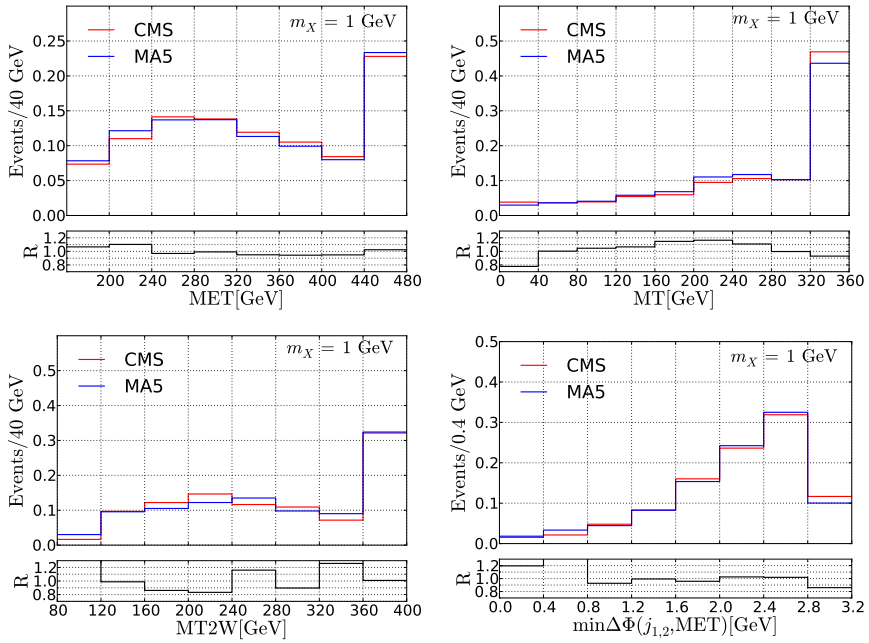


Figure C.1: Missig transverse energy, M_T, M_{T2}^W and $\Delta\Phi\left(j_{1,2}, \not{E}_T\right)$ spectrum as obtained with MADANALYSIS 5 (blue) once all selection steps but the one related to the represented variable are applied, compared to the CMS official results (red).

C.2 The CMS monojet search (CMS-EXO-12-048)

The validation of our implementation of the CMS-EXO-12-048 search in MADANALYSIS 5 has been achieved on the basis of a benchmark scenario that is inspired by Refs. [70, 71, 225, 226]. In this context, monojet events arise from the associated production of a pair of invisible Dirac fermions of mass of 1 GeV with at least one hard jet. The interactions of the DM particle with the Standard Model are mediated by a new gauge boson Z' of mass and width of 40 TeV and 10 GeV respectively, and all new physics interactions have been assumed to have a vector coupling structure and a strength set equal to 1. Concerning our signal simulation setup, we have imposed that all parton-level jets have a transverse momentum p_T larger than 20 GeV and that the leading jet has a $p_T > 80$ GeV.

The CMS monojet search relies on an integrated luminosity of 19.7 fb^{-1} of proton-proton collisions at a centre-of-mass energy of $\sqrt{s} = 8$ TeV. It focuses on a signal

	Selection step	CMS	$\epsilon_i^{\rm CMS}$	MA5	$\epsilon_i^{\rm MA5}$	$\delta_i^{\rm rel}$
0	Nominal	84653.7		84653.7		
1	One hard jet	50817.2	0.6	53431.28	0.631	5.2%
2	At most two jets	36061	0.7096	38547.75	0.721	1.61%
3	Requirements if two jets	31878.1	0.884	34436.35	0.893	1.02%
4	Muon veto	31878.1	1	34436.35	1.000	0
5	Electron veto	31865.1	1	34436.35	1.000	0
6	Tau veto	31695.1	0.995	34397.54	0.998	0.3%
	$\not{E}_T > 250$ GeV	8687.22	0.274	7563.04	0.219	20.00%
	$\not{E}_T > 300$ GeV	5400.51	0.621	4477.67	0.592	4.66%
	$\not{E}_T > 350$ GeV	3394.09	0.628	2813.70	0.628	0.00%
	$\not{E}_T > 400$ GeV	2224.15	0.6553	1753.71	0.623	4.93%
	$\not{E}_T > 450$ GeV	1456.02	0.654	1110.92	0.633	3.21%
	$\not{E}_T > 500$ GeV	989.806	0.679	722.83	0.650	4.27%
	$\not{E}_T > 550$ GeV	671.442	0.678	487.54	0.674	0.59%

Table C.2: Comparison of results obtained with our MADANALYSIS 5 reimplementation (MA5) and those provided by the CMS collaboration (CMS). The efficiencies are defined in Eq. (C.1) and the relative difference between the CMS and the MADANALYSIS 5 results $\delta_i^{\rm rel}$ in Eq. (C.2).

containing a very hard jet with a transverse momentum satisfying $p_T > 110$ GeV and a pseudorapidity smaller than 4.5 in absolute value. A second jet is moreover allowed, provided that its transverse momentum is larger than 30 GeV, its pseudorapidity satisfies $|\eta| < 4.5$ and if it is well separated from the first jet by 2.5 radians in azimuth. Events featuring more than two jets (with $p_T > 30$ GeV and $|\eta| < 4.5$), isolated electrons or muons with a transverse momentum $p_T > 10$ GeV or hadronically decaying tau leptons with a transverse momentum $p_T > 20$ GeV and a pseudorapidity satisfying $|\eta| < 2.3$ are discarded. The analysis then contains seven inclusive signal regions in which the missing energy $\not{E}_T$ is required to be above specific thresholds of 250, 300, 350, 400, 450, 500 and 550 GeV respectively.

The selection strategy of the CMS monojet analysis thus consists of six preselection cuts followed by one region-dependent cut, when we ignore the first two requirements of the analysis related to the cleaning of the events from the detector noise that cannot be handled with DELPHES 3. For the benchmark scenario under consideration, we compare the results that have been derived with our MADANALYSIS 5 reimplementation with those provided by the CMS collaboration in Table C.2.

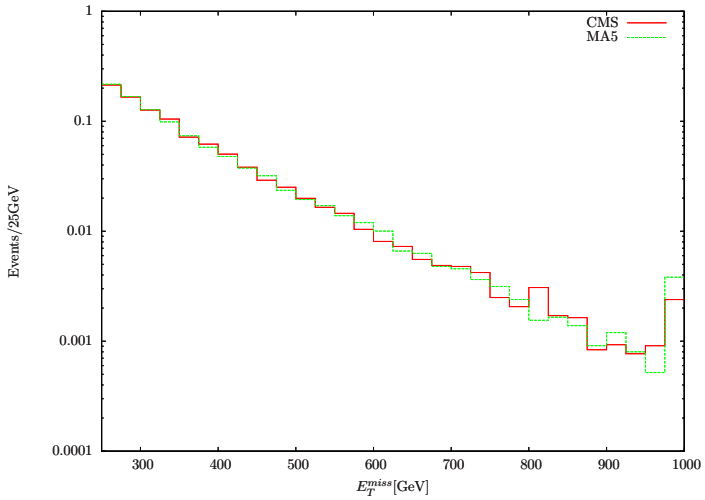


Figure C.2: Missing energy spectrum as obtained with MADANALYSIS 5 (green dashed line) after the CMS-EXO-12-048 monojet preselection, compared to the CMS official results (red solid line). The last bin is the overflow bin.

We have found that all selection steps are properly described by our implementation, with the exception the missing energy selection $\not{E}_T > 250$ GeV for which a disagreement of about 20% has been observed. It is however not uncommon that low missing energy is difficult to simulate with a fast-simulation of the detector based on DELPHES 3. We have verified that for missing energy values of interest, the description of the missing energy agree relatively well with CMS, as illustrated in Fig. C.2 where we compare, for a benchmark scenario where the Z' mass has been set to 900 GeV, the missing energy distribution as obtained by CMS to the one derived with MADANALYSIS 5.

Appendix D

Combined collider constraints

In this appendix we show the individual constraints derived from the LHC Run I results on the simplified top-philic DM model of Chapter 4. Figures D.1, D.2 and D.3 show the results of a four-dimensional parameter scan, uniform on the linear scale. Figure D.1 shows the points excluded by monojet and $t\bar{t} + \not{E}_T$ constraints. The resonant $t\bar{t}$ and four top searches constraints are shown in Fig. D.2, while the diphoton constraints appear on Fig. D.3. The results assume couplings smaller than 2π and $\Gamma_Y/m_Y < 0.5$, with no constraints from astrophysics or cosmology being imposed. In case of resonant $t\bar{t}$ and four top, we only show the 95% CL exclusion as the $t\bar{t}$ and four top results have not been obtained using a recast LHC analysis.

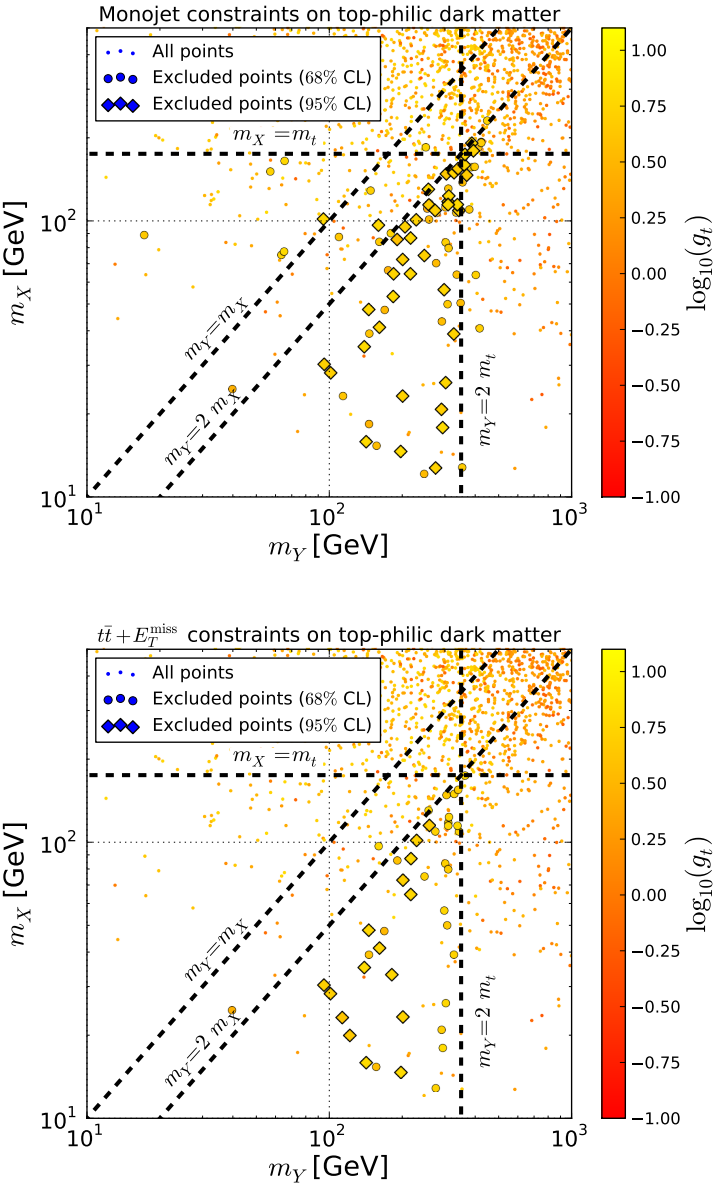


Figure D.1: Monojet and $t\bar{t} + \not{E}_T$ constraints.

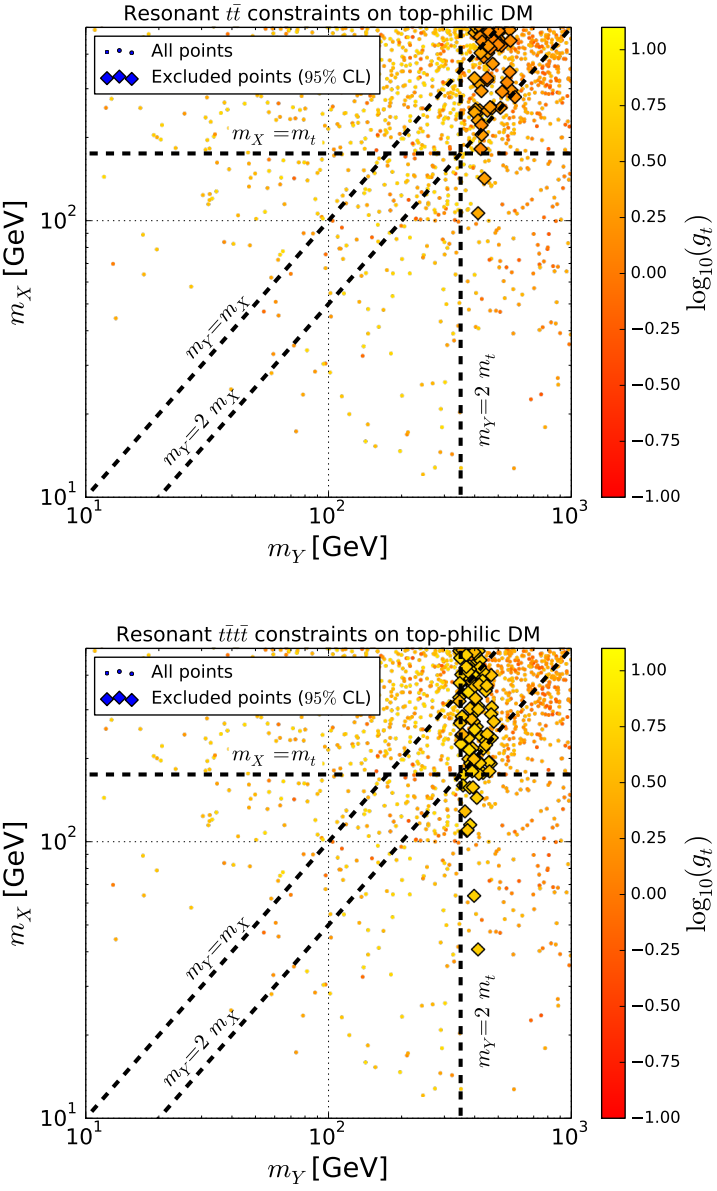


Figure D.2: Resonant $t\bar{t}$ and four top constraints.

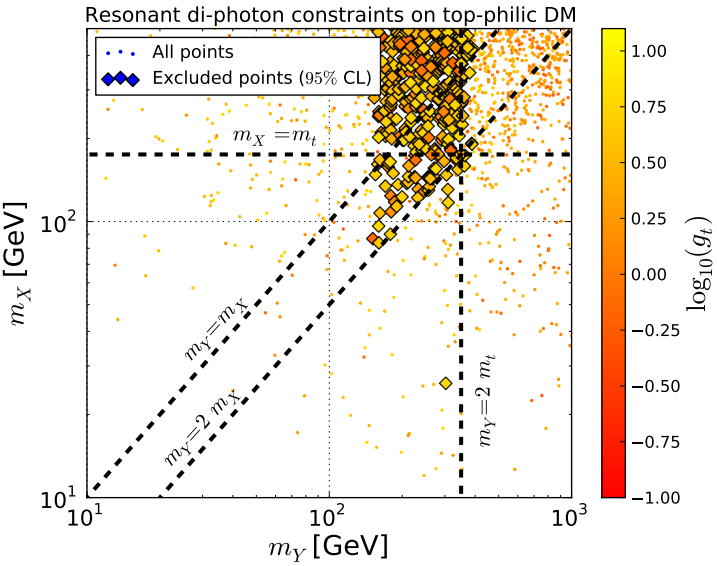


Figure D.3: Diphoton constraints.

Bibliography

[1] M. Backovic, M. Kramer, F. Maltoni, A. Martini, K. Mawatari, and M. Pellen, *Higher-order QCD predictions for dark matter production at the LHC in simplified models with s-channel mediators*, *Eur. Phys. J.* **C**75 (2015), no. 10 482, [arXiv:1508.05327].

[2] F. Maltoni, A. Martini, K. Mawatari, and B. Oexl, *Signals of a superlight gravitino at the LHC*, *JHEP* **0**4 (2015) 021, [arXiv:1502.01637].

[3] M. Backovic, A. Martini, O. Mattelaer, K. Kong, and G. Mohlabeng, *Direct Detection of Dark Matter with MadDM v.2.0*, *Phys. Dark Univ.* **9**-10 (2015) 37–50, [arXiv:1505.04190].

[4] C. Arina et al., *A comprehensive approach to dark matter studies: exploration of simplified top-philic models*, *JHEP* **1**1 (2016) 111, [arXiv:1605.09242].

[5] R. Ferraro, *From Æther Theory to Special Relativity*, in *Springer Handbook of Spacetime* (A. Ashtekar and V. Petkov, eds.), p. 3. 2014.

[6] G. Bertone and D. Hooper, *A History of Dark Matter*, *Submitted to: Rev. Mod. Phys.* (2016) [arXiv:1605.04909].

[7] G. Rajasekaran, *The Story of the Neutrino*, arXiv:1606.08715.

[8] K. Garrett and G. Duda, *Dark Matter: A Primer*, *Adv. Astron.* **2**011 (2011) 968283, [arXiv:1006.2483].

[9] J. Einasto, *Dark Matter*. Astronomy and Astrophysics (Eolss), 2010.

[10] M. S. Roberts and R. N. Whitehurst, *The rotation curve and geometry of M31 at large galactocentric distances.*, *ApJ* **2**01 (Oct., 1975) 327–346.

[11] P. Peter and P. Uzan, *Cosmologie primordiale*. Belin, 2012.

[12] **P**lanck Collaboration, P. A. R. Ade et al., *Planck 2015 results. XIII. Cosmological parameters*, *Astron. Astrophys.* **5**94 (2016) A13, [arXiv:1502.01589].

[13] B. D. Fields, *The primordial lithium problem*, *Ann. Rev. Nucl. Part. Sci.* **6**1 (2011) 47–68, [arXiv:1203.3551].

[14] S. Q. Hou, J. J. He, A. Parikh, D. Kahl, C. A. Bertulani, T. Kajino, G. J. Mathews, and G. Zhao, *Non-extensive Statistics to the Cosmological Lithium Problem*, *Astrophys. J.* **8**34 (2017), no. 2 165, [arXiv:1701.04149].

[15] G. Bertone, D. Hooper, and J. Silk, *Particle dark matter: Evidence, candidates and constraints*, *Phys. Rept.* **4**05 (2005) 279–390, [hep-ph/0404175].

[16] D. Hooper, *Particle Dark Matter*, in *Proceedings of Theoretical Advanced Study Institute in Elementary Particle Physics on The dawn of the LHC era (TASI 2008): Boulder, USA, June 2-27, 2008*, pp. 709–764, 2010. arXiv:0901.4090.

[17] G. B. Gelmini, *TASI 2014 Lectures: The Hunt for Dark Matter*, in *Theoretical Advanced Study Institute in Elementary Particle Physics: Journeys Through the Precision Frontier: Amplitudes for Colliders (TASI 2014) Boulder, Colorado, June 2-27, 2014*, 2015. arXiv:1502.01320.

[18] K. Griest and D. Seckel, *Three exceptions in the calculation of relic abundances*, *Phys.Rev.* **D**43 (1991) 3191–3203.

[19] Mather, J. C. and others, *A preliminary measurement of the cosmic microwave background spectrum by the Cosmic Background Explorer (COBE) satellite*, *Astrophysical Journal* **3**54 (may, 1990) L37–L40.

[20] **W**MAP Collaboration, C. L. Bennett et al., *First year Wilkinson Microwave Anisotropy Probe (WMAP) observations: Preliminary maps and basic results*, *Astrophys. J. Suppl.* **1**48 (2003) 1–27, [astro-ph/0302207].

[21] G. R. Blumenthal, S. M. Faber, J. R. Primack, and M. J. Rees, *Formation of galaxies and large-scale structure with cold dark matter*, *Nature.* **3**11 (Oct., 1984) 517–525.

[22] V. Springel, S. D. M. White, A. R. Jenkins, C. S. Frenk, N. Yoshida, L. Gao, J. Navarro, R. Thacker, D. Croton, J. Helly, J. A. Peacock, S. Cole, P. Thomas, H. Couchman, A. A. Evrard, J. Colberg, and F. Pearce, *Simulations of the formation, evolution and clustering of galaxies and quasars.*, *Nature.* **4**35 (June, 2005) 629–636.

[23] M. E. Peskin and D. V. Schroeder, *An Introduction to Quantum Field Theory; 1995 ed.* Westview, Boulder, CO, 1995. Includes exercises.

[24] G. Ridolfi, *An introduction to the Standard Model of Electroweak Interactions*, *Lecture notes* (2002).

[25] F. Englert and R. Brout, *Broken Symmetry and the Mass of Gauge Vector Mesons*, *Phys.Rev.Lett.* **1**3 (1964) 321–323.

[26] P. W. Higgs, *Broken Symmetries and the Masses of Gauge Bosons*, *Phys.Rev.Lett.* **1**3 (1964) 508–509.

[27] **C**MS Collaboration, S. Chatrchyan et al., *Observation of a new boson at a mass of 125 GeV with the CMS experiment at the LHC*, *Phys. Lett.* **B**716 (2012) 30–61, [arXiv:1207.7235].

[28] **A**TLAS Collaboration, G. Aad et al., *Observation of a new particle in the search for the Standard Model Higgs boson with the ATLAS detector at the LHC*, *Phys. Lett.* **B**716 (2012) 1–29, [arXiv:1207.7214].

[29] C. Csáki and P. Tanedo, *Beyond the Standard Model*, in *Proceedings, 2013 European School of High-Energy Physics (ESHEP 2013): Paradfurdo, Hungary, June 5-18, 2013*, pp. 169–268, 2015. arXiv:1602.04228.

[30] M. Lindner, T. Ohlsson, and G. Seidl, *Seesaw mechanisms for Dirac and Majorana neutrino masses*, *Phys. Rev.* **D**65 (2002) 053014, [hep-ph/0109264].

[31] R. D. Peccei and H. R. Quinn, *CP Conservation in the Presence of Instantons*, *Phys. Rev. Lett.* **3**8 (1977) 1440–1443.

[32] A. Ringwald, *Alternative dark matter candidates: Axions*, *PoS* **N**OW2016 (2016) 081, [arXiv:1612.08933].

[33] M. Kawasaki and K. Nakayama, *Axions: Theory and Cosmological Role*, *Ann. Rev. Nucl. Part. Sci.* **6**3 (2013) 69–95, [arXiv:1301.1123].

[34] P. W. Graham, I. G. Irastorza, S. K. Lamoreaux, A. Lindner, and K. A. van Bibber, *Experimental Searches for the Axion and Axion-Like Particles*, *Ann. Rev. Nucl. Part. Sci.* **6**5 (2015) 485–514, [arXiv:1602.00039].

[35] F. Della Valle, A. Ejlli, U. Gastaldi, G. Messineo, E. Milotti, R. Pengo, G. Ruoso, and G. Zavattini, *The PVLAS experiment: measuring vacuum magnetic birefringence and dichroism with a birefringent Fabry–Perot cavity*, *Eur. Phys. J.* **C**76 (2016), no. 1 24, [arXiv:1510.08052].

[36] **C**AST Collaboration, M. Arik et al., *New solar axion search using the CERN Axion Solar Telescope with ^{4}He filling*, *Phys. Rev.* **D**92 (2015), no. 2 021101, [arXiv:1503.00610].

[37] **O**SQAR Collaboration, P. Pugnat et al., *First results from the OSQAR photon regeneration experiment: No light shining through a wall*, *Phys. Rev.* **D**78 (2008) 092003, [arXiv:0712.3362].

[38] J. Kersten and O. Lebedev, *Gravitino Dark Matter in Gravity Mediation*, *Phys. Lett.* **B**678 (2009) 481–484, [arXiv:0905.3711].

[39] K. Jedamzik, M. Lemoine, and G. Moultaka, *Gravitino dark matter in gauge mediated supersymmetry breaking*, *Phys. Rev.* **D**73 (2006) 043514, [hep-ph/0506129].

[40] R. Arya, N. Mahajan, and R. Rangarajan, *Gravitino production in a thermal Universe revisited*, *Phys. Lett.* **B**772 (2017) 258–264, [arXiv:1608.03386].

[41] T. Plehn, *Dark matter from a Particle Theorist's perspective*, *Lectures Notes* (2017).

[42] A. W. Strong and I. V. Moskalenko, *The galprop program for cosmic ray propagation: new developments*, in *Proceedings, 26th International Cosmic Ray Conference, August 17-25, 1999, Salt Lake City: Invited, Rapporteur, and Highlight Papers*, p. 255, 1999. astro-ph/9906228. [4,255(1999)].

[43] C. Evoli, D. Gaggero, A. Vittino, G. Di Bernardo, M. Di Mauro, A. Ligorini, P. Ullio, and D. Grasso, *Cosmic-ray propagation with* DRAGON2*: I. numerical solver and astrophysical ingredients*, *JCAP* **1**702 (2017), no. 02 015, [arXiv:1607.07886].

[44] J. M. Gaskins, *A review of indirect searches for particle dark matter*, *Contemp. Phys.* **5**7 (2016), no. 4 496–525, [arXiv:1604.00014].

[45] M. Fornasa and A. M. Green, *Self-consistent phase-space distribution function for the anisotropic dark matter halo of the Milky Way*, *Phys. Rev.* **D**89 (2014), no. 6 063531, [arXiv:1311.5477].

[46] **F**ermi-LAT Collaboration, M. Ackermann et al., *Search for Gamma-ray Spectral Lines with the Fermi Large Area Telescope and Dark Matter Implications*, *Phys. Rev.* **D**88 (2013) 082002, [arXiv:1305.5597].

[47] **P**AMELA Collaboration, O. Adriani et al., *Cosmic-Ray Positron Energy Spectrum Measured by PAMELA*, *Phys. Rev. Lett.* **1**11 (2013) 081102, [arXiv:1308.0133].

[48] **A**MS Collaboration, L. Accardo et al., *High Statistics Measurement of the Positron Fraction in Primary Cosmic Rays of 0.5–500 GeV with the Alpha Magnetic Spectrometer on the International Space Station*, *Phys. Rev. Lett.* **1**13 (2014) 121101.

[49] V. Vitale, A. Morselli, and for the Fermi/LAT Collaboration, *Indirect Search for Dark Matter from the center of the Milky Way with the Fermi-Large Area Telescope*, *ArXiv e-prints* (Dec., 2009) [arXiv:0912.3828].

[50] L. Goodenough and D. Hooper, *Possible Evidence For Dark Matter Annihilation In The Inner Milky Way From The Fermi Gamma Ray Space Telescope*, arXiv:0910.2998.

[51] **I**ceCube Collaboration, M. G. Aartsen et al., *Search for annihilating dark matter in the Sun with 3 years of IceCube data*, *Eur. Phys. J.* **C**77 (2017), no. 3 146, [arXiv:1612.05949].

[52] **A**NTARES Collaboration, S. Adrian-Martinez et al., *Limits on Dark Matter Annihilation in the Sun using the ANTARES Neutrino Telescope*, *Phys. Lett.* **B**759 (2016) 69–74, [arXiv:1603.02228].

[53] **L**UX Collaboration, D. S. Akerib et al., *Results from a search for dark matter in the complete LUX exposure*, *Phys. Rev. Lett.* **1**18 (2017), no. 2 021303, [arXiv:1608.07648].

[54] **X**ENON100 Collaboration, E. Aprile et al., *Dark Matter Results from 225 Live Days of XENON100 Data*, *Phys. Rev. Lett.* **1**09 (2012) 181301, [arXiv:1207.5988].

[55] **X**ENON Collaboration, E. Aprile et al., *First Dark Matter Search Results from the XENON1T Experiment*, arXiv:1705.06655.

[56] **L**Z Collaboration, D. N. McKinsey, *The LZ dark matter experiment*, *J. Phys. Conf. Ser.* **7**18 (2016), no. 4 042039.

[57] **S**uperCDMS Collaboration, R. Agnese et al., *Improved WIMP-search reach of the CDMS II germanium data*, *Phys. Rev.* **D**92 (2015), no. 7 072003, [arXiv:1504.05871].

[58] **S**uperCDMS Collaboration, R. Agnese et al., *New Results from the Search for Low-Mass Weakly Interacting Massive Particles with the CDMS Low Ionization Threshold Experiment*, *Phys. Rev. Lett.* **1**16 (2016), no. 7 071301, [arXiv:1509.02448].

[59] **C**RESST Collaboration, G. Angloher et al., *Dark-Photon Search using Data from CRESST-II Phase 2*, *Eur. Phys. J.* **C**77 (2017), no. 5 299, [arXiv:1612.07662].

[60] **E**DELWEISS Collaboration, E. Armengaud et al., *Constraints on low-mass WIMPs from the EDELWEISS-III dark matter search*, *JCAP* **1**605 (2016), no. 05 019, [arXiv:1603.05120].

[61] **E**URECA Collaboration, G. Angloher et al., *EURECA Conceptual Design Report*, *Phys. Dark Univ.* **3** (2014) 41–74.

[62] R. Bernabei, *The DAMA project*, *Int. J. Mod. Phys.* **A**31 (2016), no. 31 1642001.

[63] L. Evans and P. Bryant, *LHC Machine*, *JINST* **3** (2008) S08001.

[64] **A**TLAS Collaboration, G. Aad et al., *The ATLAS Experiment at the CERN Large Hadron Collider*, *JINST* **3** (2008) S08003.

[65] **C**MS Collaboration, S. Chatrchyan et al., *The CMS Experiment at the CERN LHC*, *JINST* **3** (2008) S08004.

[66] **L**HC New Physics Working Group Collaboration, D. Alves, *Simplified Models for LHC New Physics Searches*, *J. Phys.* **G**39 (2012) 105005, [arXiv:1105.2838].

[67] J. Abdallah et al., *Simplified Models for Dark Matter and Missing Energy Searches at the LHC*, arXiv:1409.2893.

[68] S. Malik et al., *Interplay and Characterization of Dark Matter Searches at Colliders and in Direct Detection Experiments*, 2014. arXiv:1409.4075.

[69] D. Abercrombie, N. Akchurin, E. Akilli, J. A. Maestre, B. Allen, et al., *Dark Matter Benchmark Models for Early LHC Run-2 Searches: Report of the ATLAS/CMS Dark Matter Forum*, arXiv:1507.00966.

[70] J. Goodman, M. Ibe, A. Rajaraman, W. Shepherd, T. M. P. Tait, and H.-B. Yu, *Constraints on Light Majorana dark Matter from Colliders*, *Phys. Lett.* **B**695 (2011) 185–188, [arXiv:1005.1286].

[71] Y. Bai, P. J. Fox, and R. Harnik, *The Tevatron at the Frontier of Dark Matter Direct Detection*, *JHEP* **1**2 (2010) 048, [arXiv:1005.3797].

[72] P. J. Fox, R. Harnik, J. Kopp, and Y. Tsai, *Missing Energy Signatures of Dark Matter at the LHC*, *Phys. Rev.* **D**85 (2012) 056011, [arXiv:1109.4398].

[73] I. M. Shoemaker and L. Vecchi, *Unitarity and Monojet Bounds on Models for DAMA, CoGeNT, and CRESST-II*, *Phys. Rev.* **D**86 (2012) 015023, [arXiv:1112.5457].

[74] G. Busoni, A. De Simone, E. Morgante, and A. Riotto, *On the Validity of the Effective Field Theory for Dark Matter Searches at the LHC*, *Phys. Lett.* **B**728 (2014) 412–421, [arXiv:1307.2253].

[75] O. Buchmueller, M. J. Dolan, and C. McCabe, *Beyond Effective Field Theory for Dark Matter Searches at the LHC*, *JHEP* **0**1 (2014) 025, [arXiv:1308.6799].

[76] C. Englert, M. McCullough, and M. Spannowsky, *S-Channel Dark Matter Simplified Models and Unitarity*, *Phys. Dark Univ.* **1**4 (2016) 48–56, [arXiv:1604.07975].

[77] A. Alloul, N. D. Christensen, C. Degrande, C. Duhr, and B. Fuks, *FeynRules 2.0 - A complete toolbox for tree-level phenomenology*, *Comput. Phys. Commun.* **1**85 (2014) 2250–2300, [arXiv:1310.1921].

[78] J. Alwall, R. Frederix, S. Frixione, V. Hirschi, F. Maltoni, O. Mattelaer, H. S. Shao, T. Stelzer, P. Torrielli, and M. Zaro, *The automated computation of tree-level and next-to-leading order differential cross sections, and their matching to parton shower simulations*, *JHEP* **0**7 (2014) 079, [arXiv:1405.0301].

[79] R. Frederix and S. Frixione, *Merging meets matching in MC@NLO*, *JHEP* **1**2 (2012) 061, [arXiv:1209.6215].

[80] J. Wang, C. S. Li, D. Y. Shao, and H. Zhang, *Next-to-leading order QCD predictions for the signal of Dark Matter and photon associated production at the LHC*, *Phys.Rev.* **D**84 (2011) 075011, [arXiv:1107.2048].

[81] F. P. Huang, C. S. Li, J. Wang, and D. Y. Shao, *Searching for the signal of dark matter and photon associated production at the LHC beyond leading order*, *Phys.Rev.* **D**87 (2013) 094018, [arXiv:1210.0195].

[82] P. J. Fox and C. Williams, *Next-to-Leading Order Predictions for Dark Matter Production at Hadron Colliders*, *Phys.Rev.* **D**87 (2013), no. 5 054030, [arXiv:1211.6390].

[83] U. Haisch, F. Kahlhoefer, and E. Re, *QCD effects in mono-jet searches for dark matter*, *JHEP* **1**312 (2013) 007, [arXiv:1310.4491].

[84] M. Song, G. Li, W.-G. Ma, R.-Y. Zhang, and J.-Y. Guo, *Dark matter pair associated with a W boson production at the LHC in next-to-leading order QCD*, *JHEP* **1**409 (2014) 069, [arXiv:1403.2142].

[85] C. Degrande, C. Duhr, B. Fuks, D. Grellscheid, O. Mattelaer, and T. Reiter, *UFO - The Universal FeynRules Output*, *Comput. Phys. Commun.* **1**83 (2012) 1201–1214, [arXiv:1108.2040].

[86] P. de Aquino, W. Link, F. Maltoni, O. Mattelaer, and T. Stelzer, *ALOHA: Automatic Libraries Of Helicity Amplitudes for Feynman Diagram Computations*, *Comput.Phys.Commun.* **1**83 (2012) 2254–2263, [arXiv:1108.2041].

[87] G. Ossola, C. G. Papadopoulos, and R. Pittau, *On the Rational Terms of the one-loop amplitudes*, *JHEP* **0**5 (2008) 004, [arXiv:0802.1876].

[88] C. Degrande, *Automatic evaluation of UV and R2 terms for beyond the Standard Model Lagrangians: a proof-of-principle*, *Comput. Phys. Commun.* **1**97 (2015) 239–262, [arXiv:1406.3030].

[89] T. Hahn, *Generating Feynman diagrams and amplitudes with FeynArts 3*, *Comput. Phys. Commun.* **1**40 (2001) 418–431, [hep-ph/0012260].

[90] http://feynrules.irmp.ucl.ac.be/wiki/DMsimp.

[91] G. Ossola, C. G. Papadopoulos, and R. Pittau, *CutTools: A Program implementing the OPP reduction method to compute one-loop amplitudes*, *JHEP* **0**803 (2008) 042, [arXiv:0711.3596].

[92] V. Hirschi et al., *Automation of one-loop QCD corrections*, *JHEP* **0**5 (2011) 044, [arXiv:1103.0621].

[93] F. Cascioli, P. Maierhofer, and S. Pozzorini, *Scattering Amplitudes with Open Loops*, *Phys.Rev.Lett.* **1**08 (2012) 111601, [arXiv:1111.5206].

[94] R. Frederix, S. Frixione, F. Maltoni, and T. Stelzer, *Automation of next-to-leading order computations in QCD: the FKS subtraction*, *JHEP* **1**0 (2009) 003, [arXiv:0908.4272].

[95] S. Frixione and B. R. Webber, *Matching NLO QCD computations and parton shower simulations*, *JHEP* **0**206 (2002) 029, [hep-ph/0204244].

[96] T. Sjostrand, S. Mrenna, and P. Z. Skands, *PYTHIA 6.4 Physics and Manual*, *JHEP* **0**5 (2006) 026, [hep-ph/0603175].

[97] T. Sjostrand, S. Mrenna, and P. Z. Skands, *A Brief Introduction to PYTHIA 8.1*, *Comput. Phys. Commun.* **1**78 (2008) 852–867, [arXiv:0710.3820].

[98] G. Corcella, I. Knowles, G. Marchesini, S. Moretti, K. Odagiri, et al., *HERWIG 6: An Event generator for hadron emission reactions with interfering gluons (including supersymmetric processes)*, *JHEP* **0**101 (2001) 010, [hep-ph/0011363].

[99] M. Bahr, S. Gieseke, M. Gigg, D. Grellscheid, K. Hamilton, et al., *Herwig++ Physics and Manual*, *Eur.Phys.J.* **C**58 (2008) 639–707, [arXiv:0803.0883].

[100] M. Neubert, J. Wang, and C. Zhang, *Higher-Order QCD Predictions for Dark Matter Production in Mono-Z Searches at the LHC*, *JHEP* **0**2 (2016) 082, [arXiv:1509.05785].

[101] V. Hirschi and O. Mattelaer, *Automated event generation for loop-induced processes*, *JHEP* **1**0 (2015) 146, [arXiv:1507.00020].

[102] O. Mattelaer and E. Vryonidou, *Dark matter production through loop-induced processes at the LHC: the s-channel mediator case*, *Eur. Phys. J.* **C**75 (2015), no. 9 436, [arXiv:1508.00564].

[103] U. Haisch, F. Kahlhoefer, and J. Unwin, *The impact of heavy-quark loops on LHC dark matter searches*, *JHEP* **0**7 (2013) 125, [arXiv:1208.4605].

[104] M. R. Buckley, D. Feld, and D. Goncalves, *Scalar Simplified Models for Dark Matter*, *Phys.Rev.* **D**91 (2015), no. 1 015017, [arXiv:1410.6497].

[105] P. Harris, V. V. Khoze, M. Spannowsky, and C. Williams, *Constraining Dark Sectors at Colliders: Beyond the Effective Theory Approach*, *Phys.Rev.* **D**91 (2015), no. 5 055009, [arXiv:1411.0535].

[106] U. Haisch and E. Re, *Simplified dark matter top-quark interactions at the LHC*, *JHEP* **0**6 (2015) 078, [arXiv:1503.00691].

[107] J. Alwall, C. Duhr, B. Fuks, O. Mattelaer, D. G. Öztürk, and C.-H. Shen, *Computing decay rates for new physics theories with FeynRules and MadGraph5_aMC@NLO*, *Comput. Phys. Commun.* **1**97 (2015) 312–323, [arXiv:1402.1178].

[108] M. Botje et al., *The PDF4LHC Working Group Interim Recommendations*, arXiv:1101.0538.

[109] M. R. Whalley, D. Bourilkov, and R. C. Group, *The Les Houches accord PDFs (LHAPDF) and LHAGLUE*, in *HERA and the LHC: A Workshop on the implications of HERA for LHC physics. Proceedings, Part B*, 2005. hep-ph/0508110.

[110] R. Frederix, S. Frixione, V. Hirschi, F. Maltoni, R. Pittau, et al., *Four-lepton production at hadron colliders: aMC@NLO predictions with theoretical uncertainties*, *JHEP* **1**202 (2012) 099, [arXiv:1110.4738].

[111] S. Alekhin, S. Alioli, R. D. Ball, V. Bertone, J. Blumlein, et al., *The PDF4LHC Working Group Interim Report*, arXiv:1101.0536.

[112] M. Cacciari, G. P. Salam, and G. Soyez, *The Anti-k(t) jet clustering algorithm*, *JHEP* **0**804 (2008) 063, [arXiv:0802.1189].

[113] M. Cacciari, G. P. Salam, and G. Soyez, *FastJet User Manual*, *Eur. Phys. J.* **C**72 (2012) 1896, [arXiv:1111.6097].

[114] M. Rubin, G. P. Salam, and S. Sapeta, *Giant QCD K-factors beyond NLO*, *JHEP* **0**9 (2010) 084, [arXiv:1006.2144].

[115] K. Cheung, K. Mawatari, E. Senaha, P.-Y. Tseng, and T.-C. Yuan, *The Top Window for dark matter*, *JHEP* **1**0 (2010) 081, [arXiv:1009.0618].

[116] T. Lin, E. W. Kolb, and L.-T. Wang, *Probing dark matter couplings to top and bottom quarks at the LHC*, *Phys. Rev.* **D**88 (2013), no. 6 063510, [arXiv:1303.6638].

[117] G. Artoni, T. Lin, B. Penning, G. Sciolla, and A. Venturini, *Prospects for collider searches for dark matter with heavy quarks*, in *Community Summer Study 2013: Snowmass on the Mississippi (CSS2013) Minneapolis, MN, USA, July 29-August 6, 2013*, 2013. arXiv:1307.7834.

[118] **A**TLAS Collaboration, G. Aad et al., *Search for dark matter in events with heavy quarks and missing transverse momentum in pp collisions with the ATLAS detector*, *Eur. Phys. J.* **C**75 (2015), no. 2 92, [arXiv:1410.4031].

[119] **C**MS Collaboration, V. Khachatryan et al., *Search for the production of dark matter in association with top-quark pairs in the single-lepton final state in proton-proton collisions at sqrt(s) = 8 TeV*, *JHEP* **0**6 (2015) 121, [arXiv:1504.03198].

[120] N. Greiner, K. Kong, J.-C. Park, S. C. Park, and J.-C. Winter, *Model-Independent Production of a Top-Philic Resonance at the LHC*, *JHEP* **0**4 (2015) 029, [arXiv:1410.6099].

[121] P. Artoisenet, R. Frederix, O. Mattelaer, and R. Rietkerk, *Automatic spin-entangled decays of heavy resonances in Monte Carlo simulations*, *JHEP* **1**303 (2013) 015, [arXiv:1212.3460].

[122] S. Dawson and L. Reina, *QCD corrections to associated Higgs boson production*, *Phys.Rev.* **D**57 (1998) 5851–5859, [hep-ph/9712400].

[123] S. Dittmaier, M. Kramer, Y. Liao, M. Spira, and P. Zerwas, *Higgs radiation off quarks in supersymmetric theories at e^+e^- colliders*, *Phys.Lett.* **B**478 (2000) 247–254, [hep-ph/0002035].

[124] T. Han, J. Sayre, and S. Westhoff, *Top-Quark Initiated Processes at High-Energy Hadron Colliders*, *JHEP* **0**4 (2015) 145, [arXiv:1411.2588].

[125] F. Demartin, F. Maltoni, K. Mawatari, B. Page, and M. Zaro, *Higgs characterisation at NLO in QCD: CP properties of the top-quark Yukawa interaction*, *Eur.Phys.J.* **C**74 (2014), no. 9 3065, [arXiv:1407.5089].

[126] S. Ask, N. D. Christensen, C. Duhr, C. Grojean, S. Hoeche, et al., *From Lagrangians to Events: Computer Tutorial at the MC4BSM-2012 Workshop*, arXiv:1209.0297.

[127] P. Gondolo, J. Edsjo, P. Ullio, L. Bergstrom, M. Schelke, et al., *DarkSUSY: Computing supersymmetric dark matter properties numerically*, *JCAP* **0**407 (2004) 008, [astro-ph/0406204].

[128] G. Belanger, F. Boudjema, and A. Pukhov, *micrOMEGAs : a code for the calculation of Dark Matter properties in generic models of particle interaction*, arXiv:1402.0787.

[129] M. Backovic, K. Kong, and M. McCaskey, *MadDM v.1.0: Computation of Dark Matter Relic Abundance Using MadGraph5*, *Physics of the Dark Universe* **5**-6 (2014) 18–28, [arXiv:1308.4955].

[130] J. Alwall, M. Herquet, F. Maltoni, O. Mattelaer, and T. Stelzer, *MadGraph 5 : Going Beyond*, *JHEP* **1**106 (2011) 128, [arXiv:1106.0522].

[131] G. Mohlabeng, K. Kong, J. Li, A. Para, and J. Yoo, *Dark Matter Directionality Revisited with a High Pressure Xenon Gas Detector*, *JHEP* **0**7 (2015) 092, [arXiv:1503.03937].

[132] C. J. Copi, J. Heo, and L. M. Krauss, *Directional sensitivity, WIMP detection, and the galactic halo*, *Phys.Lett.* **B**461 (1999) 43–48, [hep-ph/9904499].

[133] P. Gondolo, *Recoil momentum spectrum in directional dark matter detectors*, *Phys.Rev.* **D**66 (2002) 103513, [hep-ph/0209110].

[134] P. Grothaus, M. Fairbairn, and J. Monroe, *Directional Dark Matter Detection Beyond the Neutrino Bound*, *Phys.Rev.* **D**90 (2014) 055018, [arXiv:1406.5047].

[135] P. Z. Skands, B. Allanach, H. Baer, C. Balazs, G. Belanger, et al., *SUSY Les Houches accord: Interfacing SUSY spectrum calculators, decay packages, and event generators*, *JHEP* **0**407 (2004) 036, [hep-ph/0311123].

[136] B. Allanach, C. Balazs, G. Belanger, M. Bernhardt, F. Boudjema, et al., *SUSY Les Houches Accord 2*, *Comput.Phys.Commun.* **1**80 (2009) 8–25, [arXiv:0801.0045].

[137] **L**UX Collaboration Collaboration, C. Faham, *First Dark Matter Search Results from the Large Underground Xenon (LUX) Experiment*, arXiv:1405.5906.

[138] **X**ENON Collaboration, A. Brown, *XENON dark matter searches: Results and the future*, *AIP Conf.Proc.* **1**604 (2014) 313–318.

[139] **C**DMS Collaboration, T. Saab, *Dark matter searches with the CDMS II experiment*, *AIP Conf.Proc.* **1**604 (2014) 436–441.

[140] C. E. Aalseth et al., *Search for an Annual Modulation in a P-type Point Contact Germanium Dark Matter Detector*, *Phys. Rev. Lett.* **1**07 (2011) 141301, [arXiv:1106.0650].

[141] **D**AMA Collaboration, LIBRA Collaboration Collaboration, R. Bernabei et al., *New results from DAMA/LIBRA*, *Eur.Phys.J.* **C**67 (2010) 39–49, [arXiv:1002.1028].

[142] **L**UX Collaboration, D. S. Akerib et al., *First results from the LUX dark matter experiment at the Sanford Underground Research Facility*, *Phys. Rev. Lett.* **1**12 (2014) 091303, [arXiv:1310.8214].

[143] B. A. Dobrescu, D. Hooper, K. Kong, and R. Mahbubani, *Spinless photon dark matter from two universal extra dimensions*, *JCAP* **0**710 (2007) 012, [arXiv:0706.3409].

[144] M. Freytsis and Z. Ligeti, *On dark matter models with uniquely spin-dependent detection possibilities*, *Phys.Rev.* **D**83 (2011) 115009, [arXiv:1012.5317].

[145] G. Belanger, F. Boudjema, A. Pukhov, and A. Semenov, *Dark matter direct detection rate in a generic model with micrOMEGAs 2.2*, *Comput. Phys. Commun.* **1**80 (2009) 747–767, [arXiv:0803.2360].

[146] D. N. Spergel, *The Motion of the Earth and the Detection of Wimps*, *Phys.Rev.* **D**37 (1988) 1353.

[147] **P**article Data Group Collaboration, J. Beringer et al., *Review of Particle Physics (RPP)*, *Phys.Rev.* **D**86 (2012) 010001.

[148] **H**ERMES Collaboration, A. Airapetian et al., *Precise determination of the spin structure function g(1) of the proton, deuteron and neutron*, *Phys.Rev.* **D**75 (2007) 012007, [hep-ex/0609039].

[149] **C**ompass Collaboration, E. Ageev et al., *Spin asymmetry A1(d) and the spin-dependent structure function g1(d) of the deuteron at low values of x and Q**2*, *Phys.Lett.* **B**647 (2007) 330–340, [hep-ex/0701014].

[150] S. Aoki, M. Doui, T. Hatsuda, and Y. Kuramashi, *Tensor charge of the nucleon in lattice QCD*, *Phys.Rev.* **D**56 (1997) 433–436, [hep-lat/9608115].

[151] M. Drees and M. Nojiri, *Neutralino - nucleon scattering revisited*, *Phys.Rev.* **D**48 (1993) 3483–3501, [hep-ph/9307208].

[152] J. Hisano, R. Nagai, and N. Nagata, *Effective Theories for Dark Matter Nucleon Scattering*, *JHEP* **1**505 (2015) 037, [arXiv:1502.02244].

[153] D. Santos, J. Billard, G. Bosson, J. Bouly, O. Bourrion, et al., *MIMAC: A micro-tpc matrix for dark matter directional detection*, *J.Phys.Conf.Ser.* **4**60 (2013) 012007, [arXiv:1304.2255].

[154] E. Daw, J. Fox, J.-L. Gauvreau, M. Gold, L. Harmon, et al., *Long-term study of backgrounds in the DRIFT-II directional dark matter experiment*, *JINST* **9** (2014) P07021, [arXiv:1307.5525].

[155] **D**M-TPC Collaboration, G. Sciolla et al., *Toward directional detection of Dark Matter with the DM-TPC detector*, arXiv:0806.2673.

[156] D. Nygren, *Columnar recombination: a tool for nuclear recoil directional sensitivity in a xenon-based direct detection WIMP search*, *J.Phys.Conf.Ser.* **4**60 (2013) 012006.

[157] J. Billard, L. Strigari, and E. Figueroa-Feliciano, *Implication of neutrino backgrounds on the reach of next generation dark matter direct detection experiments*, *Phys.Rev.* **D**89 (2014), no. 2 023524, [arXiv:1307.5458].

[158] J. H. Davis, *Dark Matter vs. Neutrinos: The effect of astrophysical uncertainties and timing information on the neutrino floor*, *JCAP* **1**503 (2015), no. 03 012, [arXiv:1412.1475].

[159] C. J. Copi and L. M. Krauss, *Angular signatures for galactic halo WIMP scattering in direct detectors: Prospects and challenges*, *Phys.Rev.* **D**63 (2001) 043507, [astro-ph/0009467].

[160] J. Lewin and P. Smith, *Review of mathematics, numerical factors, and corrections for dark matter experiments based on elastic nuclear recoil*, *Astropart.Phys.* **6** (1996) 87–112.

[161] S. Arrenberg, L. Baudis, K. Kong, K. T. Matchev, and J. Yoo, *Kaluza-Klein Dark Matter: Direct Detection vis-a-vis LHC*, *Phys.Rev.* **D**78 (2008) 056002, [arXiv:0805.4210].

[162] S. Arrenberg, L. Baudis, K. Kong, K. T. Matchev, and J. Yoo, *Kaluza-Klein Dark Matter: Direct Detection vis-a-vis LHC (2013 update)*, arXiv:1307.6581.

[163] G. Servant and T. M. Tait, *Elastic scattering and direct detection of Kaluza-Klein dark matter*, *New J.Phys.* **4** (2002) 99, [hep-ph/0209262].

[164] H.-C. Cheng, J. L. Feng, and K. T. Matchev, *Kaluza-Klein dark matter*, *Phys.Rev.Lett.* **8**9 (2002) 211301, [hep-ph/0207125].

[165] B. Allanach, M. Battaglia, G. Blair, M. S. Carena, A. De Roeck, et al., *The Snowmass points and slopes: Benchmarks for SUSY searches*, *Eur.Phys.J.* **C**25 (2002) 113–123, [hep-ph/0202233].

[166] **C**MS Collaboration, V. Khachatryan et al., *Search for dark matter in proton-proton collisions at 8 TeV with missing transverse momentum and vector boson tagged jets*, *JHEP* **1**2 (2016) 083, [arXiv:1607.05764].

[167] https://launchpad.net/maddm.

[168] **D**ELPHES 3 Collaboration, J. de Favereau, C. Delaere, P. Demin, A. Giammanco, V. Lemaître, A. Mertens, and M. Selvaggi, *DELPHES 3, A modular framework for fast simulation of a generic collider experiment*, *JHEP* **0**2 (2014) 057, [arXiv:1307.6346].

[169] E. Conte, B. Fuks, and G. Serret, *MadAnalysis 5, A User-Friendly Framework for Collider Phenomenology*, *Comput. Phys. Commun.* **1**84 (2013) 222–256, [arXiv:1206.1599].

[170] E. Conte, B. Dumont, B. Fuks, and C. Wymant, *Designing and recasting LHC analyses with MadAnalysis 5*, *Eur. Phys. J.* **C**74 (2014), no. 10 3103, [arXiv:1405.3982].

[171] B. Dumont, B. Fuks, S. Kraml, S. Bein, G. Chalons, E. Conte, S. Kulkarni, D. Sengupta, and C. Wymant, *Toward a public analysis database for LHC new physics searches using MADANALYSIS 5*, *Eur. Phys. J.* **C**75 (2015), no. 2 56, [arXiv:1407.3278].

[172] F. Feroz and M. Hobson, *Multimodal nested sampling: an efficient and robust alternative to MCMC methods for astronomical data analysis*, *Mon.Not.Roy.Astron.Soc.* **3**84 (2008) 449, [arXiv:0704.3704].

[173] F. Feroz, M. Hobson, and M. Bridges, *MultiNest: an efficient and robust Bayesian inference tool for cosmology and particle physics*, *Mon.Not.Roy.Astron.Soc.* **3**98 (2009) 1601–1614, [arXiv:0809.3437].

[174] G. D'Ambrosio, G. F. Giudice, G. Isidori, and A. Strumia, *Minimal flavor violation: An Effective field theory approach*, *Nucl. Phys.* **B**645 (2002) 155–187, [hep-ph/0207036].

[175] N. Craig, J. Galloway, and S. Thomas, *Searching for Signs of the Second Higgs Doublet*, arXiv:1305.2424.

[176] M. Carena, I. Low, N. R. Shah, and C. E. M. Wagner, *Impersonating the Standard Model Higgs Boson: Alignment without Decoupling*, *JHEP* **0**4 (2014) 015, [arXiv:1310.2248].

[177] Y. G. Kim, K. Y. Lee, and S. Shin, *Singlet fermionic dark matter*, *JHEP* **0**5 (2008) 100, [arXiv:0803.2932].

[178] S. Baek, P. Ko, and W.-I. Park, *Search for the Higgs portal to a singlet fermionic dark matter at the LHC*, *JHEP* **0**2 (2012) 047, [arXiv:1112.1847].

[179] L. Lopez-Honorez, T. Schwetz, and J. Zupan, *Higgs portal, fermionic dark matter, and a Standard Model like Higgs at 125 GeV*, *Phys. Lett.* **B**716 (2012) 179–185, [arXiv:1203.2064].

[180] S. Baek, P. Ko, and W.-I. Park, *Invisible Higgs Decay Width vs. Dark Matter Direct Detection Cross Section in Higgs Portal Dark Matter Models*, *Phys. Rev.* **D**90 (2014), no. 5 055014, [arXiv:1405.3530].

[181] S. Baek, P. Ko, M. Park, W.-I. Park, and C. Yu, *Beyond the Dark matter effective field theory and a simplified model approach at colliders*, *Phys. Lett.* **B**756 (2016) 289–294, [arXiv:1506.06556].

[182] P. Ko and H. Yokoya, *Search for Higgs portal DM at the ILC*, *JHEP* **0**8 (2016) 109, [arXiv:1603.04737].

[183] **F**ermi-LAT Collaboration, M. Ackermann et al., *Updated search for spectral lines from Galactic dark matter interactions with pass 8 data from the Fermi Large Area Telescope*, *Phys. Rev.* **D**91 (2015), no. 12 122002, [arXiv:1506.00013].

[184] **F**ermi-LAT Collaboration, M. Ackermann et al., *Searching for Dark Matter Annihilation from Milky Way Dwarf Spheroidal Galaxies with Six Years of Fermi Large Area Telescope Data*, *Phys. Rev. Lett.* **1**15 (2015), no. 23 231301, [arXiv:1503.02641].

[185] J. M. Alarcon, J. Martin Camalich, and J. A. Oller, *The chiral representation of the πN scattering amplitude and the pion-nucleon sigma term*, *Phys. Rev.* **D**85 (2012) 051503, [arXiv:1110.3797].

[186] J. M. Alarcon, L. S. Geng, J. Martin Camalich, and J. A. Oller, *The strangeness content of the nucleon from effective field theory and phenomenology*, *Phys. Lett.* **B**730 (2014) 342–346, [arXiv:1209.2870].

[187] F. D'Eramo and M. Procura, *Connecting Dark Matter UV Complete Models to Direct Detection Rates via Effective Field Theory*, *JHEP* **0**4 (2015) 054, [arXiv:1411.3342].

[188] L. Vecchi, *WIMPs and Un-Naturalness*, arXiv:1312.5695.

[189] **L**HC Higgs Cross Section Working Group Collaboration, J. R. Andersen et al., *Handbook of LHC Higgs Cross Sections: 3. Higgs Properties*, arXiv:1307.1347.

[190] R. D. Ball et al., *Parton distributions with LHC data*, *Nucl. Phys.* **B**867 (2013) 244–289, [arXiv:1207.1303].

[191] A. Buckley, J. Ferrando, S. Lloyd, K. Nordström, B. Page, M. Rüfenacht, M. Schönherr, and G. Watt, *LHAPDF6: parton density access in the LHC precision era*, *Eur. Phys. J.* **C**75 (2015) 132, [arXiv:1412.7420].

[192] **C**MS Collaboration, V. Khachatryan et al., *Search for dark matter, extra dimensions, and unparticles in monojet events in proton-proton collisions at $\sqrt{s} = 8$ TeV*, *Eur. Phys. J.* **C**75 (2015), no. 5 235, [arXiv:1408.3583].

[193] **C**MS Collaboration, V. Khachatryan et al., *Search for dark matter and unparticles produced in association with a Z boson in proton-proton collisions at $\sqrt{s}$=8 TeV*, *Phys. Rev.* **D**93 (2016), no. 5 052011, [arXiv:1511.09375].

[194] **A**TLAS Collaboration, G. Aad et al., *Search for dark matter produced in association with a Higgs boson decaying to two bottom quarks in pp collisions at $\sqrt{s} = 8$ TeV with the ATLAS detector*, *Phys. Rev.* **D**93 (2016), no. 7 072007, [arXiv:1510.06218].

[195] **C**MS Collaboration, *Search for Resonances Decaying to Dijet Final States at $\sqrt{s} = 8$ TeV with Scouting Data*, CMS-PAS-EXO-14-005.

[196] **C**MS Collaboration, V. Khachatryan et al., *Search for diphoton resonances in the mass range from 150 to 850 GeV in pp collisions at $\sqrt{s} = 8$ TeV*, *Phys. Lett.* **B**750 (2015) 494–519, [arXiv:1506.02301].

[197] **A**TLAS Collaboration, G. Aad et al., *A search for $t\bar{t}$ resonances using lepton-plus-jets events in proton-proton collisions at $\sqrt{s} = 8$ TeV with the ATLAS detector*, *JHEP* **0**8 (2015) 148, [arXiv:1505.07018].

[198] **C**MS Collaboration, V. Khachatryan et al., *Search for Standard Model Production of Four Top Quarks in the Lepton + Jets Channel in pp Collisions at $\sqrt{s}$ = 8 TeV*, *JHEP* **1**1 (2014) 154, [arXiv:1409.7339].

[199] **A**TLAS Collaboration, G. Aad et al., *Search for new phenomena in final states with an energetic jet and large missing transverse momentum in pp collisions at $\sqrt{s}$ =8 TeV with the ATLAS detector*, *Eur. Phys. J.* **C**75 (2015), no. 7 299, [arXiv:1502.01518]. [Erratum: Eur. Phys. J.C75,no.9,408(2015)].

[200] **C**MS Collaboration, *Search for dark matter with jets and missing transverse energy at 13 TeV*, CMS-PAS-EXO-15-003.

[201] **A**TLAS Collaboration, G. Aad et al., *Search for dark matter in events with a hadronically decaying W or Z boson and missing transverse momentum in pp collisions at $\sqrt{s} = 8$ TeV with the ATLAS detector*, *Phys. Rev. Lett.* **1**12 (2014), no. 4 041802, [arXiv:1309.4017].

[202] **A**TLAS Collaboration, G. Aad et al., *Search for dark matter in events with a Z boson and missing transverse momentum in pp collisions at $\sqrt{s}$=8 TeV with the ATLAS detector*, *Phys. Rev.* **D**90 (2014), no. 1 012004, [arXiv:1404.0051].

[203] **C**MS Collaboration, *Search for New Physics in the V-jet + MET final state*, CMS-PAS-EXO-12-055.

[204] **A**TLAS Collaboration, M. Aaboud et al., *Search for dark matter produced in association with a hadronically decaying vector boson in pp collisions at $\sqrt{s} = 13$ TeV with the ATLAS detector*, *Phys. Lett.* **B**763 (2016) 251–268, [arXiv:1608.02372].

[205] **A**TLAS Collaboration, G. Aad et al., *Search for Dark Matter in Events with Missing Transverse Momentum and a Higgs Boson Decaying to Two Photons in pp Collisions at $\sqrt{s} = 8$ TeV with the ATLAS Detector*, *Phys. Rev. Lett.* **1**15 (2015), no. 13 131801, [arXiv:1506.01081].

[206] **A**TLAS Collaboration, *Search for new phenomena in events with missing transverse momentum and a Higgs boson decaying to two photons in p p collisions at $\sqrt{s} = 13$ TeV with the ATLAS detector*, ATLAS-CONF-2016-011.

[207] **A**TLAS Collaboration, *Search for Dark Matter in association with a Higgs boson decaying to b-quarks in pp collisions at $\sqrt{s} = 13$ TeV with the ATLAS detector*, ATLAS-CONF-2016-019.

[208] D. Goncalves, F. Krauss, S. Kuttimalai, and P. Maierhöfer, *Boosting invisible searches via ZH : From the Higgs boson to dark matter simplified models*, *Phys. Rev.* **D**94 (2016), no. 5 053014, [arXiv:1605.08039].

[209] **C**MS Collaboration, V. Khachatryan et al., *Search for narrow resonances in dijet final states at $\sqrt{s} = 8$ TeV with the novel CMS technique of data scouting*, *Phys. Rev. Lett.* **1**17 (2016), no. 3 031802, [arXiv:1604.08907].

[210] **C**MS Collaboration, V. Khachatryan et al., *Search for resonant $t\bar{t}$ production in proton-proton collisions at $\sqrt{s} = 8$ TeV*, *Phys. Rev.* **D**93 (2016), no. 1 012001, [arXiv:1506.03062].

[211] G. Bevilacqua and M. Worek, *Constraining BSM Physics at the LHC: Four top final states with NLO accuracy in perturbative QCD*, *JHEP* **0**7 (2012) 111, [arXiv:1206.3064].

[212] **C**MS Collaboration, S. Chatrchyan et al., *Search for new physics in events with same-sign dileptons and jets in pp collisions at $\sqrt{s}$ = 8 TeV*, *JHEP* **0**1 (2014) 163, [arXiv:1311.6736]. [Erratum: JHEP01,014(2015)].

[213] L. Beck, F. Blekman, D. Dobur, B. Fuks, J. Keaveney, and K. Mawatari, *Probing top-philic sgluons with LHC Run I data*, *Phys. Lett.* **B**746 (2015) 48–52, [arXiv:1501.07580].

[214] K. Hagiwara, J. Kanzaki, Q. Li, and K. Mawatari, *HELAS and MadGraph/MadEvent with spin-2 particles*, *Eur.Phys.J.* **C**56 (2008) 435–447, [arXiv:0805.2554].

[215] A. Martini, K. Mawatari, and D. Sengupta, *Diphoton excess in phenomenological spin-2 resonance scenarios*, *Phys. Rev.* **D**93 (2016), no. 7 075011, [arXiv:1601.05729].

[216] S. Kraml, U. Laa, K. Mawatari, and K. Yamashita, *Simplified dark matter models with a spin-2 mediator at the LHC*, arXiv:1701.07008.

[217] B. R. Holstein, *Graviton Physics*, *Am. J. Phys.* **7**4 (2006) 1002–1011, [gr-qc/0607045].

[218] J. Pumplin, D. R. Stump, J. Huston, H. L. Lai, P. M. Nadolsky, and W. K. Tung, *New generation of parton distributions with uncertainties from global QCD analysis*, *JHEP* **0**7 (2002) 012, [hep-ph/0201195].

[219] R. Field, *Min-Bias and the Underlying Event at the LHC*, *Acta Phys. Polon.* **B**42 (2011) 2631–2656, [arXiv:1110.5530].

[220] M. L. Mangano, M. Moretti, F. Piccinini, and M. Treccani, *Matching matrix elements and shower evolution for top-quark production in hadronic collisions*, *JHEP* **0**1 (2007) 013, [hep-ph/0611129].

[221] J. Alwall, S. de Visscher, and F. Maltoni, *QCD radiation in the production of heavy colored particles at the LHC*, *JHEP* **0**2 (2009) 017, [arXiv:0810.5350].

[222] J. Guo, E. Conte, and B. Fuks, *MadAnalysis5 implementation of the CMS monojet search (EXO-12-048)*, 10.7484/INSPIREHEP.DATA.JAN2.UNDA.

[223] B. Fuks and A. Martini, *MadAnalysis5 implementation of the CMS search for dark matter production with top quark pairs in the single lepton channel (CMS-B2G-14-004)*, 10.7484/INSPIREHEP.DATA.MIHA.JR4G.

[224] Y. Bai, H.-C. Cheng, J. Gallicchio, and J. Gu, *Stop the Top Background of the Stop Search*, *JHEP* **0**7 (2012) 110, [arXiv:1203.4813].

[225] M. Beltran, D. Hooper, E. W. Kolb, Z. A. C. Krusberg, and T. M. P. Tait, *Maverick dark matter at colliders*, *JHEP* **0**9 (2010) 037, [arXiv:1002.4137].

[226] J. Goodman, M. Ibe, A. Rajaraman, W. Shepherd, T. M. P. Tait, and H.-B. Yu, *Constraints on Dark Matter from Colliders*, *Phys. Rev.* **D**82 (2010) 116010, [arXiv:1008.1783].